Fluid Flow Behavior of Semi-Solid Aluminum at High Shear Rates

by

James Andrew Yurko

B.S.E., Materials Science and Engineering, University of Michigan (1997)

Submitted to the Department of Materials Science and Engineering
in partial fulfillment of the requirements for the degree of

Doctor of Philosophy

at the

MASSACHUSETTS INSTITUTE OF TECHNOLOGY

June 2001

Signature of Author .....
Department of Materials Science and Engineering
4 May 2001

Certified by .....
Merton C. Flemings
Toyota Professor of Materials Processing
Thesis Advisor

Accepted by .....
Harry L. Tuller
Professor of Ceramics and Electronic Materials
Chair, Department Committee on Graduate Students

Fluid Flow Behavior of Semi-Solid Aluminum at High Shear Rates

by

James Andrew Yurko

Submitted to the Department of Materials Science and Engineering
on 4 May 2001, in partial fulfillment of the
requirements for the degree of
Doctor of Philosophy

Abstract

The rheological behavior and microstructure of semi-solid aluminum alloys were studied using a novel apparatus, the Drop Forge Viscometer (DFV). The viscometer determines force from the curvature of displacement data allowing calculations of viscosities at shear rates in excess of $1000\ s^{-1}$. Alternatively, the DFV can be operated like a conventional parallel-plate compression viscometer, attaining shear rates as low as $10^{-5}\ s^{-1}$. Durations of an experiment range between approximately 5 ms and 24 hours.

Most rapid compression tests resulted in periods of first rapidly increasing shear rate followed by rapidly decreasing shear rate. Viscosity during the increasing shear rate period decreased by 1-2 orders of magnitude. The viscosity during the decreasing shear rate was an order of magnitude smaller (relative to another experiment) when it achieved a 75% greater maximum shear rate.

The DFV was used to calculate viscosity as a function of shear rate for Al-Si and Al-Cu alloys that were rheocast with the commercial SIMA and MHD processes, as well as the recently developed MIT method. Experiments were conducted between fractions solid of 0.44 and 0.67. Viscosity of A357 produced by the three processing routes all had similar viscosities, ranging from 300 Pa·s at $120\ s^{-1}$ to 2.2 Pa·s at $1500\ s^{-1}$. The final height of compressed Al-Cu was always greater than Al-Si for a given set of experimental conditions.

Segregation was not observed in rapid compression experiments shorter than 10 ms, either visually or with EDS characterization. At low compression velocities, segregation was observed and increased with the amount of strain.

Thesis Advisor: Merton C. Flemings
Title: Toyota Professor of Materials Processing

Contents

List of Tables

List of Figures

Acknowledgments

I would not have been able to complete my graduate work without the help and support of numerous people, and I want to express my gratitude to each of them. Besides the people mentioned in these paragraphs, there were many, many more that either helped me on the long road or gave me inspiration to finish my thesis.

My parents, back home in Yale, Michigan, have supported me throughout my academic career, giving me their unconditional love and helping me grow up into a man. This work is dedicated to them, and I thank you for all the sacrifices you have made.

My advisor, Professor Merton Flemings, allowed me the privilege of joining the Solidification Research Group and gave me a large degree of freedom in managing and conducting my thesis work. This confidence that you showed in me was extremely helpful in my development as a researcher.

I gratefully acknowledge the help of my thesis committee, Professors Sam Allen and Klavs Jensen, for their guidance and help during the final stages of this work. I also would like to thank Prof. Chris Scott for helping me during the initial stages of the work.

There are several people at MIT that were a tremendous help the last four years. Dr. Doug Matson, my mentor and friend, not only helped me in the laboratory, but he also welcomed me into his family and guided me through the more tumultuous times. Dr. Anacleto de Figueredo was instrumental in the design and construction of the Drop Forge Viscometer and passed on to me a tiny bit of his infinite laboratory knowledge. Dr. Gerardo Trapaga showed me the power of computational physical modeling, and I will never forget our conversations standing in the courtyard outside of Building 4.

Other members of the Solidification Research Group, including Prof. Theo Kattamis, Dr. Akira Kato, Daniel Sandoval, Tomomitsu Inada, Cuong Bui, Jessada Wannasin, Lori Kensel, Stacey Rochford, and Nadia Brunner helped make the day-to-day experience of working in the group enjoyable. In particular, I want to thank Andy Martinez, who has worked alongside me the last two years, helping make the semi-solid research project the success it is today.

I made numerous friends while at MIT, people that are so incredibly talented I feel lucky to say I know them: Jared Martin, Philip Singer, Jason Richards, Zubin Irani, Chris Vineis, Ben Hellweg, Mike Read, Steve Murray, Tom Langdo, Toby Freyman, Krystyn Van Vliet, Mindy

Tupper, Bob Hyers, Jeff Nystrom, and Neil Jenkins. We have lots of stories and memories that I hope we can share again with each other in the future.

Finally, I would like to thank the person who has made the last two years at MIT the greatest time in my life, Joanie Kertz. We met each other at a time when the insanity of MIT and graduate school was at its zenith, and her love and friendship were essential in getting through. I know we have many unwritten chapters left to complete together.

Last but not least, I would like to thank the United States of America, for funding my research through a Department of Energy research grant and also a National Science Foundation Graduate Research Fellowship. Her financial support allowed me to pursue my dreams of receiving an advanced degree in Materials Science and Engineering.

James A. Yurko

Cambridge, MA

May, 2001

Chapter 1

Introduction

There have been numerous studies on the rheological behavior of semi-solid metal since it was discovered that alloys sheared during solidification possessed a non-dendritic microstructure, similar in manner to a concentrated suspension. This non-dendritic, equiaxed microstructure opened up the possibility of metal forming in the two-phase solid/liquid state.

Early rheological work on semi-solid alloys focused on characterizing the material at steady-state flow conditions, relating process variables such as temperature, shear rate, and grain morphology with viscosity. Recent studies, however, have focused on understanding the flow behavior during transient, high shear rate flow conditions, more representative of industrial forming processes.

Rheological study of semi-solid metals is challenging, particularly with conventional viscometers under transient conditions at temperatures in excess of 600 °C and volume fractions solid above 0.40. In addition, most rotational instruments have relied upon producing the semi-solid alloy *in-situ,* and they are unable to examine commercially produced material. Modeling of the flow behavior is also challenging. Chemical engineers have struggled to model suspensions for decades, using numerous models to describe their behavior. Metallurgists are now encountering this problem with the modeling of semi-solid alloys.

A novel apparatus, the Drop Forge Viscometer (DFV), has been built and constructed at MIT based on the parallel-plate compression rheometer. The instrument has the ability to characterize the flow behavior of commercially produced, semi-solid aluminum alloys under rapid transient behavior, at time resolution on the order of milliseconds. The major objectives

of this work are the following:.

- Develop the Drop Forge Viscometer into a robust technique for examining the flow behavior of semi-solid aluminum alloys at transient, high shear rates, as well as to develop the DFV into a tool with commercial process control capability.
- Determine viscosity as a function of shear rate and fraction solid for rheocast A357 produced by three different techniques, known as the SIMA, MHD, and MIT processes, as well as other Al-Si and Al-Cu alloys produced at MIT.
- Compare results from these alloys using the DFV and with previous studies using other compression and rotational rheometers.
- Achieve a better fundamental understanding of the effect of microstructure on the flow properties of semi-solid aluminum alloys, and determine under what process conditions separation of liquid and solid phases occurs.

Chapter 2

Literature Review

2.1 Rheology of Suspensions

A suspension is defined as a mixture of a solid in a liquid, and semi-solid metal alloys in the two phase solid/liquid state fall under this general definition. Suspensions can be categorized in numerous ways, two of which are by the size of the solid particles and the volume fraction of the solid phase. Depending on the size of the particles, the interacting forces are either hydrodynamic or non-hydrodynamic. When the solid particles are small (< 1 μm), the forces that dominate are non-hydrodynamic and consist of Van der Waals, electrical, and thermal (Brownian) forces. When the volume fraction is less than 0.02, particle interaction is minimal, and the suspension is considered dilute [1]. Metal slurries qualify as non-dilute suspensions with interacting particles.

The primary goal of researchers has been to understand how suspensions behave under various flow conditions. The inherent property that dictates how a fluid responds to rate of deformation is *viscosity*, or the momentum transfer rate of a fluid when sheared. Although suspensions are two phase materials, it is common to treat them as a homogeneous fluid and therefore assign them an apparent viscosity [2]. Experimental studies have tried to characterize viscosity of suspensions, but because the flow is complex and the viscosity is a function of many variables, there is wide variation in reported flow behavior. The range of reported experimental results has led to numerous models that attempt to predict the fluid behavior. The following section will discuss the background of rheological suspension work.

2.1.1 Early Studies of Suspensions

The most widely cited, early work on the flow behavior of suspensions are Einstein's classic papers of 1906 and 1911 [3]. Assuming a dilute volume fraction and negligible inertia, Einstein derived an effective viscosity (μ^*) that is a function of the liquid viscosity (μ_o) and the volume fraction (ϕ).

$$\mu^* = \mu_o(1 + \frac{5}{2}\phi) \tag{2.1}$$

Researchers over the years tried to adapt the effective viscosity equation so it could be used at higher volume fraction, thus ignoring particle interactions and other variables. The neglect of particle interactions and shear rate on viscosity became apparent from the experimental results of early studies. As seen in Figure 2-1, Rutgers summarized the experimental results of effective viscosity as a function of volume fraction, and he found deviation of over two orders of magnitude in relative viscosity at high volume fraction [4]. Thomas tabulated existing data from various researchers (Figure 2-2) and extrapolated the results to get an average relative viscosity curve as a function of volume fraction [5]. Upon examination of Figures 2-1 and 2-2, it can be seen that there is significant disagreement in the results.

The empirical equation of Krieger and Dougherty stands out from the early suspension work as providing the most reliable results for concentrated hard-sphere suspensions because it takes into account the maximum packing factor [6]. The equation is given as

$$\frac{\mu^*}{\mu_o} = \left(1 - \frac{\phi}{\phi_m}\right)^{-[\mu]\phi_m} \tag{2.2}$$

where ϕ_m is the maximum packing factor and $[\mu]$ is the intrinsic viscosity of the suspension.

Frankel and Acrivos, using an energy dissipation theory based on particle interactions, developed the model

$$\frac{\mu^*}{\mu_o} = \frac{9}{8}\left(\frac{(\phi/\phi_m)^{1/3}}{1 - (\phi/\phi_m)^{1/3}}\right) \tag{2.3}$$

to argue that flow between particles is the dominating force in determining viscosity [7]. The model was an improvement over empirical models, but it still did not take into account collisions and aggregation of solid particles or inertial effects.

2.1.2 Recent Studies of Suspensions

Researchers have tried to develop exact relationships for describing suspensions at high concentrations of solid particles. Known as constitutive relationships, they are used to relate the stress tensor in a fluid with its rate of deformation tensor. Of the numerous models for suspensions, the original was developed by Batchelor [8]. Using statistical mechanic approaches of calculating an average stress over a volume, the forces acting over a number of particles in a volume are added.

$$\langle \sigma_{ij} \rangle = \frac{1}{V} \int \sigma_{ij} dV \tag{2.4}$$

Recent work has focused on refining constitutive relationship theory to account for particle interaction forces in the various types of suspensions [9]-[11]. Exact solutions to these types of constitutive relationships are computationally intensive, but they are becoming more manageable with modern computing speed.

2.1.3 General Constitutive Relationships

General constitutive equations are useful in describing the nature of fluid behavior depending on how the stress in the fluid changes with the rate of deformation. There are four basic relationships for time-independent, simple shear fluid flow, as depicted in Figure 2-3 [12].

Newtonian Fluid

The straight line in Figure 2-3 represents Newtonian flow, which can be expressed with Newton's law of viscosity, where τ is the shear stress and $\dot{\gamma}$ is the shear rate.

$$\tau = -\mu \dot{\gamma} \tag{2.5}$$

The viscosity, or the slope of this curve, is independent of shear rate. Many fluids can be characterized as Newtonian, including water and liquid metals.

Non-Newtonian, Power Law Fluid

Pseudoplastic and dilatant fluids, on the other hand, have a viscosity that is dependent on shear rate. They are also referred to as shear thinning and shear thickening fluids, respectively. The simplest model to describe the flow behavior of these fluids is the power law or Ostwald de Waele equation

$$\tau = k\dot{\gamma}^n \tag{2.6}$$

where n is the power law exponent. When n is equal to one, the equation simplifies to Equation 2.5. If $n > 1$, the fluid is dilatant, and viscosity increases with increasing shear rate. When $n < 1$, the fluid is shear thinning and viscosity decreases with increasing shear rate. Many fluids, including colloidal suspensions and polymer solutions, are shear thinning, while others, including concentrated suspensions, are shear thickening.

Bingham Plastic

The final fluid represented in Figure 2-3 is a Bingham plastic. Bingham fluids have a yield stress; therefore, the fluid does not begin to shear until the critical stress has been applied. After yielding, depending on whether the fluid is Newtonian or non-Newtonian, the fluid is referred to as either a Bingham or Herschel-Bulkley fluid, respectively. The simplest model of a Bingham plastic is represented in Equation 2.7, where τ_o is the yield stress.

$$\tau = \mu\dot{\gamma} + \tau_o \quad for\ \tau \geq \tau_o \tag{2.7}$$

The shear rate is zero unless the shear stress is greater than the yield stress. Paint, mayonnaise, and ketchup are all examples of Bingham plastics.

The yield stress in a fluid has been fundamentally defined in different ways, and recently it has been proposed that there are actually three different types of yield stresses [13]. The first, the *elastic-limit yield stress,* τ_y, is the stress above which plastic deformation begins. The second type is designated the *static yield stress,* τ_s, and this is defined as the minimum stress necessary for unbounded strain or deformation, or the border between plastic and viscous flow. A third term, the *dynamic yield stress,* τ_d, is the stress obtained when a shear stress-shear rate plot is extrapolated to zero shear rate. This is the stress that is used most frequently in flow

modeling.

Researchers have described the non-Newtonian fluid behavior of concentrated suspensions as shear thinning [14]-[16], shear thickening [15]-[20], and exhibiting a yield stress [13],[21]. Each of the above fluid types can be expressed in a more general manner as described in the following section.

2.1.4 General Viscous Fluid

The more general form of Newton's viscosity law is written in tensor notation as

$$\boldsymbol{\tau}_{ij} = \mu \mathbf{2D}_{ij} \tag{2.8}$$

where **2D** is the *rate of deformation* tensor. Theory on the general viscous fluid is summarized in Chapter 4 of Macosko [1]. In Cartesian coordinates, the rate of deformation tensor in complete form is expressed as

$$\mathbf{2D} = \begin{pmatrix} 2 \cdot \frac{\partial v_x}{\partial x} & \frac{\partial v_x}{\partial y} + \frac{\partial v_y}{\partial x} & \frac{\partial v_x}{\partial z} + \frac{\partial v_z}{\partial x} \\ \frac{\partial v_y}{\partial x} + \frac{\partial v_x}{\partial y} & 2 \cdot \frac{\partial v_y}{\partial y} & \frac{\partial v_y}{\partial z} + \frac{\partial v_z}{\partial y} \\ \frac{\partial v_z}{\partial x} + \frac{\partial v_x}{\partial z} & \frac{\partial v_z}{\partial y} + \frac{\partial v_y}{\partial z} & 2 \cdot \frac{\partial v_z}{\partial z} \end{pmatrix} \tag{2.9}$$

Many models that depend on the rate of deformation have been developed, and they all arise from the general viscous fluid equation. Several of these models describe viscosity as a function of the invariants of the **2D** tensor. The first, second, and third invariants are represented as I_{2D}, II_{2D}, and III_{2D}. I_{2D} is zero for incompressible fluids, and III_{2D} is a measure of the degree of extensional flow. These two invariants will be assumed insignificant for the remainder of the flow behavior discussion. Models that assume the flow behavior is undergoing simple shear only include II_{2D}, and the following equation represents a general viscous fluid with rate of deformation dependency.

$$\boldsymbol{\tau}_{ij} = 2\mu \left(II_{2D} \right) \mathbf{D}_{ij} \tag{2.10}$$

When $\mu(II_{2D}) = \mu$, the equation reduces to the Newtonian flow condition. The power law, Equation 2.6, can also be represented in tensor form.

$$\tau_{ij} = k\left|II_{2D}\right|^{(n-1)/2}(2\mathbf{D}_{ij}) \tag{2.11}$$

When a fluid is undergoing steady simple shear, $II_{2D} = \left(\dot{\gamma}\right)^2$, thus simplifying Equation 2.11 to Equation 2.6.

Because the power law model predicts infinite viscosity at zero shear rate and zero viscosity at infinite shear rate, different models have been proposed that predict Newtonian behavior at the two limiting cases. The first of these models was developed by Cross and further refined by Yasuda and Carreau. Yasuda's model is

$$\frac{\mu - \mu_\infty}{\mu_o - \mu_\infty} = \frac{1}{\left[1 + k^a\left|II_{2D}\right|\right]^{(n-1)/a}} \tag{2.12}$$

where μ_o and μ_∞ are viscosities at zero and infinite shear rate, and a is a fitting parameter. This model is flexible and can be applied to many fluids.

Finally, fluids with yield stresses can also be expressed with the general viscous fluid equation. Two modifications have been made from the classical Bingham expression (Equation 2.7). Instead of a yield stress criteria, a critical strain rate can be used to separate the two flow regimes. The first regime is no longer represented as a Hookean solid, but instead as a highly viscous fluid

$$\tau = 2\mu\mathbf{D} \quad \text{for} \quad II_{2D}^{1/2} \leq \dot{\gamma}_c \tag{2.13a}$$

$$\tau = 2\left(\frac{\tau_y}{\left|II_{2D}\right|^{1/2}} + k\left|II_{2D}\right|^{(n-1)/2}\right)\mathbf{D} \quad \text{for } II_{2D}^{1/2} > \dot{\gamma}_c \tag{2.13b}$$

For purposes of computational fluid flow modeling, this equation is very useful because the fluid can be described as a viscous fluid for all rates of deformation, but there is a discontinuity at the critical shear rate, $\dot{\gamma}_c$. Computational fluid modeling is simplified with one constitutive equation for all ranges of shear rate, and Papanastasiou empirically modified Equations 2.13a and 2.13b by combining the two equations into one and eliminating the discontinuity with an exponential smoothing function.

2.1.5 Thixotropy

Discussion thus far has focused on using time-independent constitutive relationships, but another approach is the use of thixotropic (time-dependent) theory. Thixotropy has been defined in several ways, but the Joint Committee on Rheology of the International Council of Scientific Union defines it as: "A thixotropic system exhibits a time dependent, reversible, and isothermal decrease of viscosity with shear in flow." Reviews of thixotropy have been completed by Bauer and Collins and later by Mewis [22],[23]. Experimentally, thixotropy is an interesting phenomenon because during a transient shear rate experiment, the viscosity is different for an identical shear rate depending on the shear history. This behavior, when plotted as viscosity as a function of shear rate, gives rise to a hysteresis loop.

There are three main approaches for describing thixotropic fluids. Constitutive relationships (continuum theory) can be developed that are similar to the approaches in the previous section, except now they have a time dependence on past shear history. Slibar and Paslay developed a model similar to the Bingham expression, Equation 2.7, where the critical yield stress is a function of time [24]. However, the time dependence in their model is qualitative and has not been verified with experiments.

Another approach used in thixotropic modeling is based on internal structural kinetics. The structure of the material is undergoing change on a microscopic level; therefore, the material can be described with a stress equation that is not only a function of deformation rate but also the internal structure of the material. The internal structure can be described in an equation that is a function of shear rate and prior history [25]. Equations of this form are qualitative and do not include a yield stress term. Nonetheless, it is an interesting approach that has been used to describe suspensions, including semi-solid metal [26].

A third theory is the use of microstructure for determining rheological behavior. This approach is similar to the structural kinetic method, but the details about the microstructure are more detailed. The original work in this area was performed by Mooney on the size distribution of aggregates using the theory of slow coagulation during shear [27]. A few models of semi-solid have developed from this type of model. The original was developed by Kumar *et al.*, relating the breakdown of solid particles with shear and the agglomeration of particles with a sintering mechanism [28]. Recent modeling by Perez *et al.* of semi-solid metal was

similar, but argued that effective volume fraction is a function of the relative size of the particle aggregates, which are in turn a function of shear rate [29].

2.1.6 Experimental Work on Suspensions

It is obvious that there are several models for describing the flow behavior of suspensions, and these fluids have also been studied extensively experimentally. The primary instrument for examining flow behavior of suspensions (as well as fluids in general) is a viscometer, also referred to as a rheometer. In this text, the two terms will be used interchangeably. There are several types of viscometers that are used under a shear condition, and these can be divided into two categories: drag or pressure driven flows [1]. Both families of rheometers will be discussed in detail in this section.

Drag Flow Rheometers

A general drag flow rheometer consists of a fluid sandwiched between two obstacles, one of which is moving and the other is fixed, thus inducing a velocity gradient in the fluid. The shear stress on the fluid is measured, and the viscosity is subsequently calculated.

The sliding plate is the simplest of the drag flow viscometers. A fluid is located between two plates, and one of the plates is moved in the x-direction at a velocity, v_x, under a force, F. The distance between the plates in the y-direction is known; therefore, a shear rate can be determined from $\dot{\gamma} = dv_x/dy$. The shear stress equals the force divided by the fluid area, and using Newton's law of viscosity, Equation 2.5, the viscosity can be calculated. However, there are geometry constraints that make this rheometer unpopular, such as the fluid running out from between the plates, maintaining the plates in a parallel condition, and edge effects.

The rotational version of the sliding plate viscometer, the concentric cylinders or Couette viscometer, is the most common apparatus for examining fluids. A fluid is placed between two cylinders, one of which rotates. Depending on whether the outer or inner cylinder rotates, the viscometer is referred to as either a Couette or Searle type, respectively. The velocity gradient between the gap is analogous to the sliding-plate technique, and torque in the cylinder can be related to shear stress. This rheometer has several advantages over other types, most importantly that shear rate is constant across the gap such that viscosity is not a function of

position.

There are several other rheometers that fall under this category, including the rotational parallel-plate, cone and plate, and falling ball. Each are described in detail in Macosko [1], and they are all similar to the Couette viscometer with different flow geometries.

The Couette viscometer has been used for measuring suspensions, but there are limitations with its use. Particle segregation, lack of continuum flow, and inertial effects can affect concentric cylinder flow measurements.

Particles can diffuse because of concentration gradients or self diffusion (if the particles are small enough), and they can also diffuse from high to low shear stress regions. The moving cylinder is the location of the high shear stress; therefore, fluid with lower concentration of particles will dominate at the wall, and erroneous torque measurements will result. Viscous resuspension can occur when a suspension has segregated because of density differences [30]. Even though the particles have settled to the bottom of the Couette rheometer, they can resuspend into the liquid when the apparatus begins shearing again. Other researchers have reported concentration gradients in Couette devices because of particle size differences [31].

Another factor in the concentric cylinder apparatus is the particle size relative to the gap in the device. The velocity gradient is assumed to be linear, but when there is a particle that has a radius within an order of magnitude of the gap, step discontinuities develop in the velocity field [1]. Under this condition shear rate is no longer constant across the gap.

Inertial effects can also be significant in a Couette rheometer. The effects disappear after a short time, when the stress field reaches equilibrium. The time for establishing homogeneous, simple shear flow is a function of the fluid density, ρ, the gap in the viscometer, h, and viscosity, μ.

$$t_c = \frac{10\rho h^2}{\mu} \tag{2.14}$$

All of these effects lead to concerns about the interpretation of data collected from concentric cylinder viscometers on concentrated suspensions.

Pressure Driven Flow Rheometers

The other major type of shear rheometers are driven by a pressure gradient in the fluid. Pressure driven rheometers have non-homogeneous flow fields; therefore, viscosity and shear rate in

the fluid are a function of position. The original device for measuring viscosity, the capillary viscometer, was constructed in 1839. A fluid is squeezed at an applied pressure through a tube and exits the other end at a smaller pressure, normally atmospheric. The capillary rheometer is capable of achieving higher shear rates than many other viscometers. By measuring the flow rate and using the capillary tube dimensions, a simple relation is derived from the equation of motion for determining viscosity, where R is the tube radius, p_c is the pressure drop, L is the tube length, and Q is the volumetric flow rate.

$$\mu = \frac{\pi R^4 p_c}{8QL} \tag{2.15}$$

Like all rheometers, the capillary apparatus has inherent limitations. Because there is a shear stress gradient, particles migrate away from the wall to the middle of the tube. The lack of particles at the wall lowers the local viscosity and increases the likelihood of wall-slip of the fluid. Other potential problems are melt fracture, shear heating, and extrudate swell.

The experiments conducted in this work were performed with a different pressure driven flow rheometer, the parallel-plate compression viscometer. The next section provides details on this apparatus.

2.2 Parallel-Plate Compression Viscometer

The parallel-plate compression viscometer has been used to calculate viscosity of fluids for more than eighty years. Ira Williams is credited with inventing the device, also known as the parallel-plate plastometer, to characterize rubber [32]. The theory behind how the apparatus is used to determine viscosity for both Newtonian and non-Newtonian fluids will be discussed, along with a survey of fluids that have been characterized with the apparatus.

2.2.1 Newtonian Fluid

Derivation of the Parallel-Plate Solution

The equations of continuity and motion are used to describe the flow of an isothermal fluid. In general form, they are expressed as follows.

Continuity:

$$\frac{\partial \rho}{\partial t} = -(\nabla \cdot \rho \mathbf{v}) \tag{2.16}$$

In Equation 2.16, ρ is density, t is time, and $\mathbf{v}$ is the velocity vector. The equation states that the rate of mass flux into a volume element is equal to the change in density as a function of time. For an incompressible fluid, Equation 2.16 simplifies to $(\nabla \cdot \mathbf{v}) = 0$.

Motion:

$$\rho \frac{D\mathbf{v}}{Dt} = -\nabla p - [\nabla \cdot \boldsymbol{\tau}] + \rho \mathbf{g} \tag{2.17}$$

$\rho \frac{D\mathbf{v}}{Dt}$ is the mass per unit volume times acceleration

$-\nabla p$ is the pressure force on the element per unit volume

$-[\nabla \cdot \boldsymbol{\tau}]$ is the viscous force on the element per unit volume

$\rho \mathbf{g}$ is the gravitational force on the volume element

The equation of motion, Equation 2.17, is derived from a momentum balance on a volume element of fluid and is equivalent to Newton's second law. Written in scalar form, the equation of motion in cylindrical coordinates for an incompressible Newtonian fluid becomes

$$-\frac{\partial p}{\partial r} + \mu \nabla^2 v_r = \rho \frac{\partial v_r}{\partial t} \tag{2.18a}$$

$$-\frac{1}{r}\frac{\partial p}{\partial \theta} + \mu \nabla^2 v_\theta = \rho \frac{\partial v_\theta}{\partial t} \tag{2.18b}$$

$$-\frac{\partial p}{\partial z} + \mu \nabla^2 v_z = \rho \frac{\partial v_z}{\partial t} \tag{2.18c}$$

In 1874, Stefan published his seminal paper describing the flow of a Newtonian fluid compressed between two plates [33]. A quasi-steady state approximation is made ($\partial v_r / \partial \mathrm{t} = 0$), implying that inertial terms in the equation of motion are neglected, along with gravity. The radius of the fluid is assumed to be much larger than the height, therefore $r >> z$ and $v_r >> v_z$. Finally $v_\theta = 0$ because of circular symmetry. The equations of continuity and motion in cylindrical coordinates simplify to the following

Continuity:

$$\frac{1}{r}\frac{\partial}{\partial r}(rv_r) + \frac{\partial v_z}{\partial z} = 0 \tag{2.19}$$

Motion (r and z):

$$0 = -\frac{\partial p}{\partial r} + \mu\frac{\partial^2 v_r}{\partial z^2} \tag{2.20a}$$

$$0 = \frac{\partial p}{\partial z} \tag{2.20b}$$

Assuming there is no wall slip, Equation 2.20a is integrated twice with respect to z using the boundary condition $v_r = 0$ at $z = 0$ and at $z = h$, resulting in

$$v_r = \frac{1}{2\mu}\frac{\partial p}{\partial r}(z - h)z \tag{2.21}$$

The radial velocity is a parabolic function of the z-position in the sample. Using a mass balance,

$$-\pi r^2\left(\frac{dh}{dt}\right) = \int_0^h 2\pi r v_r dz \tag{2.22}$$

and substituting Equation 2.21 into Equation 2.22, followed by integration results in Equation 2.23.

$$\frac{\partial p}{\partial r} = \frac{6\mu r}{h^3}\left(\frac{dh}{dt}\right) \tag{2.23}$$

Integrating (∂p/∂r) with the boundary condition that $p = p_{atm}$ when $r = R$,

$$p - p_{atm} = \left(\frac{3\,\mu}{h^3}\frac{dh}{dt}\right)\left(r^2 - R^2\right) \tag{2.24}$$

When Equation 2.24 is integrated over the surface of the plate (Equation 2.25), an expression for the applied force, F, results as shown in Equation 2.26.

$$F = \int_0^R (p - p_0)\, 2\pi r dr = \int_0^R 2\pi r\left(\frac{3\,\mu}{h^3}\frac{dh}{dt}\right)\left(r^2 - R^2 dr\right) \tag{2.25}$$

$$F = \left(\frac{3\pi\mu R^4}{2h^3}\right)\frac{dh}{dt} \tag{2.26}$$

As the fluid spreads between the plates, R is increasing, but the volume of the sample, V, is constant. Substituting $V = R^2h$ into equation 2.26 results in the final expression,

$$F = \left(\frac{3\mu V^2}{2\pi h^5}\right)\frac{dh}{dt} \tag{2.27}$$

Equations 2.26 and 2.27 are each commonly referred to as the Stefan equation.

Most parallel-plate viscometers consist of a platen that rests on the fluid. In this configuration the force is the constant weight of the platen. Integrating Equation 2.27 as a function of time with constant force results in the solution,

$$\frac{1}{h^4} - \frac{1}{h_o^4} = \frac{8\pi F}{3\mu V^2}(t - t_o) \tag{2.28}$$

Experimentally, height is recorded as a function of time and viscosity is subsequently calculated.

Griffiths was the first to use Equation 2.28 for determining viscosity with the parallel-plate compression viscometer, using the simplified theoretical treatment of Healey [34]. Dienes and Klemm recognized that the Stefan solution of the equations of motion and continuity was the appropriate expression for describing the flow in the viscometer [35].

Calculation of Shear Rate

The shear rate of the fluid, $\dot{\gamma}$, for the parallel-plate geometry is defined as $\partial v_r/\partial z$. For a Newtonian fluid in compression, the shear rate is a function of both the radial distance from the center of the sample as well as the vertical distance from the centerline.

$$\dot{\gamma} = -\frac{6rz}{h^3}\frac{dh}{dt} \tag{2.29}$$

Because the shear rate varies in the sample, an average shear rate is determined by integrating the shear rate throughout the volume of the sample [36],

$$\dot{\gamma}_{av} = \frac{2\pi}{v}\int_0^R\int_0^{h/2}\dot{\gamma}r\,dr dz = \frac{R}{2h^2}\left(\frac{dh}{dt}\right) \tag{2.30}$$

A drawback of using this calculated shear rate is that the velocity profile of the fluid must be known *a priori* to take the partial derivative of v_r with respect to z. An expression for non-Newtonian shear rate has been derived that includes the power-law exponent.

2.2.2 Non-Newtonian Fluid

Power Law

Scott was the first to recognize that the parallel-plate viscometer could be used to determine flow parameters of non-Newtonian fluids [37]. The derivation is similar to the one above, except Equation 2.20a is altered to accommodate a non-Newtonian viscosity

$$0 = -\frac{\partial p}{\partial r} + \frac{\partial \tau_{rz}}{\partial z} \tag{2.31}$$

The stress tensor component τ_{rz} is expressed as,

$$\tau_{rz} = k\left(-\frac{\partial v_r}{\partial z}\right)^n \tag{2.32}$$

which can be integrated twice with the same boundary conditions in the Newtonian derivation above, thus resulting in an expression for the fluid velocity in the radial direction as given by Equation 2.33.

$$v_r = \frac{h^{1+(1/n)}}{1+(1/n)}\left(-\frac{1}{kr^n}\frac{dp}{dr}\right)^{1/n}\left[1-\left(\frac{z}{h}\right)^{1+(1/n)}\right] \tag{2.33}$$

Substituting Equation 2.33 into Equation 2.22 and integrating leads to the Scott equation, Equation 2.34.

$$F = \left(\frac{dh}{dt}\right)^n \frac{1}{h^{2n+1}}\left(\frac{2n+1}{2n}\right)^n \frac{\pi k R^{n+3}}{n+3} \tag{2.34}$$

Shear rate is also different in non-Newtonian fluids. The velocity profile is a function of the power law exponent, and the shear rate at any position in the fluid can be expressed in Equation 2.35.

$$\dot{\gamma} = -\frac{\partial v_r}{\partial z} = \frac{2\,(dh/dt)}{h^2}\left(\frac{2n+1}{2n}\right)\left(\frac{z}{h/2}\right)^{1/n} r \tag{2.35}$$

Equation 2.35 can be substituted into Equation 2.30 and integrated, thus resulting in an average

power-law shear rate.

$$\dot{\gamma} = \frac{R}{h^2}\left(\frac{dh}{dt}\right)\left(\frac{2n+1}{n}\right)\left(\frac{1}{3\,(1/n+1)}\right) \tag{2.36}$$

Bingham Plastic

In addition to deriving a solution for a power-law fluid, Scott developed a solution for a Bingham plastic in the parallel-plate compression geometry. Scott derived an expression for the pressure gradient in the radial direction which could not be solved without approximations [37].

$$(n+1)\left\{\frac{h}{2}\left(-\frac{dP}{dr}\right)-\tau_o\right\}^{(2n+1)/n} + (2n+1)\,\tau_o\left\{\frac{h}{2}\left(-\frac{dP}{dr}\right)-\tau_o\right\}^{(n+1)} \\ \frac{(n+1)(2n+1)}{n}\mu^{1/n}\left(\frac{-dP}{dr}\right)^2\frac{r(dh/dt)}{4} = 0 \tag{2.37}$$

An interesting conclusion of his work that is still in dispute today is the existence of a *yield surface.* In the compression geometry, the shear stress is maximum at the plates, and decreases to zero in the middle of the gap. Depending on the yield stress, only fluid near the plates and far from the z-axis yield, while regions on the radial and axial centerlines would travel as a plug. Researchers have argued that plug flow in a squeezing condition is impossible if continuity is maintained, while others have refuted this by claiming that the solid plug is actually a highly viscous fluid that maintains continuity. There is no experimental evidence of yield surfaces to date.

Covey and Stanmore developed a solution, Equation 2.39, using Scott's pressure gradient, Equation 2.37 for conditions where viscous flow dominates [38]. A dimensionless number, S, the modified plasticity number, compares viscous effects with yield stress effects for the compression geometry,

$$S = \frac{R\,(-dh/dt)\,\mu}{h^2\tau_o} \tag{2.38}$$

and when $S > 10$, an expression for force can be derived.

$$F = \frac{3V^2\mu}{2\pi h^5}\left(\frac{dh}{dt}\right) + \frac{\tau_o V^{3/2}}{\pi^{1/2}h^{5/2}} \tag{2.39}$$

For small values of S, (< 0.05), the expression for force, Equation 2.40, is different because the

yield stress component is the major resistance to flow,

$$F = \frac{2\pi\tau_o R^3}{3h} + \frac{4\pi}{7h^2}\left\{2\tau_o\mu\left(-dh/dt\right)R^7\right\}^{1/2} \tag{2.40}$$

and a limiting height, Equation 2.41 can be found that allows determination of a yield stress

$$h_L = \left(\frac{2V^{3/2}\tau_o}{3\pi^{1/2}F}\right)^{2/5} \tag{2.41}$$

Covey and Stanmore, besides deriving the previous expressions for a Bingham plastic, also derived equations for Herschel-Bulkley fluids. For $0.05 < S < 10$, they used a numerical method to solve the pressure gradient.

2.2.3 Experimental Studies

The parallel plate compression viscometer, which is referred to in the literature as the parallel-plate plastometer, parallel plate viscometer, transverse flow viscometer, compression viscometer, and the parallel-plate plastimeter, has been used to characterize the flow of numerous non-Newtonian fluids [39]. Originally built to characterize rubber, the apparatus has been used extensively to examine polymer melts (PE, PP, plasticizer, silicone elastomer, and thermosetting resin) [40]-[46], glass [47], semi-solid metal [36],[48]-[50], toothpaste [38], mayonnaise [51],[52], and mustard [52]. These studies were conducted with viscometers that used either the constant force or constant compression velocity methods. An example of viscosity results produced by the parallel-plate compression viscometer can be seen in Figure 2-4 [40]. Other researchers have tried to make the rheology analysis of the instrument more robust by examining effects such as wall-slip, but the basic equations for describing flow have remained relatively unchanged. The equations that determine viscosity all require a no-slip boundary condition, and many current studies have developed corrections for wall-slip and partial wall-slip [43],[53].

The parallel-plate viscometer is widely accepted as an instrument for characterizing the flow behavior of high viscosity, non-Newtonian fluids. The flow geometry is complex, and there is normally a mix of shear and extensional flow, thus making comparisons of different fluids difficult. As a result, the apparatus has been referred to as an indexer and not a viscometer.

The maximum shear rate that has been achieved with the apparatus is less than 50 s^{-1}, and the fluid must have significant viscosity so it doesn't run out from between the plates before a test is complete. Still, researchers have found the instrument highly useful in characterizing a fluid as a function of variables that closely resemble process conditions.

2.3 Rheology of Semi-Solid Metal Alloys

2.3.1 Background of Semi-Solid Metal

The discovery that the microstructure of metal alloys in the two phase solid/liquid state could be manipulated to allow forming was first reported by Spencer *et al.* at MIT in the early 1970's [54]. It was noticed that instead of the normal dendritic microstructure, a globular, equiaxed grain structure was formed when shearing a tin-lead metal alloy as it cooled from the liquid state. The non-dendritic alloy exhibited lower viscosity than a dendritic alloy at the same fraction solid and required much lower forming pressures to induce flow. It was quickly realized that this phenomenon had large commercial potential, which was summarized by Flemings in his seminal review paper [55].

Flemings summarized the main advantages as: (1) lower heat content than liquid metal, (2) solid present at time of mold filling, (3) viscosity higher and more controllable than in liquid metals, (4) flow stress lower than for solid metals, (5) ability to incorporate other materials, and (6) the ability to separate liquid and solid. Each of these characteristics has numerous potential commercial benefits, and they are summarized in Table 2-1.

There are two primary processing methods for forming semi-solid metal. Forming the semi-solid structure directly from the liquid alloy and subsequently processing is called *rheocasting.* Producing the semi-solid structure, cooling, and then reheating the alloy prior to casting is referred to as *thixocasting.* The difference has significance when describing a rheological experiment and will be referred to in the following section.

There are two primary commercial routes for rheocasting aluminum for thixocasting. The magnetohydrodynamic (MHD) process stirs the aluminum melt with electromagnetic fields while the alloy freezes in a continuous caster, thus achieving the desired non-dendritic microstructure. Besides MHD, the other main process is the strain-induced melt activation

(SIMA) method. Billets of aluminum are cold worked so that upon reheating, recrystallization creates globular solid grains. A technique recently developed at MIT was used to create custom alloys in this thesis [56]. The new process relies upon nucleation of solid grains on a rotating copper chill. The recent review of Pan *et al.* summarizes other novel processing methods that are used to rheocast semi-solid alloys [57].

2.3.2 Rheological Experiments

The third advantage mentioned by Flemings, the higher and controllable viscosity, has been the primary focus of research in the semi-solid field for the last thirty years. The potential of semi-solid processing has been inhibited because understanding of the fluid behavior has been incomplete. Similar to concentrated suspensions, rheological studies of semi-solid alloys have led to differing conclusions and multiple fluid-flow models.

Rheological experiments have focused on varying time scales and temperature ranges of semi-solid alloys. Experiments can be broken into steady-state or transient measurements, and high ($> 60\%$ solid) or low fraction solid. These definitions can be as arbitrary as they sound, and there is still not complete agreement on the divisions of the categories.

Steady-State Rheological Experiments

Suspensions, and therefore metal slurries, behave differently depending on the geometry and flow conditions of the experiment. Early studies on semi-solid alloys were mostly conducted with concentric cylinder rheometers, and the semi-solid material was produced *in-situ* with mechanical stirring as it cooled from the liquid state. Important information was gathered on the apparent viscosity and how it related to cooling rate, shear rate, particle size, entrapped eutectic liquid, and time-dependent effects. Researchers determined that the material was highly thixotropic, with a large decrease in apparent viscosity upon shearing. Breakdown of agglomerated particles along with coarsening and subsequent decrease of particle surface area decreased the viscosity. The steady-state viscosity has been described with a shear thinning, power law equation, and early studies have been summarized in detail in the review paper of Flemings [55].

An original experiment that stands out from the early studies is the work of Laxmanan and

Flemings [36]. Using a parallel-plate compression viscometer, Sn-15%Pb was examined at low shear rates over a wide range of fraction solid, 0.30 to 0.60. A power-law model was curve fit to the data as a function of shear-rate and fraction solid (Equation 2.42),

$$\mu = a \exp(b f_s) \dot{\gamma}^{(c f_s + d)} \tag{2.42}$$

and the test was the first conducted on a reheated, rheocast semi-solid. Shear rates attained during the test were low, less than 1 s^{-1}.

Kattamis and Piccone conducted experiments on an Al-Cu-Mg alloy with a Couette rheometer and developed a model for viscosity that was not a only a function of fraction solid and shear rate but also of particle morphology [58]. In their experiment, slurry was drawn into a tube and quenched such that particle morphology could be determined for a given condition of shear rate and fraction solid. Particle size and shape were characterized and compared relative to their starting conditions. Equation 2.43 is the viscosity model they derived,

$$\mu = \mu_o \left(1 + \frac{K f_s \left(S_v / S_{v0}\right) \left(d / d_o\right)}{K - f_s} + 2.0333 \times 10^4 f_s \left(\dot{\gamma}\right)^{-0.727} \right) \tag{2.43}$$

where μ_o is the liquid viscosity, K is a constant, and (S_v/S_{v0}) and (d/d_o) are the globular shape and size, respectively, for a given time and shear rate during an isothermal test.

Transient Rheological Experiments

Since the late 1980's, there has been a large focus on characterization of semi-solid alloys using transient rheological experiments. In the thixotropy review paper of Mewis, it is stated that there are three main tests that can be used to characterize thixotropic fluids: (1) a step function in shear rate or shear stress, (2) a consecutive linear increase or decrease in shear rate, or (3) a sinusoidal change in shear rate [23]. Researchers have used the first type of transient experiment extensively in the semi-solid field, and the important findings of these studies will be summarized in the following paragraphs.

Concentric Cylinders Semi-solid alloys tested in a concentric cylinder viscometer are always *in-situ*, rheocast material. The first transient experiment using a Couette rheometer was

performed by Turng and Wang on Sn-15%Pb alloys up to a fraction solid of 0.57 with a 1.26 mm gap [59]. They found a Newtonian viscosity limit at shear rates above 1000 s^{-1}, and similar to other previous researchers, reported that the steady-state flow behavior is shear thinning. An interesting observation from their experiments is the evidence of a torque spike after a step increase in shear rate. The shear stress overshoot or undershoot transient time is relatively constant if the shear rate is either being increased or decreased.

Kumar *et al.* examined Sn-15%Pb and Al-7%Si-0.6%Mg during numerous transient experiments with fractions solid ranging from 0.3 to 0.45 in a 3 mm gap Couette rheometer [28],[60],[61]. The major conclusion of their work was that semi-solid fluid behaved in a dilatant, or shear thickening manner, if the structure could be considered constant (isostructural) for short durations. They claimed that the torque spikes observed in Turng and Wang's work corresponded to this isostructural, dilatant behavior. Figure 2-5 is a qualitative plot of shear stress as a function of shear rate and material structure. An isostructural fluid would exhibit shear thickening, and a fluid that is disagglomerating would be shear thinning. A model was developed that utilizes a structural parameter, s, that describes the connectivity of the solid particles in a semi-solid alloy, similar to the structural kinetic models described in the thixotropy section.

$$\tau_{ij} = f\left(\dot{\gamma}, T, s\right) \tag{2.44}$$

$$\frac{ds}{dt} = g\left(\dot{\gamma}, T, s\right) \tag{2.45}$$

Based on Equation 2.44, a fully developed constitutive equation was derived that accounts for agglomeration and disagglomeration of the solid phase in the liquid and the maximum volume fraction:

$$\tau = A(s)\frac{(c/c_{\max})^{1/3}}{1-(c/c_{\max})^{1/3}}\mu_o + (n+1)\mu_o^{n+1}C(T)sf_s\dot{\gamma}^n \tag{2.46}$$

where $A(s)$ is a hydrodynamic coefficient dependent on particle morphology, c is an effective solid fraction function, $C(T)$ is the power law coefficient, μ_o is the liquid viscosity, and s is the structure parameter (Equation 2.46). The structure parameter ranges from zero to one, with one being a fully agglomerated state and zero representing when none of the particles are connected. Their experimental evidence was supported by others that the kinetics of agglomeration are slower than disagglomeration and reported a break-down time on the order

of seconds [62]. This, however, disagrees with the result of Turng and Wang that transients after a stress overshoot or undershoot are equivalent.

There have been several other studies with concentric cylinder rheometers during the last decade. McLelland *et al.* conducted experiments on tin-lead alloys at a fraction solid of 0.36 and reported a negative power-law exponent, $n < 0$ [63]. This corresponds to a decrease in shear stress with increasing shear rate, which is an experimental result that was also reported by other researchers [64],[65]. McLelland determined that semi-solid metal slurries are the only fluids to report this behavior in the literature, but in the review of Mewis, there are two references of fluids that exhibit this behavior. McLelland reported that the low values of n were found in experiments at shear rates less than 200 s^{-1}, as opposed to other researchers who reported positive n-values at higher shear rates. Using a modified version of Figure 2-5 that included a yield stress, McLelland argued that rapid structural breakdown could lead to a decreasing shear stress with increasing shear rate.

Quaak *et al.* performed experiments on A356 and composites of this alloy at fractions solid between 0.2 and 0.4 at shear rates ranging from 0.4 to 210 s^{-1} [64]. They found a steady-state power law exponent less than zero, and they determined a transient, isostructural n-value that was less than one, thus disagreeing with Kumar.

Mada and Ajersch conducted a series of experiments on A356 composites and used a structural kinetic equation developed in previous work to explain the thixotropic nature of semi-solid metal. They qualitatively stated that the large decrease in shear stress at early times during a test was accounted for by disagglomeration and liberation of entrapped liquid, effectively increasing the volume fraction of liquid and decreasing resistance to flow [26],[62].

Peng and Wang conducted a series of experiments on Sn-15%Pb at a fraction solid range of 0.20 to 0.54, and described the fluid flow behavior with a Herschel-Bulkley model [66]. Yield stress values were in the range of 10 to 100 Pa, and n-values ranged from 0.73 to 0.84. They also reported transient times during shear stress overshoots (or undershoots), but the values were the same for both increasing and decreasing experiments.

Another recent study by Modigell *et al.* supported the findings of Kumar that the fluid behavior was shear thickening at constant structure. Modigell used a 2.5 mm gap Couette rheometer on Sn-15%Pb alloys at fractions solid ranging between 0.35 and 0.50 and shear rates

as large as 225 s^{-1} [67].

There have been several studies performed with concentric cylinder rheometers on various alloys and shear rate ranges, but there is still disagreement on how to interpret the results. Spikes in torque readings that last for various durations have lead to the belief by some that the suspension is acting in a shear thickening manner, while others have suggested that torque spikes are an artifact of rotational instruments, either because of wall slip or agglomeration of particles across the gap. Some have interpreted that there is a yield stress, but everyone agrees that the behavior of the material after continuous shearing is pseudoplastic.

In addition to experiments involving *in situ* rheocast material, studies have been performed on reheated semi-solid alloys with techniques other than the Couette rheometer such as the parallel-plate compression viscometer, the back-extrusion method, and various unconventional approaches.

Parallel-Plate Compression Viscometer Besides the original work of Laxmanan and Flemings [36], other studies have been conducted with the parallel-plate compression approach. Mada and Ajersch used the parallel-plate viscometer with constant velocity on composites of A356 and SiC at low shear rates, less than 2 s^{-1} [48]. An important observation from their work is that they reported less segregation of liquid and solid at high compression speeds and low fractions solid.

A derivative of the parallel-plate compression viscometer was built by Kapranos *et al.* [50]. Using high speed load cells, force was measured at high frequency while a sample with a diameter of 36 mm and height of 42 mm was compressed at speeds of 0.5 m/s, thus producing an average shear rate of up to 200 s^{-1}. The instrument was used on A356 at temperatures near the eutectic melt temperature, and viscosity was calculated using the Stefan solution, Equation 2.27. Using the commercial fluid dynamics software FLOW-3D® (registered product of Flow Science, Inc., Sante Fe, NM), a mesh geometry was created that imitated the physical experiment. The computer software calculated a force on the fluid for a given viscosity model. The force results from the experiment were compared with the model until it was determined that a specific fluid viscosity model adequately represented both data sets. Using this iterative technique, fluid model parameters could be assigned for a given alloy and temperature. An interesting

observation of their experimental work was the large difference in force during impact depending on whether the eutectic phase was melted. Above the eutectic melt plateau, there was no noticeable spike in force at impact.

A recent study by Pan and Apelian using parallel-plate compression concluded that semi-solid slurries possess a finite yield stress [68]. Above the eutectic melt temperature, the yield stress was determined to be on the order of 100-1000 Pa, agreeing with earlier work by Sannes *et al.* using a vane rheometer [69].

Back-Extrusion Technique Loué *et al.* developed a novel technique referred to as the back-extrusion method [49]. A semi-solid metal is reheated inside of a cylinder and then compressed with a piston. The fluid extrudes up around the sides of the piston and the force is recorded as a function of piston height. Viscosity is calculated from this data, and high shear rates can be attained on the order of 1000 s^{-1}. Loué reported that below a critical ramming velocity, segregation of liquid took place that was followed by a densification of the solid phase, and above this critical velocity, fluid flow was homogeneous. They also reported that they did not see segregation in low speed parallel-plate compression studies, and that lubricated grain sliding was probably the dominant flow mechanism because there was no evidence of plastic deformation of the grains. Other researchers have used back-extrusion on magnesium alloys and Sn-15%Pb [70],[71].

Capillary, Indentation, Vane, and Parallel-Plate Rotational Methods There have been many other attempts at examining fluid behavior of semi-solid metal using unconventional approaches. Capillary studies have been conducted by several researchers [72],[73], and results show a shear thinning behavior at high shear rates. Such experiments are difficult to control because of freezing in the tube and maintaining an isothermal condition. Furthermore, wall slip appears to be significant for this apparatus.

Indentation has also been used by researchers to determine force versus strain curves [74],[75]. Indentation is a non-homogeneous test, and extracting useful rheological data is difficult.

Another method that has been used to measure rheological properties is the vane method. The vane method is a type of shear rheometer that consists of a rotating vane placed inside of the

fluid. Torque is measured, and although the shear stress field is highly inhomogenous, viscosities and yield stress can be determined Nguyen and Boger used this technique on suspensions and were able to measure a yield stress [21]. Sannes *et al.* performed experiments on magnesium alloys at a wide range of fraction solid, and reported values in the range of 100 to 100,000 Pa for fractions solid between 0.3 and 0.7 [69].

de Figueredo, Kato and Flemings at MIT recently conducted experiments with a parallel-plate rotational viscometer on reheated rheocast A357 at shear rates between 100 and 1000 s^{-1} [76]. The apparatus could examine semi-solid material that was created *in situ* with mechanical stirring or reheated, commercially rheocast alloy. This device was chosen because shear rate could be varied by either increasing the RPM rate of the plate or decreasing the gap between the plates. Stress overshoot or undershoots were not detected, leading to their conclusion that semi-solid metal alloys behaved in a shear thinning manner even at fast transients. Their calculated viscosities on reheated rheocast alloys were lower than values found by the back-extrusion technique on reheated material, but higher than steady-state measurements on alloys that had been cooled from the liquid state.

2.3.3 Other Relevant Work on Semi-Solid Alloys

Besides rheological studies, experiments have been conducted on alloys in the semi-solid state with the intention of understanding the fundamental mechanisms at work during deformation and flow of the alloy. In this section, important results from recent work will be highlighted.

Nature of the Solid Phase Network

Grain Boundary Wetting The microstructure of an alloy that is prepared for semi-solid forming is characterized by a globular, solid phase that is surrounded by liquid which is of near eutectic composition. Depending on the surface energies of the solid/solid interface (γ_{ss}) and the solid/liquid interface (γ_{sl}), two adjacent particles at high volume fraction will either form a wetted or non-wetted grain boundary. If the surface is non-wetted, diffusional processes will eliminate the grain boundary and the particles will coalesce by a sintering process [77].

A grain boundary will wet if $2\gamma_{sl} < \gamma_{ss}$ because the surface energy for creating two solid-liquid surfaces is less than one solid-solid boundary. Partial wetting occurs if a small dihedral

angle, ϕ, forms when the surface energy of two liquid surfaces is slightly larger than one solid-solid surface. This is apparent in Equation 2.47.

$$\gamma_{ss} = 2\gamma_{sl} \cos\left(\frac{\phi}{2}\right) \tag{2.47}$$

When $\phi > 60$ degrees, the liquid forms a lens at the grain boundary, and the interface is essentially non-wetted.

In metals, low-angle grain boundary energies are small, on the order of 0 to 0.1 J/m^2, depending on the grain boundary angle. Gündüz and Hunt experimentally determined surface energies of solid-solid and solid-liquid interfaces in the Al-Si, Al-Cu, and Pb-Sn binary systems [79]. High angle grain boundary energies for each system were slightly less than twice the solid-liquid surface energy, inferring that partial wetting occurs in these alloys. However, Al-Si and Al-Cu solid-liquid surface energies were about 0.16 J/m^2, therefore low-angle grain boundaries would not wet.

According to German, in liquid phase sintering, the strength of sintered particles is highly dependent on the neck size to particle diameter ratio (X/D) [78]. The neck size is a function of the dihedral angle, shown in Equation 2.48.

$$\frac{X}{D} = \sin\left(\frac{\phi}{2}\right) \tag{2.48}$$

The sinter bond strength is proportional to the fourth power of the neck to particle size ratio, thus a small difference in wetting angle can lead to large variations in strength.

3-D Morphology Studies Ito *et al.* determined from a series of micrograph sections on Al-6.5%Si that the solid phase is more agglomerated than what appears in two-dimensional micrographs [80]. Ito imaged the surface of the sample at 40 μm intervals and constructed a three-dimensional representation of the structure. Grain boundary films are on the order of 1 μm, and more refined work was conducted by Wolfsdorff *et al.* on Sn-Pb alloys [81]. Using microtomography, three-dimensional structures were created from sections at varying coarsening times. In addition to wetted and non-wetted boundaries, they determined that grains could be partially wetted. Essentially every particle in the network is contacted at

high volume fraction, but the stability of the network can increase if they are connected by non-wetted boundaries to multiple particles.

Arnberg *et al.*, using electron backscattering diffraction (EBSD) determined the agglomeration of the solid phase in the aluminum alloy 6082 [82]. EBSD allows for the characterization of grain boundary angle between primary phase grains. Agglomeration increased with the amount of stirring during solidification because of increased coarsening and the higher probability that low-angle grain boundaries would occur. The percentage of boundaries that were low-angle as a function of the total number of boundaries ranged from 3.2 to 18.3%, and the EBSD was performed on a single 2-D section, thus limiting its usefulness in determining connectivity.

Verrier *et al.* investigated A357 with EBSD and x-ray tomography [83]. X-ray tomography has a resolution of 2 microns, an order of magnitude better than the work of Ito or Wolfsdorff. They made several major conclusions from their work about connectivity of particles before and after deformation. They found that reheated rheocast alloys have a large degree of agglomeration of particles before deformation, and in one particular sample, two agglomerates accounted for more than 60% of the solid phase. After slow compression there was only one agglomerate, and it accounted for more than 90% of the solid phase. At higher rates of unconstrained compression, the amount of agglomeration decreased.

Physical Mechanisms of Semi-Solid Fluid Flow

Chen and Tsao proposed four possible mechanisms for flow of semi-solid alloys [84]. They are (1) liquid flow, (2) flow of liquid incorporating solid particles, (3) sliding between solid particles, and (4) plastic deformation of solid particles. Compression experiments were conducted on A356 at temperatures of 570 and 575 °C and strain rates of 0.001 and 0.01 s^{-1}. As fraction solid and deformation rate increased, they determined that sliding between solid particles and plastic deformation were the dominating mechanisms. They found less segregation of liquid and solid at increasing deformation rates, similar to the works of Mada and Loué [48], [49]. Segregation was determined from fraction solid calculations using optical micrographs and the lever rule.

A more extensive experimental study was conducted by Tzimas and Zavaliangos on Al-Cu alloys at strain rates of 0.1 and 1 s^{-1} in the fraction solid range of 0.60 to 0.95 [85]. Force

was measured as a function of strain, and it was observed that a peak stress occurred at all fractions solid at a strain less than 0.10. As the fraction solid increased, the peak stress increased, and macroscopic cracking of the sample occurred. The Al-Cu binary alloy had larger peak stress values than the A2014 alloy which had Fe-Mn precipitates at its grain boundaries. The binary alloy also exhibited larger amounts of cracking for a given fraction solid relative to the commercial alloy. They did not observe phase segregation in these experiments.

Tzimas and Zavaliangos conducted shear rate jump experiments on the two Al-Cu alloys, increasing the shear rate from 0.1 to 1.0 s^{-1} during a test. After the stress value reached a plateau during compression, the strain rate was increased, and the stress increased to a new value. The stress decreased to a new plateau that was larger than the original at high fraction solid, but at a critical fraction solid, both plateau stresses were equal and independent of strain rate. The critical volume fraction for A2014 and Al-4%Cu were 0.80 and 0.60, respectively, and this value represents the upper limit of semi-solid alloy processability.

Maximum Volume Fraction The highest volume fraction solid that can be processed has not been determined, and there are conflicting results in the literature. Most rheological studies that used a Couette apparatus report a value of 0.60 for convenience. Kumar *et al.*. [60] used a value of 0.64 based on the theoretical random packing fraction of hard spheres calculated by Shapiro and Probstein [86]. Shapiro and Probstein stated that at high shear rates the packing fraction has been reported between 0.55 and 0.71. From their findings there is not one well-defined packing limit which is a function of the size distribution of the solid particles, but several depending on the degree of short range ordering.

Semi-solid metal, both dendritic and non-dendritic, has been examined by researchers for better understanding of the solidification process in a casting. The *coherency* temperature is defined as the fraction solid where a solid grain can no longer travel great distances in the liquid because it is constrained by other grains [87]. Above the coherency fraction solid, grains can rearrange by sliding past each other with relative ease. Grain boundary motion can occur in pure aluminum grain boundaries with small amounts of stress. Winning *et al.* reports that at 600 °C grain boundaries can migrate, and at this temperature low angle grain boundaries have a higher mobility than high angle grain boundaries [88]. The mobility of a low-angle grain

boundary in units of μm/sMPa is between 500 and 600, which is fast enough to allow grains to realign into close packed structures. Arne and St. John determined that at a fraction solid above the coherency level, a maximum packing fraction solid is attained [87]. At this point, grains can no longer rearrange, and yield strength increases dramatically. There is insufficient liquid during deformation, resulting in fracture, cracking, and porosity during deformation. The coherency and maximum packing fractions solid are functions of the particle shape and size.

2.4 Summary

The previous sections covered three major topics: concentrated suspensions, the parallel-plate compression viscometer, and the behavior of semi-solid metal alloys. Each has a significant role in describing the importance of this thesis: the examination of the fluid flow behavior of semi-solid alloys at high shear rates.

Suspensions have been studied a great deal since the work of Einstein at the beginning of the last century, yet there is still a large amount of disagreement on how to physically model suspensions and how to experimentally characterize them. Numerous models were presented, each with advantages and limitations. Experimentally, characterization of concentrated suspensions is difficult because of non-homogeneities in the flow behavior. Various viscometers were compared and contrasted.

The parallel-plate compression viscometer was discussed in great detail in the second section of this chapter as a technique for examining concentrated suspensions. Although the shear stress and shear rate are functions of position in the fluid during an experiment with the parallel-plate instrument, this rheometer more closely resembles industrial process conditions. The derivation of how viscosity can be determined for Newtonian and non-Newtonian fluids with the apparatus was shown, as well as previous experiments with the device.

The third section summarized the recent experimental studies with semi-solid metal alloys. Rheological experiments on semi-solid alloys have lead to varying conclusions about the flow behavior; some researchers have characterized the flow behavior as shear thickening and others as shear thinning during transient states of shear. Still others have introduced the concept of

a yield stress, even at low to medium fraction solid. Besides the rheological work, experiments on the mechanisms to the flow behavior have been conducted.

There is clearly a need to characterize the flow behavior of semi-solid alloys at high shear rates to complement the rotational viscometer techniques. Previous compression tests have either been at low speeds or lacked data acquisition techniques for extracting rheological data. A new viscometer has been built at MIT with a novel method for calculating applied force that helps answer some of the fundamental questions about the fluid flow behavior of semi-solid alloys.

CHARACTERISTIC	POTENTIAL BENEFIT OR APPLICATION
Lower heat content than liquid metal	Higher speed part forming
	Higher speed continuous casting
	Lower mold erosion
	Ferrous part forming
	Forming of other high-melting-point materials
	Forming of reactive metals
Solid present at time of mold filling	Less shrinkage voids
	Less feeding required
	Less macrosegregation
	Fine grain structure
Viscosity higher than in liquid metals, and controllable	Less entrapped mold gases
	Reduced oxides - improved machinability
	Less mold attack
	Higher speed part forming
	Improved surface finish
	Automation
	New processes
Flow stress lower than for solid metals	Forming of intricate parts
	High speed part forming
	Lower cost part forming
	High speed forming of continuous shapes (e.g.
	extrusion)
	New processes
Ability to incorporate other materials	Composites
Ability to separate liquid and solid	Purification

Table 2.1: Characteristics of semi-solid metals for future exploitation [54].

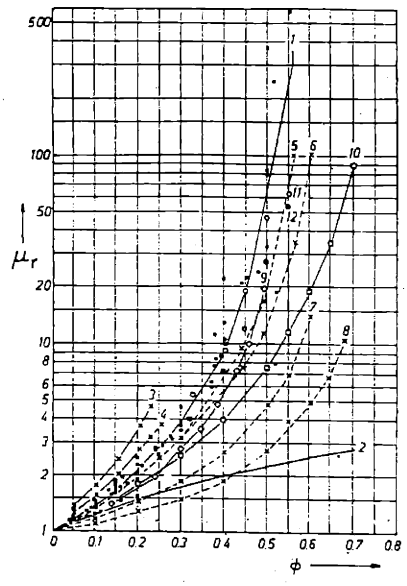

Figure 2-1: Data collected by Rutgers of relative viscosity of suspensions as a function of volume fraction [4]. The numbers on the curves correspond to specific experimental studies.

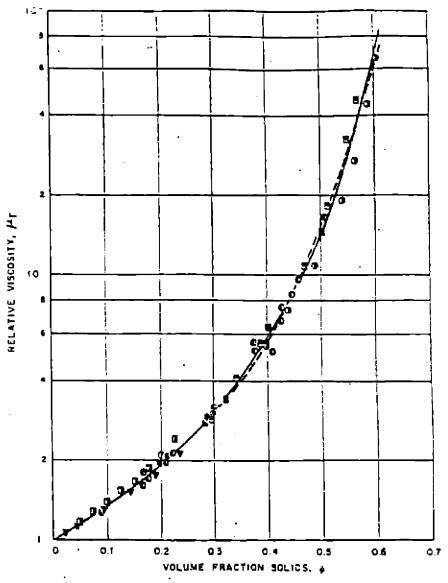

Figure 2-2: Data of various research studies collected by Thomas [5] and subjected to extrapolation to account for differences seen in previously reported results (Figure 2-1). This curve does not agree with the average viscosity value in Figure 2-1.

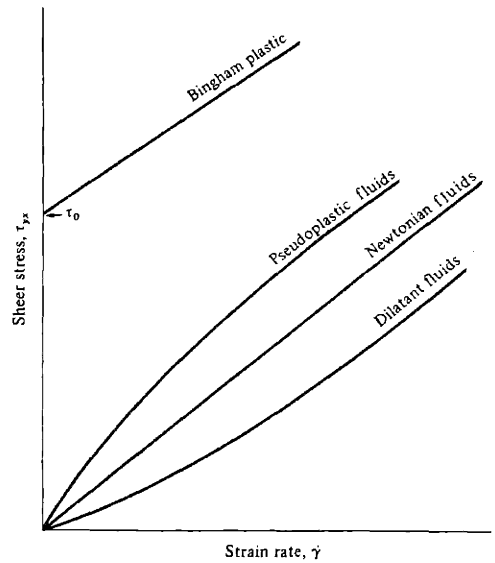

Figure 2-3: Relationship of stress versus strain rate for different types of fluids. Newtonian, pseudoplastic, dilatant, and Bingham plastic are each represented [12].

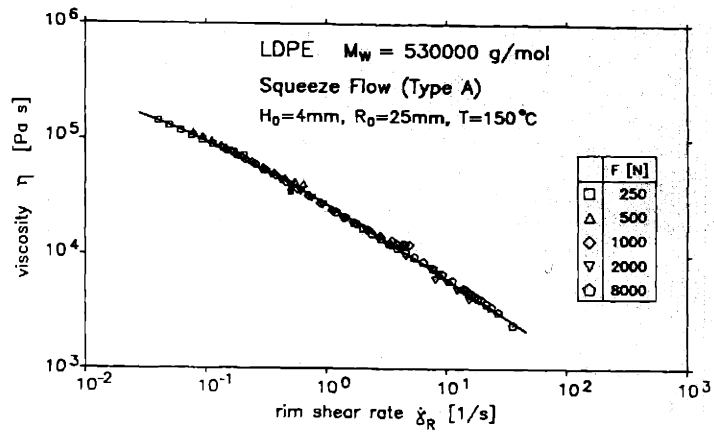

Figure 2-4: Experimentally determined viscosity of LDPE using the parallel-plate compression and capillary viscometer [40].

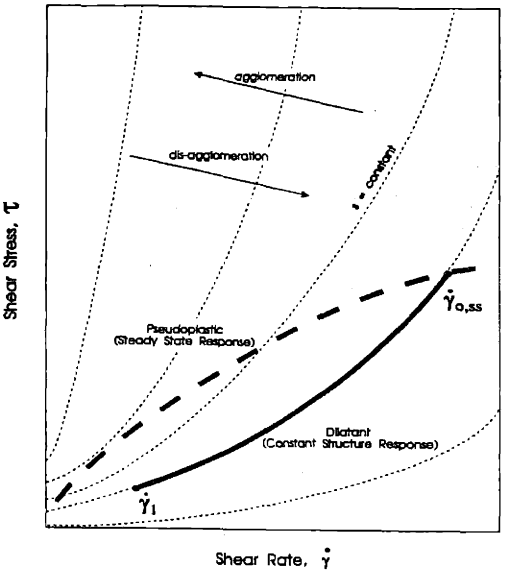

Figure 2-5: Qualitative plot of shear stress as a function of shear rate and particle agglomeration [28]. Isostructural behavior is represented as dilatant, while disagglomeration is pseudoplastic.

Chapter 3

Experimental Method

A novel viscometer was designed and constructed to experimentally study the fluid flow behavior of semi-solid slurries at transient, high shear rates. The apparatus, known as the Drop Forge Viscometer (DFV), has a geometry similar to a parallel-plate compression viscometer but can achieve much higher shear rates. The following chapter describes the DFV, the materials that were examined, and the experimental procedure. The calculation of viscosity is discussed, along with analysis of the assumptions used to make the solution tractable.

3.1 Drop Forge Viscometer

3.1.1 Apparatus

The DFV consists of a lower platen and an upper platen, with an attached platen rod to track platen motion with time. All components are contained within an air recirculating furnace to maintain the apparatus in an isothermal condition. The drop forge viscometer is thus similar to the parallel-plate compression viscometer except that the upper plate is allowed to fall under the influence of gravity, unlike the more conventional approach of resting the upper plate on the sample. Figure 3-1 is a schematic of the DFV, which is located inside of an air-recirculating furnace. The lower steel platen rests on two rectangular steel tubes, thus suspending the plate an inch above the furnace floor. The gap between the furnace chamber and platen allows for easy removal of the plate and sample following testing.

The five-inch diameter upper platen is fabricated from steel. This platen is coated with

layers of graphite and boron nitride to prevent sticking of the sample. Extra mass can be added to the DFV by placing steel discs of known mass on top of the upper platen. The plate connects to the stainless steel threaded rod, which extends out of the top of the furnace, self-aligning the upper platen through a graphite sleeve that minimizes friction. The rod is suspended with an adjustable solenoid, which controls the z-position of the upper platen before compression.

A high speed digital camera, the Kodak Ektapro 4540 Motion Analyzer, rests on a platform that attaches to the furnace assembly and images the rod as it falls. A photovoltaic sensor attached to the furnace triggers the camera when the rod achieves a specified position. After completion of the test, a laptop PC downloads images in TIFF format from the camera via a GPIB acquisition board and a National Instruments Labview software interface.

3.1.2 Data Acquisition

The primary data from the experiment are digital images of the falling rod. The position of a marker affixed to the rod can be related to the height of the sample during an experiment because it is strategically placed to fall in the field of view of the camera during sample compression inside the furnace. The rod is backlit by a 300W floodlight, and the marker appears as a sharp, dark edge on the rod. The TIFF images with 264 x 64 pixels of 8-bit resolution are captured at a rate of 18,000 frames per second. Because of the 8 bit resolution, each pixel stores a relative intensity value of between 0 and 255. On average, between 100 to 200 images are downloaded for data analysis corresponding to a test duration of between 5.56 and 11.1 ms. Figure 3-2 presents raw images acquired with the high speed camera. The marker is clearly discerned from the rod, and the rate of change in displacement of the marker decreases with time, indicative of deceleration.

3.1.3 Temperature Control

The air-recirculating furnace chamber has a volume of 1.5 cubic feet and a temperature accuracy of ± 2 °C. Thermocouple measurements taken from different positions in the furnace verify that the temperature range is within the predicted error, and varies less than half a degree in the volume range of a test sample. The sample is estimated to be within ± 0.5 °C of the measured

temperature.

3.2 Materials

Four rheocast aluminum alloys produced by three different process routes were studied in this work. In commercial semi-solid casting, the most commonly used materials are the hypo-eutectic, aluminum-silicon alloys A357 and A356. The A357 used in the experiments was produced by both the SIMA (strain induced, melt activated) and the MHD (magnetohydrodynamic) methods, the two most common processing techniques. The majority of experiments were conducted with the SIMA prepared material. The other three alloys, A356, A356 diluted with pure aluminum, and binary Al-4.5wt%Cu, were rheocast at MIT using a new technique. The nominal compositions are listed in Table 3-1. All samples were machined into cylinders with a diameter of 25 mm and a height of 15 mm.

3.2.1 Commercial Rheocast A357

The A357 SIMA material was purchased in 25 mm diameter billet from Alumax (acquired by Alcoa). A 1.5 meter rod was chemically analyzed at three different cross-sectional locations along the length for composition, and the results are listed in Table 3-1. Samples for the viscometer study were cut to the proper height from the billet using an abrasive saw. Figure 3-3 is a plot of the fraction solid versus temperature for two A357 alloys with differing Si content, as determined with the computational thermodynamic software Thermo-Calc® (Appendix A) [89]. It can be seen in the figure that a small change in silicon content (0.25wt%) causes a difference of approximately 0.02 f_s in the fraction solid range $0.40 < f_s < 0.50$. The eutectic phase begins to freeze over a narrow temperature range (large df_s/dT) at about 0.55 fraction solid, thus limiting the experimental studies to fractions solid below this value.

The A357 MHD material was also produced by Alumax. Composition near the middle and outer edge of a slug was determined from chemical analysis (Table 3-1). Because of the cross-sectional variation in silicon content, the cylindrical samples were machined from the core of a 3 inch diameter slug.

3.2.2 MIT Rheocast Alloys

A new rheocasting process was invented at MIT in April 2000 and was employed to make customized alloys [56]. In the technique, a rotating copper rod is inserted into a melt that is a few degrees above its liquidus, and after only a few seconds, a spheroidal, non-dendritic microstructure is produced. This is in stark contrast to conventional mechanical stirring approaches that require agitation for much longer periods of time. Three alloys were prepared for this study using the MIT technique: A356, A356 diluted to 4.5 wt% Si with pure Al, and Al-4.5 wt% Cu.

The compositionally modified A356 was rheocast to allow viscosity measurements at higher fractions solid than permitted by the higher silicon content commercial alloy. The Al-4.5 wt% Cu was rheocast for the same purpose. Figures 3-4 and 3-5 show the fraction solid temperature dependence for the two alloys. There were several stages in producing samples with the MIT method. In the case of the A356, it was first heated in an induction furnace along with pure aluminum pellets. After melting, convection homogenized the melt before it was cast into a cylindrical mold. The material was later reheated and melted in another induction furnace and modified with the insertion of the copper rod. Eight samples could be machined from the rheocast, one kilogram slug. Two different slugs of modified A356 were chemically analyzed, and their compositions were similar and void of gradients along the cross section (Table 3-1).

3.3 Experimental Procedure

The entire experiment can be separated into three major phases: preparation of the furnace and DFV before the furnace is heated to temperature, execution of the experiment after the sample is at the desired fraction solid, and analysis of the downloaded data using a commercial image analysis software package.

3.3.1 Initial Preparation of Furnace and Drop Forge Viscometer

Experiments are conducted at a high temperature between 575 and 640 °C; therefore, the DFV must be properly installed in the furnace before it is heated. The upper platen is coated with graphite and boron nitride and is attached to the rod. The lower platen is placed in the furnace

and aligned using a level. Next, the upper platen rests on the lower platen to indicate the zero height position, and a tape is placed on the rod so that the marker is near the bottom field of view of the camera. An image is captured to serve as the calibration image of the base position. A sample of known height is placed between the plates, and another image is captured. The two images are used to determine the number of millimeters per pixel. Every test begins with a new set of calibration images.

The lower platen is removed, and the upper platen is adjusted to the desired initial height using the solenoid. The plate can fall from a height of 30.5 cm or rest on the sample like a conventional parallel-plate viscometer, thus allowing examination of a wide range of shear rates. The furnace is programmed to heat from ambient to the test temperature over the course of two hours. The furnace soaks at the test temperature for two additional hours before a sample is placed in the furnace. The sample and lower platen are inserted into the furnace using a tong-like device.

It was determined from thermocouple measurements that the sample requires a little more than an hour to reach the desired fraction solid; therefore, samples are placed in the furnace for ninety minutes prior to testing. Figure 3-6 shows a temperature versus time profile for a sample. The temperature was measured in the center of a sample using a type-K thermocouple.

3.3.2 Drop Forge Viscometer Experiment

After the sample has been heated for ninety minutes, the actual DFV test is conducted. The furnace is turned off before compression because the vibration of the furnace interferes with digital imaging. In the time frame of the test, the temperature of the sample is not affected by the loss of power. A switch turns off the solenoid to release the rod. Prior to impact, the photovoltaic sensor triggers the camera. At 18 kHz, the camera can capture 4096 images for approximately 0.22 seconds, while a typical compression test is completed in about 0.01 seconds. After impact, the rod is manually lifted back into the solenoid. The furnace door is opened and the lower platen and sample are removed together from the chamber. Occasionally, the sample will stick to the upper plate, but upon cooling below the eutectic temperature, the sample is firm enough to be removed. Another sample can then be placed into the furnace for another experiment.

Besides the fast compression experiments, the platen can be rested on the sample for slow compression. The force is assumed to be the weight of the upper platen, and the duration of the test is much longer than the fast compression experiments. Experiments have been conducted that last between 15 minutes and 24 hours. The camera acquires images at a rate of 30 Hz for approximately 35 seconds. During an experiment, the camera begins acquisition, and the platen is placed on the sample. After the image capture is complete, the image files are downloaded from the camera to a PC. This procedure of capturing and downloading is repeated, so images are collected in intervals over the duration of the test.

3.3.3 Image Analysis

The image data files are transferred to a laptop PC and then to a Macintosh PC. The commercial image analysis software program IPLab® (registered product of Scanalytics, Inc., Fairfax, VA) is used to measure the displacement of the sample as a function of time. A macro routine was written that performs the task of measuring the displacement because of the large number of images per test. The major steps in the macro routine are listed below.

- Temporally, the marker on the rod moves in the -y direction for a particular value of x. An image is opened from the data series to determine the value of x for that particular experiment. Figure 3-2 shows the marker moving vertically.
- Images are arranged into a sequential file list.
- A loop is started, with several iterative tasks being performed.
- An image is opened, and intensity is normalized to increase the contrast between the light and dark areas of the image. The marker and rod are dark, and therefore intensity in that region is small, usually less than 140, while the back-lit area intensity is over 180.
- Using the known x-value from the test image, the pixel intensity is checked at a value of $(x, y = 0)$. If the intensity is small enough to correspond to the marker, the pixel y-coordinate is written to a data file. Otherwise, the y-value is incremented and the intensity is checked again. This loop repeats until the lower relative intensity of the marker is detected.

- The next image is opened and the process is repeated until every image has been analyzed.

The data (text) file contains two columns. The first contains the image sequence number, and the second is the pixel y-coordinate.

3.4 Calculation of Viscosity and Shear Rate

The data file is utilized to determine apparent viscosity in the commercial graphing program Kaleidagraph^{TM} (registered trademark of Synergy Software). The data is first converted into height and time, and then the first and second derivatives are calculated to determine compression velocity and acceleration. Using this data, along with the Stefan equation (Equation 2.27), apparent viscosity can be calculated.

3.4.1 Displacement Analysis

As mentioned above, the data contain sequential numbers and corresponding pixel values. The sequence is converted into time by dividing the data by the capture rate, 18 kHz. The pixel values are converted to height using a conversion of millimeters per pixel, as determined by the calibration images. The pixel value is multiplied by the conversion factor, thus resulting in a height in millimeters. The minimum height in the data file is compared with the experimental compressed sample height; subsequently, the data file is adjusted to equal the experimental height. For example, if the minimum height in the data file was 0.7 mm larger than the experimental compressed sample height, the height in the text file would be subtracted by 0.7 mm. Finally, a plot of height versus time is generated and Figure 3-7 shows a typical instantaneous, dimensionless height versus time plot from an experiment.

3.4.2 Compression Velocity and Acceleration

It is well known from classical physics that displacement, velocity, and acceleration are related by the following two equations.

$$v_z = \frac{dh}{dt} \tag{3.1}$$

$$a_z = \frac{dv_z}{dt} = \frac{d^2h}{dt^2} \tag{3.2}$$

The displacement data, $h(t)$, is curve fit using a fourth order polynomial. The first and second order derivatives are calculated from this curve fit with respect to time; therefore, the compression velocity and acceleration are known.

The Stefan equation is a function of the height of the sample, as well as the compression velocity, dh/dt, the volume, V, and the applied force on the fluid, F (Equation 2.27).

$$F = \left(\frac{3\mu V^2}{2\pi h^5}\right)\frac{dh}{dt}$$

The applied force is the only remaining variable necessary to calculate viscosity. It is assumed that the deceleration of the plate is caused by the viscous force of the fluid on the falling platen. This deceleration of the rod corresponds to an *acceleration* of the fluid. The applied force is therefore calculated from the deceleration of the platen multiplied by its mass. Including gravity, this is the applied force on the fluid.

$$F = m_{platen}\left(\frac{d^2h}{dt^2} + g\right) \tag{3.3}$$

Figure 3-8 and 3-9 are examples of plots of the first and second derivatives of height with respect to time.

3.4.3 Viscosity and Shear Rate Calculation

Each of the variables are known as a function of time in the Stefan equation, thus viscosity as a function of time can be calculated. This viscosity is an average throughout the volume, and it is an instantaneous calculation. The shear rate can be calculated with Equation 2.30, which is a function of the maximum radial position of the sample, R, the height, h, and the compression velocity, dh/dt.

$$\dot{\gamma} = -\frac{R}{2h^2}\frac{dh}{dt}$$

Since the volume and instantaneous height of the sample are known, the radius is determined assuming continuity. Each variable is known as a function of time, thus shear rate can be

calculated. This calculated shear rate, like the viscosity, is an average throughout the volume and instantaneous with respect to time. When viscosity and shear rate are mentioned in this work, they are referring to the definitions from this section.

3.5 Assumptions and Potential Error in the Calculation of Viscosity and Shear Rate

There were several assumptions to be verified in using the Stefan solution for calculation of viscosity. Wall slip, the effect of the z-component of motion, and inertial effects were analyzed to determine if they had an effect on the viscosity calculation. Potential experimental error will also be discussed in this section.

3.5.1 Wall Slip

The Stefan equation uses the boundary condition that the fluid velocity is zero in the radial direction at the position of the plates ($v_r = 0$ at $z = 0$ and $z = h$). An experiment was conducted to verify that the boundary condition was satisfied in the DFV. A hole was drilled into a sample perpendicular to the radial direction at a distance of one half radius from the center z-axis and was filled with iron powder. After compression in the DFV, the sample was radiographed and the iron appeared to be pinned at the surface of the sample, indicating no wall slip. Visual observation of samples after compression also confirms the no wall slip condition because the outline of the original sample is unchanged. In addition, the surface of the sample outside of the original radius shows radial flow marks from layers of fluid that have flowed from beneath the surface.

3.5.2 Non-Radial Pressure Gradients

Another major assumption of the Stefan equation is the absence of the z-component of the equation of motion in the solution. The classic assumption is that the radial velocity is overwhelmingly larger than the compression velocity, but during an experiment in the DFV, these two velocities can be comparable because of the small aspect ratio of the cylindrical sample (radius:height). After the initial moment of compression, the aspect ratio of the cylindrical

sample determines the ratio of v_r and v_z.because of continuity.

The commercial fluid dynamics software program FLOW-3D® was used to determine whether axial fluid flow was significant. The modeling code and mesh used throughout this work is in Appendix B. Because it is known that pressure gradients drive flow, the relative magnitude of the gradients in the r and z directions were visually compared. Figure 3-10 shows the pressure contours in a sample as it is compressed, and half of the sample is shown in the $r-z$ plane. It is clearly seen that by the third frame, the pressure gradient is primarily in the r-direction, supporting the validity of neglecting the z-component and the use of the Stefan equation. The validity of the radial flow assumption increases as the sample is strained and the aspect ratio increases.

3.5.3 Inertial Effect

Because of the large compression velocities during an experiment, it was thought that inertial effects may significantly contribute to the experimentally determined force. Because the force is used to determine viscosity, an overestimation of force due to inertia could greatly affect the viscosity calculation. FLOW-3D® was used to examine the potential effect of inertia. The inertial component of the equation of motion, Equation 2.17, is dependent on the fluid's density, and when the computer program calculates the force on the fluid, inertia is included in the analysis. The Stefan solution, on the other hand, is independent of density, and therefore is not affected by inertia.

For a given set of conditions, *i.e.* compression velocity and viscosity, the force predicted by the computational fluid dynamics program and the Stefan equation could be compared as a function of density. Figure 3-11 is a plot of force versus density for a 10 Pa·s fluid that is being compressed at 1 m/s. Because the Stefan result is independent of density, it is normalized to one, and the FLOW-3D® force is compared relative to it. The two curves represent the force at different instantaneous heights during an experiment. As density, compression velocity, and $h(t)/h_o$ increase, there is deviation in the force predicted by the two methods. Decreasing the viscosity also increases the deviation. For a fluid with a density of 2500 kg/m^3 and a viscosity of 10 Pa·s (conservative values representative of semi-solid aluminum), the difference in force is less than a factor of 1.5 for the velocities achieved in the DFV. This gives great confidence that

the force determined from experiments is from primarily viscous and not inertial effects. The deviation in force as $h(t)/h_o \rightarrow 1$, coupled with the fact that $v_z \approx v_r$ during the initial moments of compression, gives greater confidence in the viscosity calculation as the test progresses and strain increases.

3.5.4 Experimental Error

Because the shear rate and viscosity calculations have a strong functional dependence on the displacement data, a small amount of error can drastically affect viscosity. One pixel in a digital image corresponds to less than 0.1 mm in sample height. During analysis of a series of images, deviation in displacement data is no more than one or two pixels; therefore, the raw data have a high degree of precision. However, compressed samples occasionally have variation in final cross-sectional thickness of approximately 0.5 mm. A deviation in height of this magnitude would change the calculated shear rate by as much as 50% at shear rates near 1500 s^{-1}, and viscosity would also be affected.

The temperature variation in a sample is approximately ± 0.5 °C, which can lead to changes in fraction solid of a reheated, rheocast sample. The fraction solid dependence on temperature (df_s/dT) is different depending on the alloy and the temperature, but for the fraction solid range studied in this work, df_s/dT was approximately 0.03 and 0.01 for Al-Cu and Al-Si, respectively. The Al-Cu alloy used in this work was a binary alloy of 99.999% purity; thus, it was assumed that cross-sectional variations in copper content were minimal. On the other hand, the commercial Al-Si alloys have compositional gradients that may lead to fluctuations in fraction solid for a given temperature. Because of the furnace temperature and the compositional gradients in this material, the fraction solid can deviate by as much as 0.02.

In most experiments, the initial 20-25% of the displacement data was not employed to calculate viscosity, and the initial 35-45% was eliminated at low fraction solids. A considerable amount of scatter existed in this portion of the experiments, and a few likely reasons have been identified. The most probable cause is the decrease of sample height prior to compression due to slumping of the specimen under its own weight, and this effect increases at lower fraction solid. Additionally, the falling upper platen is not perfectly aligned, and some amount of compression may be required before the entire surface of the platen is impacting metal alloy.

Other possible sources of data scatter are semi-solid structure inhomogeneities and the small amount of deceleration during the initial period of compression.

The major goal in this thesis is to examine order of magnitude changes in fluid behavior; thus, the error discussed in this section should not have a large effect. In the following chapter, potential effect of error is included in an example of viscosity and shear rate results.

Alloy	%Si	%Mg	%Fe	%Mn	%Ti
A357 (*nominal*)	7.0	< 0.60	...	< 0.03	...
A357 SIMA (*left end of billet*)	6.37	0.52	0.10	0.01	0.05
A357 SIMA (*center of billet*)	6.67	0.53	0.11	0.01	0.05
A357 SIMA (*right end of billet*)	6.79	0.54	0.10	0.01	0.05
A357 MHD (*center of slug*)	6.74	0.47	0.13	0.01	0.01
A357 MHD (*outer edge of slug*)	7.47	0.51	0.15	0.01	0.01
A356 (*nominal*)	7.0	< 0.35	...	< 0.35	...
A356 (*prior to modification*)	6.67	0.41	0.10	0.005	0.14
Modified A356 (*center of slug 1*)	4.55	0.22	0.09	...	0.09
Modified A356 (*edge of slug 1*)	4.51	0.23	0.09	...	0.08
Modified A356 (*average of slug 2*)	4.43	0.23	0.10	...	0.10

Table 3.1: Weight percent composition of alloys determined with wet chemical analysis (all compositions contain balance aluminum).

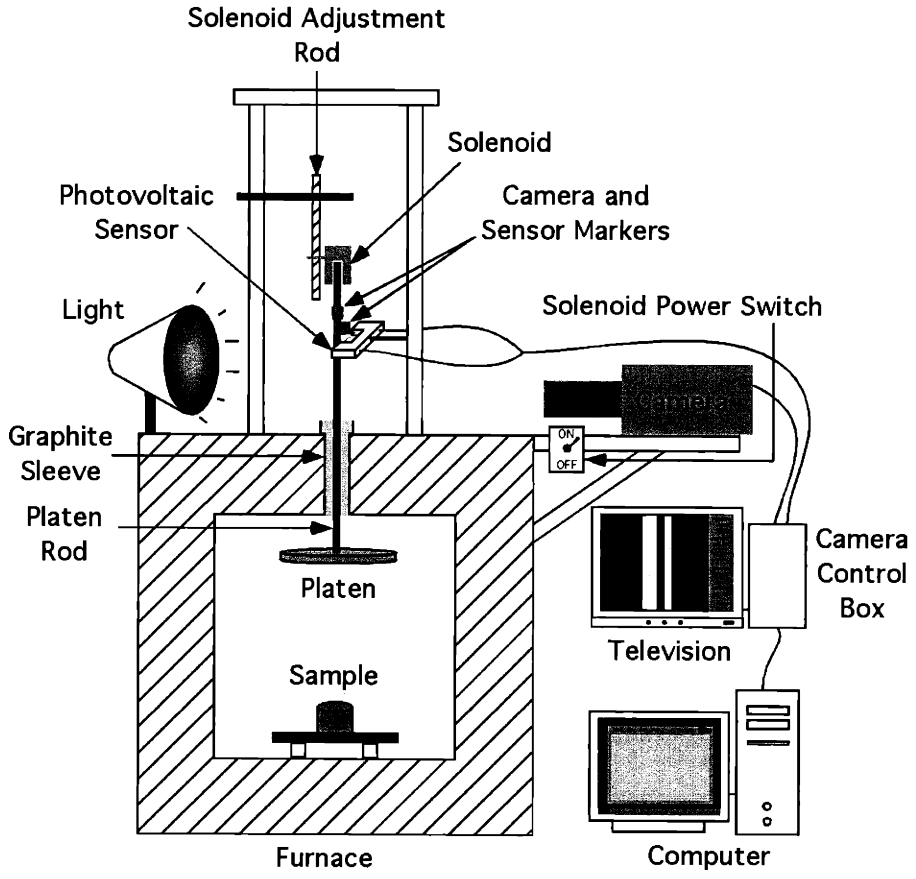

Figure 3-1: Schematic of the Drop Forge Viscometer.

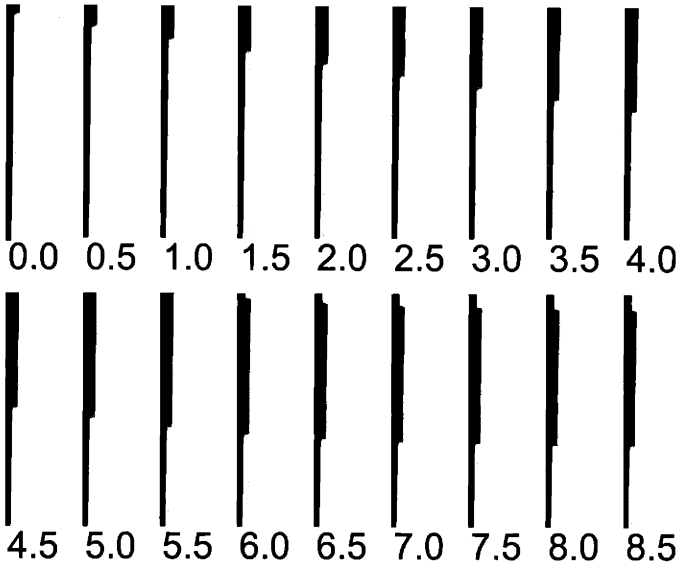

Figure 3-2: Digital images taken from experiment 2 and displayed in 0.5 ms increments (every ninth frame). The thicker portion of the image is a marker on the platen rod that represents the position of the upper platen, and the velocity of the marker is decreasing with each subsequent image.

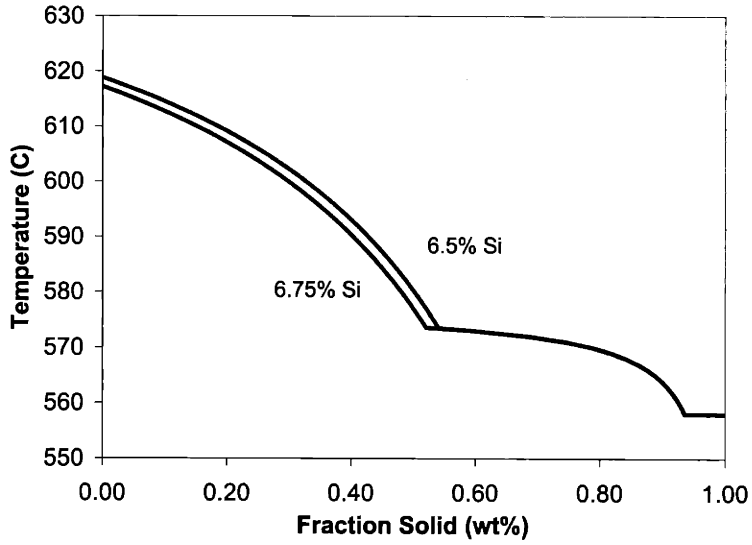

Figure 3-3: Fraction solid (wt%) versus temperature for two A357 alloys with 0.50% Mg, 0.15% Fe, and varying Si content, calculated with Thermo-Calc® and the SGTE thermodynamic database [89]. Details of the fraction solid calculation are in Appendix A.

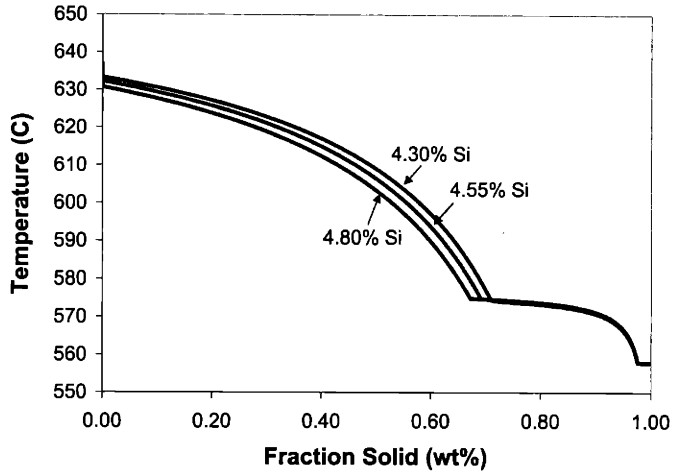

Figure 3-4: Fraction solid (wt%) versus temperature for a modified A356 alloy at varying Si content calculated with Thermo-Calc® and the SGTE thermodynamic database [89]. Details of the fraction solid calculation are in Appendix A.

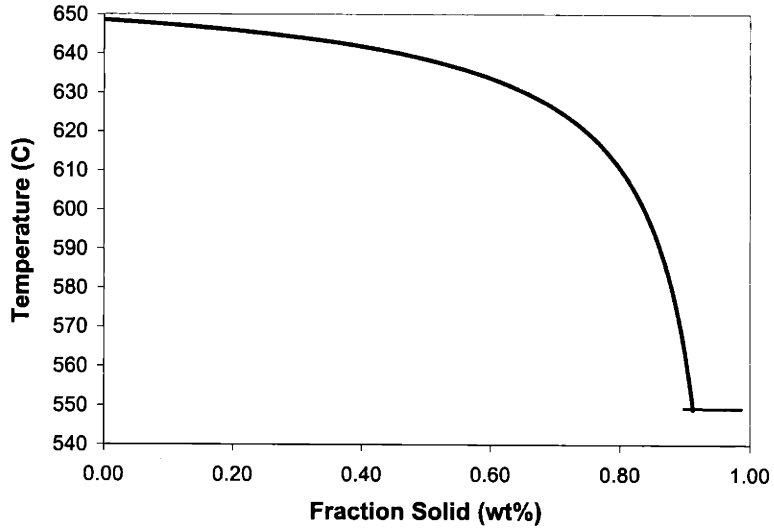

Figure 3-5: Fraction solid (wt%) versus temperature for Al-4.5wt%Cu calculated with Thermo-Calc® and the SGTE thermodynamic database [89]. Details of the fraction solid calculation are in Appendix A.

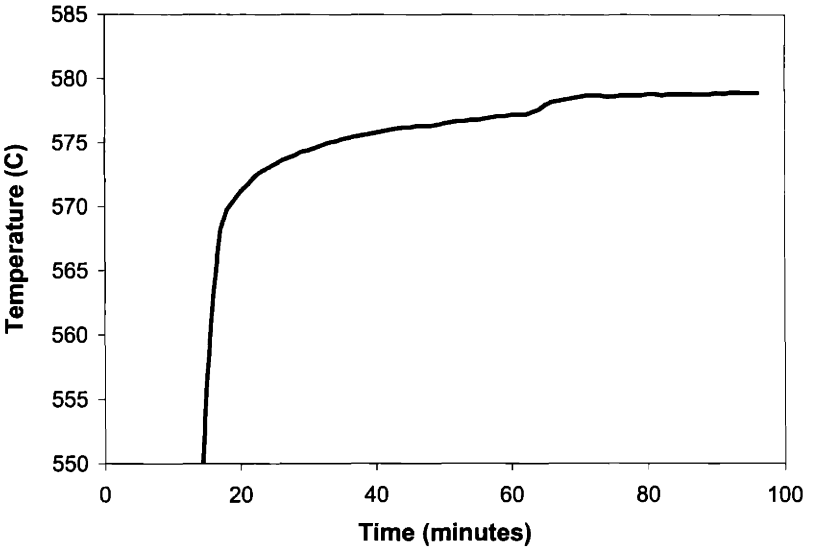

Figure 3-6: Temperature as a function of time for a sample heated to 579 °C in the furnace prior to a compression test.

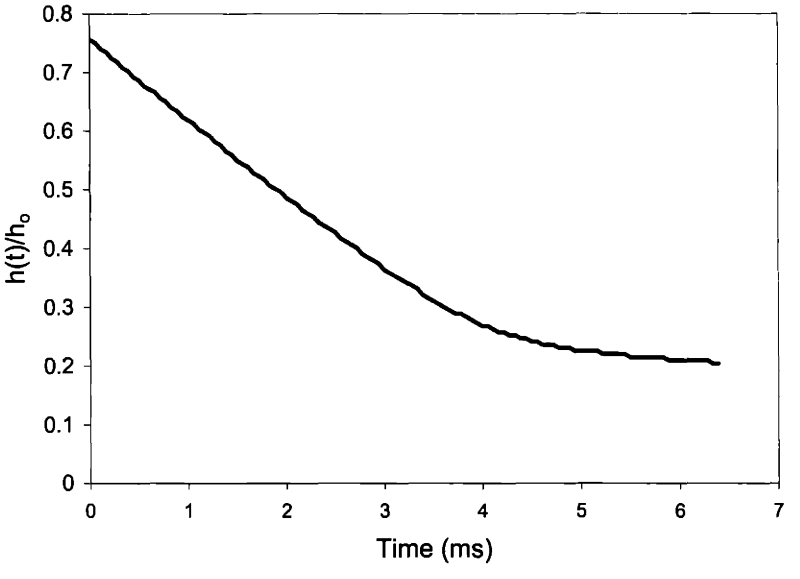

Figure 3-7: Instantaneous, dimensionless height versus time for experiment 2. Displacement was calculated from analyzing a series of images acquired with the Drop Forge Viscometer.

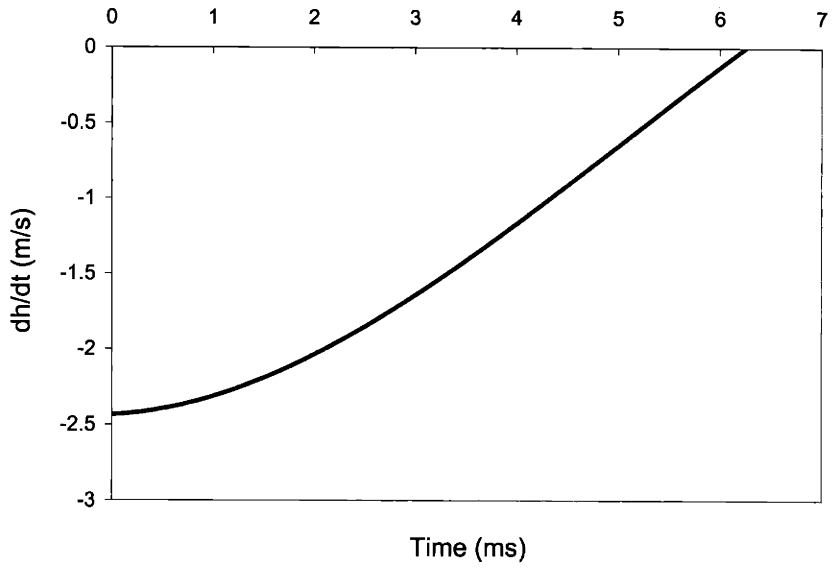

Figure 3-8: The instantaneous compression velocity as a function of time for experiment 2. Velocity is the first derivative of the displacement data (Figure 3-7) with respect to time.

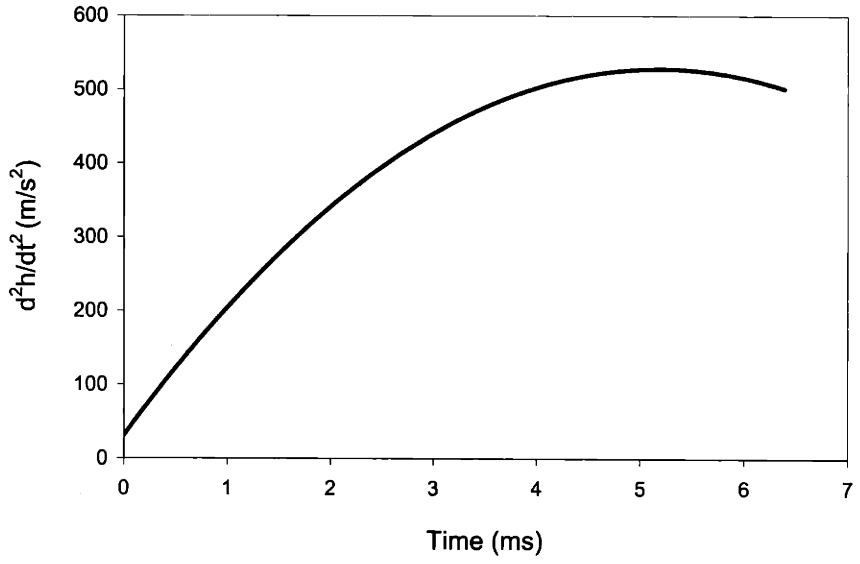

Figure 3-9: Acceleration of the sample during compression for experiment 2. Acceleration is the second derivative of the displacement data (Figure 3-7) with respect to time.

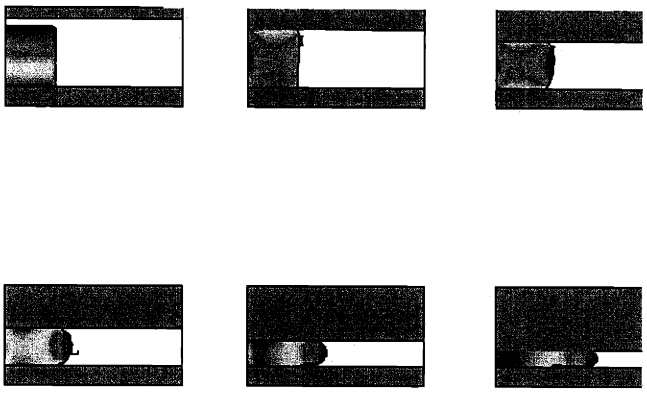

Figure 3-10: Modeling results from FLOW3D® of the pressure contours in a cylindrical sample during compression. Half of the sample is in view in the r-z plane. A Newtonian fluid model was used with a viscosity of 10 Pa·s and a compression rate of 1 m/s. The modeling code is in Appendix B.

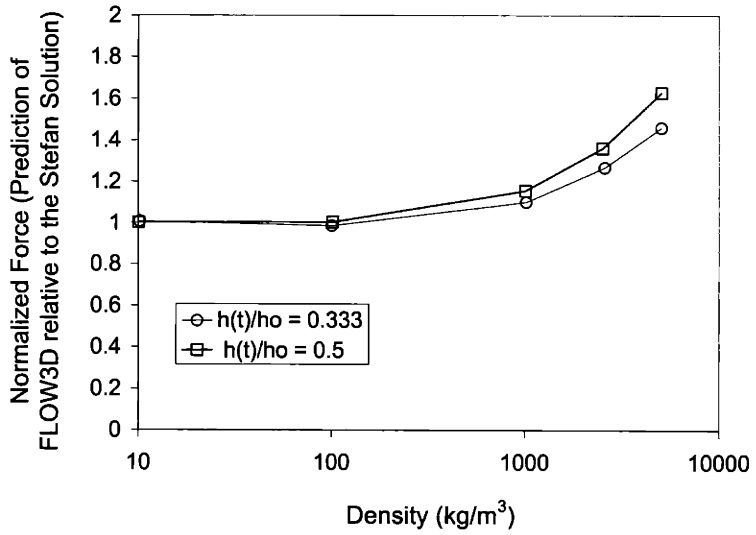

Figure 3-11: Normalized force as a function of fluid density. The FLOW-3D® predicted force is compared with the Stefan solution for a fluid with a viscosity of 10 Pa·s that is compressed at 1 m/s. The density of semi-solid aluminum is approximately 2500 kg/m^3. The modeling code used in this iterative study is in Appendix B.

Chapter 4

Results of the Drop Forge Viscometer Experiments

Results from numerous experiments on the reheated rheocast alloys will be discussed in this chapter. Data and observations from high and low shear rate experiments will be shown, followed by metallography and EDS characterization from select samples. Discussion of the results will follow in the next chapter.

4.1 High Shear Rate Results

Experiments were conducted at high shear rates ($> 10^2$ s^{-1}) on the aluminum-silicon and aluminum-copper alloys described in the previous chapter. In addition to alloy type, three primary variables could be controlled during an experiment: fraction solid of the alloy, initial platen height, and platen (including rod) mass. The volume fraction solid, g_s, which is a function of temperature, was varied between 0.44 and 0.67 depending on the alloy. The initial platen height was set at the maximum position in the furnace, 30.5 cm above the reheated sample, which corresponds to a compression velocity of approximately 2.4 m/s. When mass was added to the apparatus, the initial platen height was lowered with respect to the furnace ceiling to accommodate the mass, consequently decreasing the impact velocity. The mass of the platen system ranged from 0.272 to 1.793 kg. A complete list of experiments is found in Table 4-1.

The viscosity and shear rate were calculated using the method discussed in the previous chapter. The terms viscosity and shear rate refer to an instantaneous, volume-averaged value. Figure 4-1 is a plot of viscosity and shear rate as a function of time from a typical experiment (experiment 2). Shear rate increases during the initial part of the test and flattens out before decreasing. Viscosity, which is dependent on shear rate, decreases during the first part of the experiment and then later increases. Error bars are included that take into account fraction solid and displacement variations of ± 0.02 and ± 0.5 mm. Figure 4-2 is the data from Figure 4-1 replotted as viscosity versus shear rate. Viscosity behaves inversely with shear rate, thus indicating shear thinning behavior of decreasing viscosity with increasing shear rate. The viscosity continues to decrease although the shear rate remains constant, characteristic of thixotropic flow. Finally, the viscosity increases as the shear rate begins to decrease. The absolute change in viscosity is greatest when shear rate is increasing. An interesting observation is that the entire experiment is completed in less than one hundredth of a second (10 ms). Viscosity results will be shown in the following sections for the various alloys.

4.1.1 A357

Most experiments on A357 were conducted using samples produced by the SIMA process. Tests were conducted in a limited fraction solid range, near 0.50. Above 0.50-0.55 g_s, the eutectic constituents of this alloy freeze over a narrow temperature range, thus making precise viscosity measurements impossible. Figure 4-3 and 4-4 are plots of viscosity versus increasing and decreasing shear rates, respectively, for two samples with similar fractions solid (experiments 1 and 2). The entire viscosity versus shear rate curve from Figures 4-3 and 4-4 are plotted together in Figure 4-5. Viscosity versus increasing and decreasing shear rate is represented in Figure 4-2 as regions (a) and (b). The 0.47 and 0.48 g_s samples were compressed with masses of 0.322 kg and 0.379 kg, respectively. In Figure 4-3, the viscosities are similar, but the higher fraction solid sample does not achieve as large of a shear rate. This effect becomes important when shear rate begins to decrease because the maximum shear rate attained in Figure 4-3 translate to the initial decreasing shear rates of Figure 4-4. The fraction solid of the two samples are statistically insignificant, but the minimum viscosity of the lower fraction solid specimen was an order of magnitude smaller than the other because of its larger maximum shear

rate. Viscosity begins to recover from a smaller value in the lower fraction solid experiment; therefore, the difference in viscosity between samples is much larger in Figure 4-4, than Figure 4-3. The observed differences in viscosity between the two experiments can be clearly seen in Figure 4-5, which is a plot of viscosity as a function of both increasing and decreasing shear rate.

In addition to examining material produced from the SIMA process, A357 MHD (experiments 7 and 8) and A356 MIT material (experiments 9 and 10) were compressed at similar fractions solid. They have essentially the same alloy composition but were produced from three different rheocasting techniques. Figures 4-6 and 4-7 are plots that compare the flow behavior of the three materials. The platen mass used in each experiment was similar, between 0.272 and 0.379 kg. From Figure 4-6, it is apparent that the MHD sample compressed the least, but during the initial part of the test, all of the displacement curves are similar. Deviation in behavior does not become apparent until the samples have compressed to less than seventy percent of their original height. In Figure 4-7, the fluid behavior for the three different materials appears similar, with the exception of the maximum shear rate achieved by the A357 MHD. In spite of the fact the MHD sample was compressed with the heaviest mass (0.379 kg), it exhibited the lowest maximum shear rate ($< 300\ s^{-1}$), while samples produced by the other methods achieved shear rates in excess of $750\ s^{-1}$.

4.1.2 Modified A356

A356 was diluted with pure Al to produce an alloy with a Si content of approximately 4.5wt%. The amount of eutectic is much less than that of conventional A356 and does not begin freezing until the fraction solid is near 0.70. Samples were studied under a wide range of volume fraction solid, between 0.44 and 0.67. Figures 4-8 and 4-9 are plots of the instantaneous, dimensionless height of the sample as a function of time for varying solid fraction. The higher and lower solid fractions were compressed with masses of 1.793 and 0.379 kg, respectively. Figure 4-10 is a macroscopic photograph of the samples after compression in the Drop Forge Viscometer (experiments 11, 12, and 15-18). Figure 4-11 compares the viscosity as a function of decreasing shear rate for four different fractions solid (experiments 12, 14-16, and 18). Viscosity increases with fraction solid, as expected for suspensions of increasing volume fraction solid.

Figure 4-12 compares the viscosity of the modified A356 MIT with A357 SIMA (experiments 1, 2, and 12). The viscosities are very similar for the two different Al-Si alloys produced from different rheocast techniques at the same fraction solid. These results are not only encouraging that Al-Si alloys with smaller amounts of Si may be used at higher fractions solid during forming operations, but also that the MIT technique is a viable method for producing rheocast material.

4.1.3 Al-4.5wt%Cu

A binary Al-4.5wt%Cu alloy was also examined with the DFV. This alloy has a small amount of eutectic, thus allowing for higher fraction solid experiments. Figure 4-13 is a plot of the instantaneous, dimensionless height as a function of time during compression for varying fraction solid and platen masses (experiments 19-21 and 24). Figure 4-14 is a plot of the viscosity as a function of shear rate for three different fractions solid (experiments 19, 21, 22, and 24). The observed flow behavior, shear thinning, agrees with the results of the aluminum-silicon alloys, but the aluminum-copper alloy requires a larger platen mass to achieve the same shear rates.

4.1.4 Comparison of Al-Si and Al-Cu

Figures 4-15, 4-16, and 4-17 are plots that compare the viscosity behavior of the aluminum-copper and the modified A356 alloys at two different fraction solid values (experiments 12, 15, 19, and 24). The viscosity of the Al-Cu alloy at a fraction solid of 0.46 was greater than the viscosity of the modified A356 at similar fraction solid, and the Al-Si alloy achieved a higher maximum shear rate even though it was compressed with a mass that was two and a half times less than the mass used to compress the Al-Cu alloy (Figures 4-15 and 4-16). In the higher fraction solid comparison, the two alloys exhibit the same viscosity curve, but the modified A356 achieves a larger maximum shear rate. Figure 4-18 is a plot of the instantaneous, dimensionless height as a function of time for the two alloys. The Al-Si compressed to a smaller height for a given fraction solid and platen mass. The differences in the viscosities of the alloys will be discussed in the next chapter.

4.2 Low Shear Rate Results

Experiments were conducted at low shear rates (10^{-5} to 10^{-2} s^{-1}) with the DFV on reheated A357 SIMA, resting the upper platen on the reheated sample and assuming the force on the sample was the weight of the platen. The tests complement the high shear rate experiments, and the technique is that of Laxmanan and Flemings from the original parallel-plate compression study on tin-lead semi-solid alloys [36]. Figure 4-19 is a plot of the viscosity as a function of decreasing shear rate for three experiments at a fraction solid of 0.48 (experiments 4-6). The fluid behavior is shear thinning, similar to the high shear rate results. The gap between shear rates from the high and low shear rate experimental techniques is almost 4 orders of magnitude; therefore intermediate tests were conducted with the platen being dropped from an initial height of less than 1 inch. In this configuration, attained shear rates were on the order of 1 to 50 s^{-1}, which are slightly smaller than that of the high shear rate tests (experiment 3).

The viscosity results from the three different experimental methods are shown in Figure 4-20 (experiments 1-6). The high shear-rate results are taken from the decreasing shear rate portions of each test. The results agree quite well over several orders of magnitude of both shear rate and viscosity.

4.3 Metallography

Micrographs of the various alloys were obtained both prior to compression, and in the case of the A357 SIMA, after compression. Quantitative metallography was performed and tabulated for each micrograph.

The shape factor, F_o, a value that relatively compares the area of a grain, A, and its perimeter, P, was calculated for each micrograph.

$$F_o = \frac{4\pi A}{P^2} \tag{4.1}$$

The shape factor ranges between 1 and 0, with 1 and 0 corresponding to a circle and line, respectively. The shape factor was determined for each grain in a micrograph and averaged. The number of grains were recorded per micrograph, which had an area of 1.8 mm^2.

Images were acquired with a Spot Diagonostic Instruments digital video camera attached to an Olympus Vanox-T optical microscope. Samples were polished to 0.05 μm and observed in the unetched condition. The image analysis program IPLab® was employed to perform quantitative metallography.

4.3.1 Uncompressed Material

The micrographs of the uncompressed, quenched specimens can be seen in Figure 4-21. Fraction solid was predicted with Thermo-Calc®, and the calculation is described in Appendix A. Shape factor and number of grains per mm^2 are tabulated in Table 4-2. The shape factor of the MHD sample is the smallest and has the largest amount of scatter, as seen in Figure 4-21(c), and this material appears from visual observation to have the largest amount of entrapped liquid within the primary grains. The SIMA produced material has some entrapped liquid, while the MIT alloys have very little. The grain size of the MIT material is larger than the two commercial techniques, but this is due to the fact that the material was not processed under optimal conditions.

The material that was liquid prior to quenching in the Al-4.5wt%Cu did not appear visually as evenly dispersed as in the Al-Si alloys. In Figure 4-22, a large pocket of eutectic phase is evident, which is not seen in the Al-Si material after quenching.

4.3.2 Compressed A357 SIMA

Micrographs of A357 SIMA were taken after three different compression tests (Experiments 2, 5 and 6), as seen in Figures 4-23, 4-24, and 4-25, and the corresponding quantitative results are in Table 4-3.

In Figure 4-23, micrographs are shown for a sample that has been compressed at high shear rates. Images were taken at (a) the outer edge and (b) in the center of the sample. The shape factor is not only similar for both regions, but it is also the same as the as-cast quenched SIMA material (Table 4-2). Particle size differences are minimal and segregation is not apparent.

Two slow compression experiments were performed for various durations of time. In experiment 5, the sample was compressed for 16 minutes. Figure 4-24 presents micrographs of (a) the outer edge and (b) the center of the sample. The shape factors are again similar, but

the number of particles is less at the outer edge relative to the middle. The size of particles appears to be the same through out the specimen, but the overall number of particles is smaller than the fast compression experiment as a result of coarsening.

The last set of micrographs, Figure 4-25, are from a four-hour slow compression test (experiment 6). Three micrographs are shown in the figure, including (a) the edge and (c) the middle of the sample. Segregation is apparent at the outer edge, where the composition is near the eutectic. The middle of the sample consists of mainly primary aluminum grains, and a transition between this phase and the eutectic exists and is clearly seen in (b). Again, the number of particles is relatively small because of coarsening.

Besides optical microscopy, energy dispersive spectroscopy (EDS) was performed on the three compressed A357 samples. EDS (a.k.a. EDX) determines the chemical composition of the sample surface by measuring characteristic X-rays emitted from the specimen. The EDS detector rests inside of an SEM close to the surface of the sample. The major limitation with EDS is that an element must consist of at least a few weight percent for an accurate composition reading. However, this precision is adequate for the comparison of silicon content in different regions of the compressed samples. Measuring silicon content allows for determination of the local fraction solid using the lever rule in the specified region of the sample.

Data acquired with EDS is given in Table 4-4. The scanning electron microscope was set at a magnification of 50X so that a diffuse area was collected by the instrument detector. Several measurements were made for each sample at the radial edge and center of the samples.

Volume fraction solid was calculated by two methods and is also listed in Table 4-4. The area of the particles in each micrograph was measured with IPLab® and divided by the total area of the picture. This is not the ideal technique for measuring fraction solid, but it is useful for comparing relative fraction solid among samples. Fraction solid was also calculated by using the EDS silicon composition data in combination with the binary Al-Si phase diagram and the lever rule. Both techniques have significant amounts of error, but they are adequate for detecting macrosegregation.

Exp. #	Alloy	Temp. (°C)	Vol. Fraction Solid	Platen Mass (kg)	Max. Shear Rate (s^{-1})	Final Sample Height (h_f/h_o)
1	A357 SIMA	580	0.47	0.322	1330	0.15
2	A357 SIMA	579	0.48	0.379	750	0.19
3	A357 SIMA	579	0.48	0.379	31	0.48
4	A357 SIMA	579	0.48	0.379	0.0027	0.54
5	A357 SIMA	579	0.48	0.379	0.0052	0.52
6	A357 SIMA	579	0.48	0.379	0.0043	0.33
7	A357 MHD	579	0.48	0.379	295	0.28
8	A357 MHD	579	0.48	0.379	280	0.27
9	A356 MIT	580	0.47	0.272	1270	0.21
10	A356 MIT	580	0.47	0.272	1500	0.20
11	Mod. A356 MIT	611	0.44	0.379	N/A	0.03
12	Mod. A356 MIT	607	0.48	0.379	965	0.20
13	Mod. A356 MIT	600	0.55	0.379	85	0.56
14	Mod. A356 MIT	600	0.55	0.379	115	0.51
15	Mod. A356 MIT	599	0.56	1.793	900	0.25
16	Mod. A356 MIT	594	0.60	1.793	375	0.31
17	Mod. A356 MIT	589	0.62	1.793	N/A	0.44
18	Mod. A356 MIT	579	0.67	1.793	60	0.59
19	Al-4.5wt%Cu MIT	640	0.46	0.917	770	0.18
20	Al-4.5wt%Cu MIT	638	0.51	0.917	175	0.33
21	Al-4.5wt%Cu MIT	638	0.51	1.736	550	0.27
22	Al-4.5wt%Cu MIT	638	0.51	1.736	410	0.29
23	Al-4.5wt%Cu MIT	636	0.56	0.917	215	0.37
24	Al-4.5wt%Cu MIT	636	0.56	1.736	285	0.31

Table 4.1: Master list of experiments conducted in this thesis.

Material	Calculated Vol. Fraction Solid (g_s)	Shape Factor (F_o)	# of Grains (per mm^2)
A357 SIMA	0.45±0.02	0.81±0.05	50
A357 MHD	0.45±0.02	0.71±0.13	71
Mod. A356 MIT	0.42±0.02	0.78±0.06	35
Al-4.5wt%Cu MIT	0.48±0.04	0.76±0.07	28

Table 4.2: Quantitative metallography results of four alloys prior to compression.

Exp. #	Fig. #	Location of Micrograph	Shape Factor (F_o)	# of Grains (per mm^2)	Duration of Experiment
2	4-23a	outer edge	0.80±0.05	54	10 ms
2	4-23b	center	0.83±0.04	48	10 ms
5	4-24a	outer edge	0.82±0.05	33	16 min.
5	4-24b	center	0.81±0.06	48	16 min.
6	4-25a	outer edge	0.61±0.21	N/A	4 hours
6	4-25c	center	0.82±0.04	25	4 hours

Table 4.3: Quantitative metallography results of compressed A357 SIMA.

Exp. #	Duration of Experiment	Region	Si Content (wt% from EDS)	Vol. Fraction Solid	
				optical	EDS
2	10 ms	radial edge	7.15±0.5	0.71	0.46±0.05
2	10 ms	center	6.26±0.5	0.76	0.54±0.05
5	16 min.	radial edge	8.48±0.5	0.47	0.34±0.05
5	16 min.	center	6.43±0.5	0.72	0.53±0.05
6	4 hours	radial edge	11.95±0.5	0.25	0.02±0.05
6	4 hours	center	4.71±0.5	0.78	0.69±0.05

Table 4.4: Comparison of fraction solid of the three A357 SIMA alloys compressed for different durations and shear rates. Fraction solid was determined optically (area fraction method) and using the lever rule with EDS data. Both techniques have significant variation, but there is clearly increased segregation for the low shear rate tests with increasing duration.

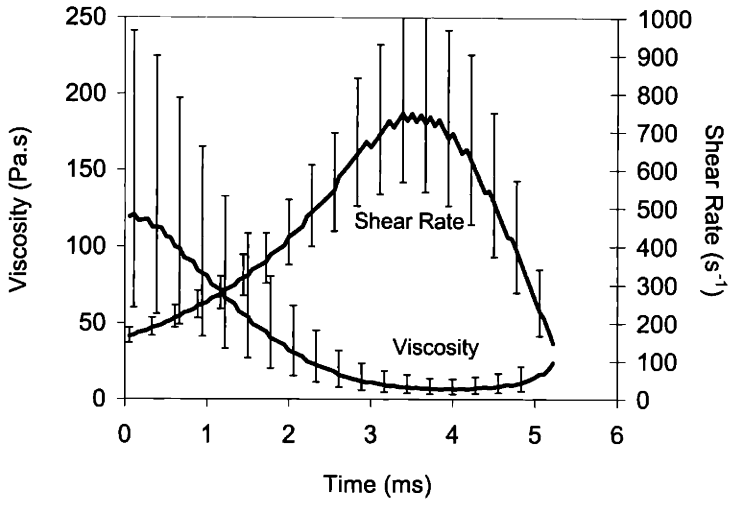

Figure 4-1: Instantaneous, volume-averaged viscosity and shear rate as a function of time for experiment 2. Data from Figures 3-7, 3-8, and 3-9 were used in the calculations. Error bars indicate a range of possible values that result when fraction solid and displacement varies within ± 0.02 and ± 0.5 mm, respectively.

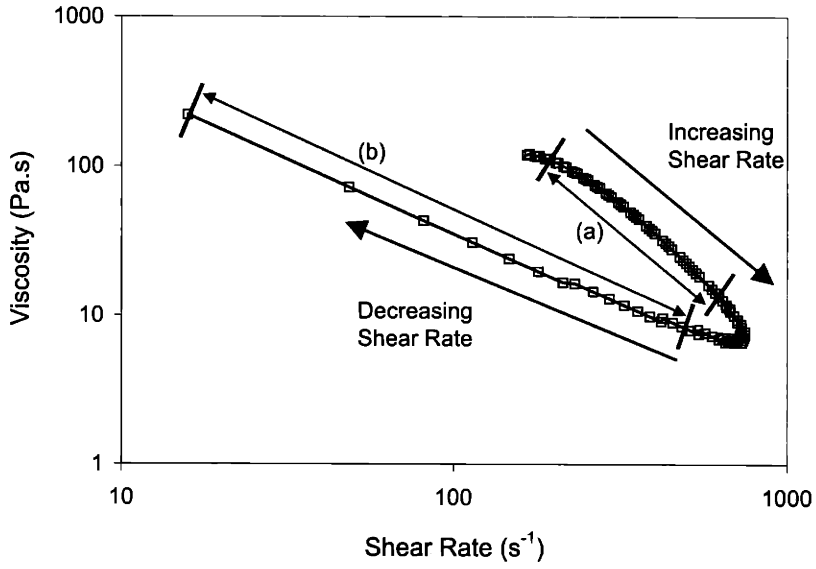

Figure 4-2: Data from Figure 4-1 replotted as viscosity as a function of shear rate. The rate of change of viscosity is greater during the increase in shear rate (experiment 2).

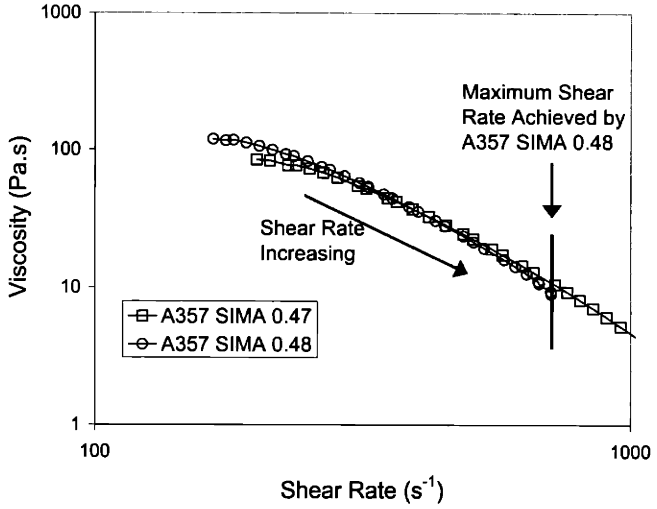

Figure 4-3: Viscosity as a function of increasing shear rate for A357 SIMA at two similar fractions solid (experiments 1 and 2). Data taken from increasing shear rate portion of viscosity versus shear rate curve, *e.g.* region (a) of Figure 4-2. The 0.48 sample did not achieve as large a shear rate for the same initial experimental conditions.

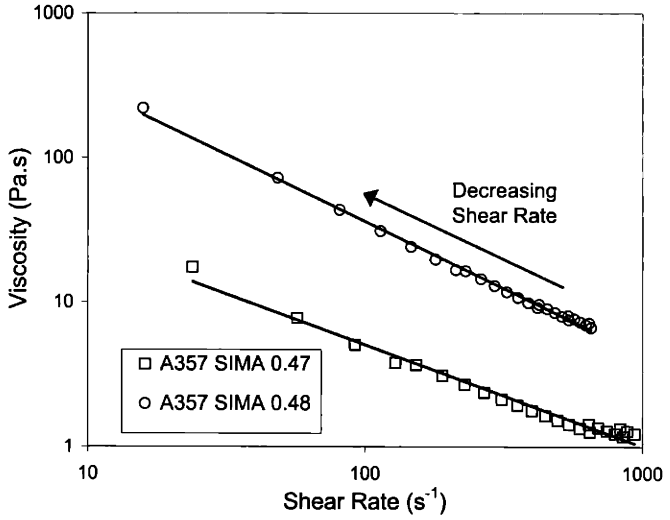

Figure 4-4: Viscosity as a function of decreasing shear rate for A357 at two similar fractions solid (experiments 1 and 2). Data taken from decreasing shear rate portion of viscosity versus shear rate curve, *e.g.* region (b) of Figure 4-2. The higher fraction solid experiment did not achieve as high a shear rate (Figure 4-3), and therefore has a larger viscosity for a given shear rate during the decrease portion of the test.

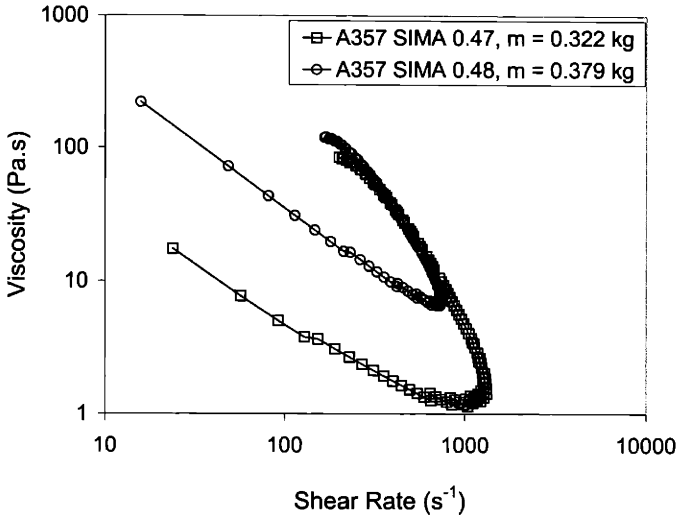

Figure 4-5: Viscosity as a function of shear rate from Figures 4-3 and 4-4 for A357 SIMA (experiments 1 and 2).

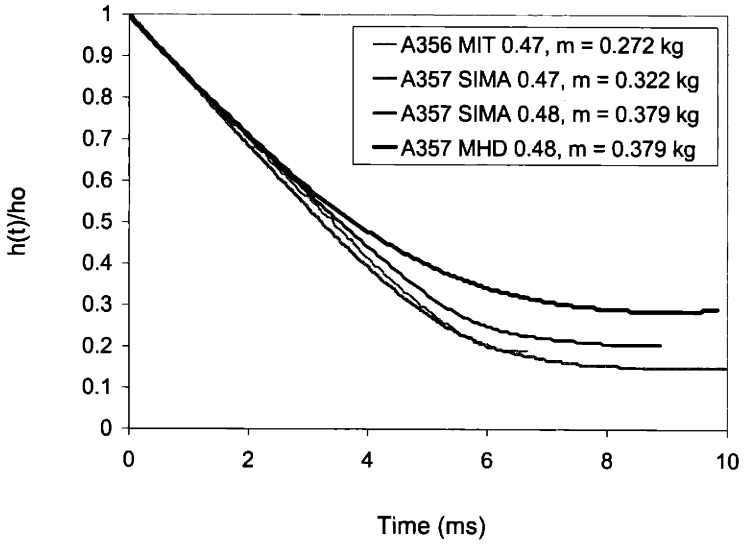

Figure 4-6: Comparison of the instantaneous, dimensionless height of A357 and A356 rheocast with the SIMA, MIT, and MHD processes (experiments 1, 2, 7, and 9).

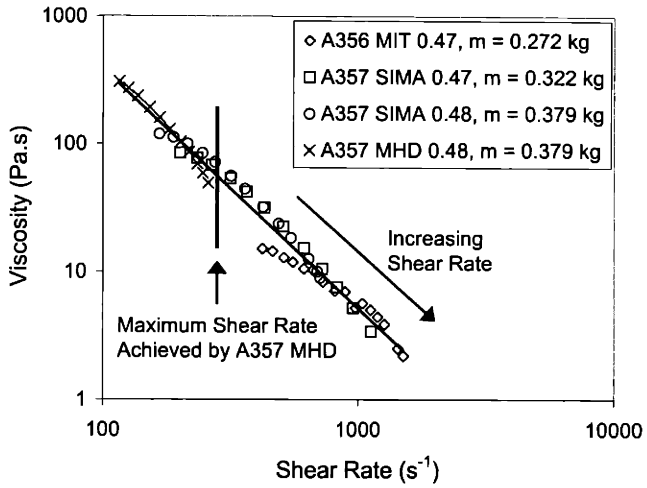

Figure 4-7: Calculated viscosity versus increasing shear rate for A356 and A357 produced by SIMA (experiments 1 and 2), MHD (experiments 7 and 8), and the MIT process routes (experiments 9 and 10). Viscosities are similar, but the maximum shear rate achieved by the MHD was lower than the other materials.

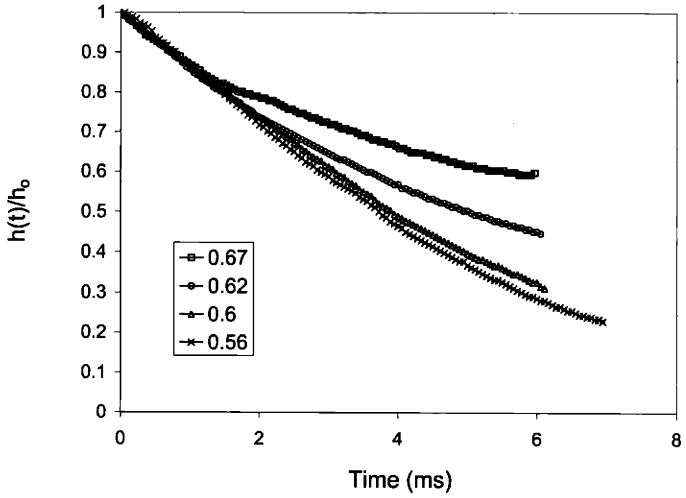

Figure 4-8: Dimensionless height of modified A356 samples compressed in the DFV at varying fraction solid with a platen mass of 1.793 kg (experiments 15-18).

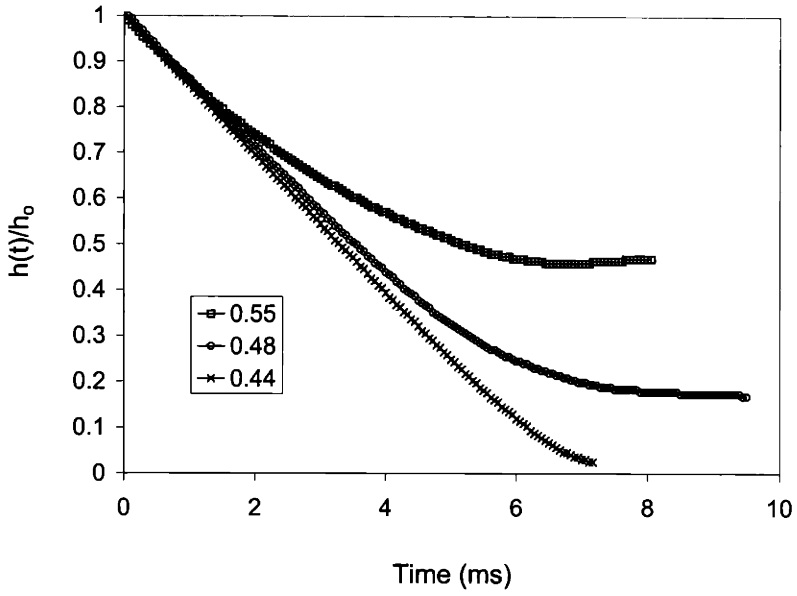

Figure 4-9: Dimensionless height of modified A356 compressed in the DFV at varying volume fraction solid with a platen mass of 0.379 kg (experiments 11-13).

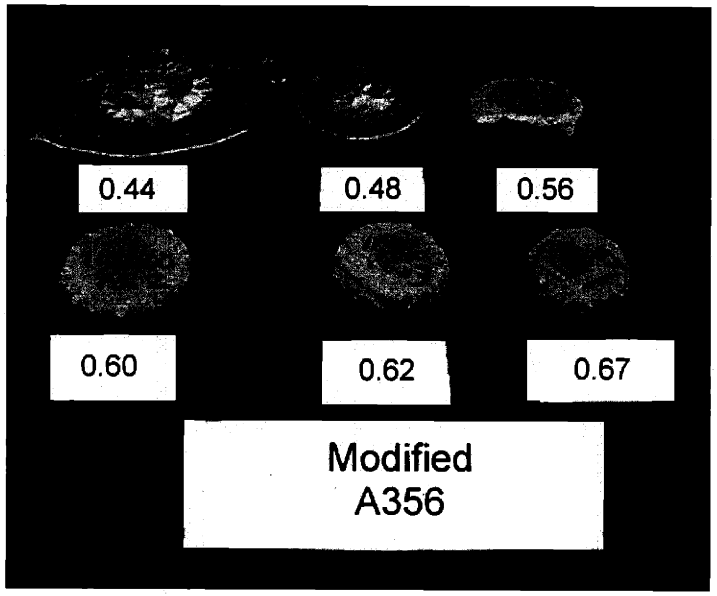

Figure 4-10: Photograph of modified A356 after compression in the DFV for varying fraction solid. The 0.44 and 0.48 and the 0.55, 0.60, 0.62, and 0.67 fraction solid samples were compressed with 0.379 kg and 1.793 kg masses, respectively (experiments 11, 12, and 15-18).

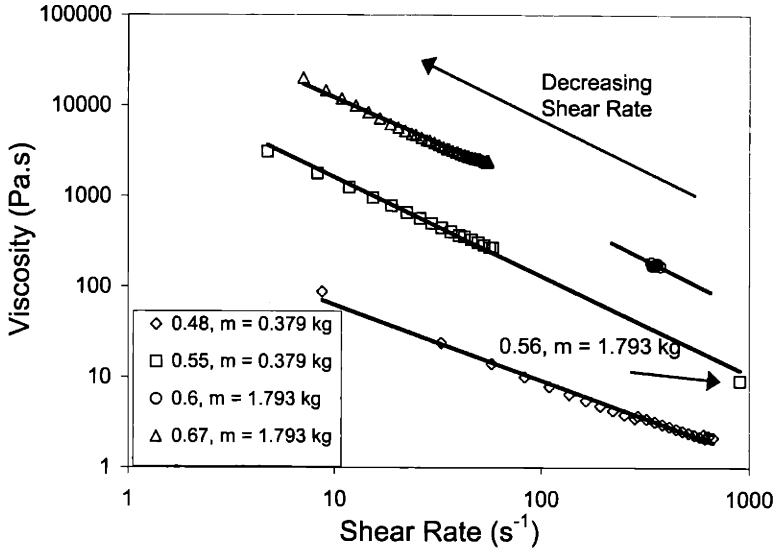

Figure 4-11: Calculated viscosity versus increasing shear rate of modified A356 rheocast with the MIT process. Viscosity can be seen to increase with fraction solid (experiments 12, 14-16, and 18).

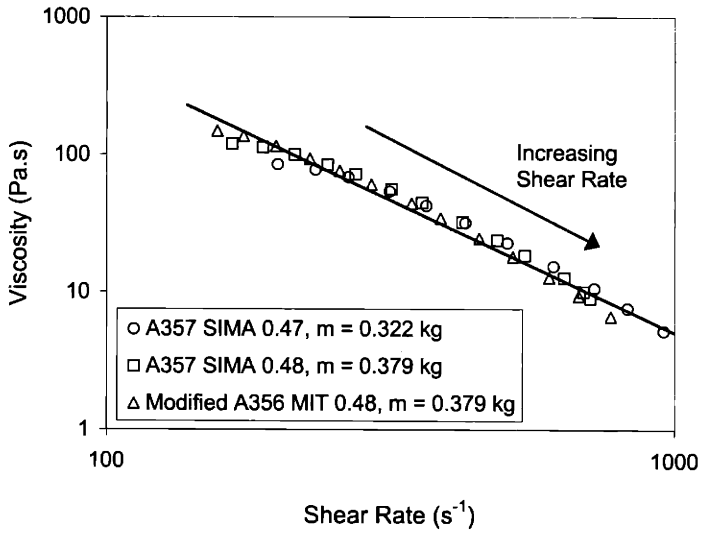

Figure 4-12: Calculated viscosity as a function of increasing shear rate of modified A356 produced by the MIT method compared to conventional A357 SIMA (experiments 1, 2, and 12).

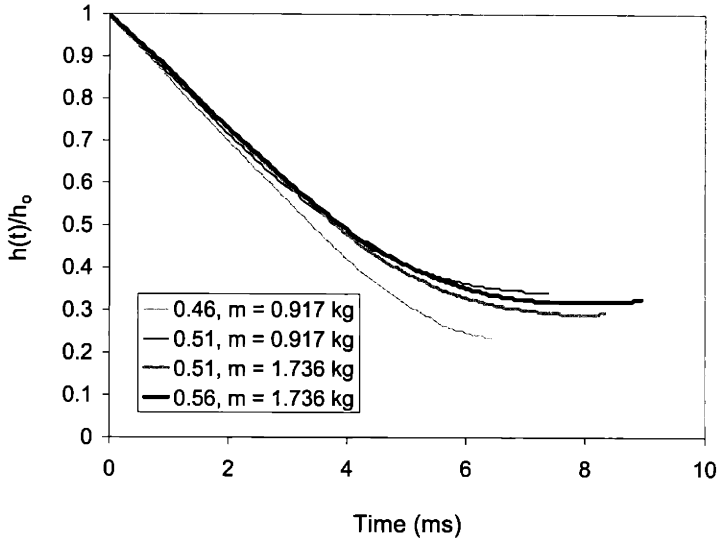

Figure 4-13: Comparison of the dimensionless height as a function of time for rheocast Al-4.5wt%Cu at varying fractions solid and platen masses (experiments 19-21, and 24).

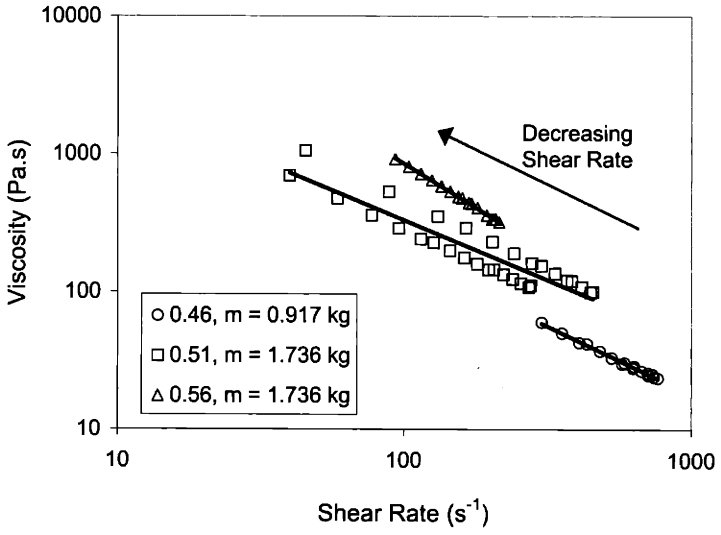

Figure 4-14: Calculated viscosity as a function of decreasing shear rate for Al-4.5wt%Cu at varying volume fractions solid (experiments 19, 21, 22, and 24).

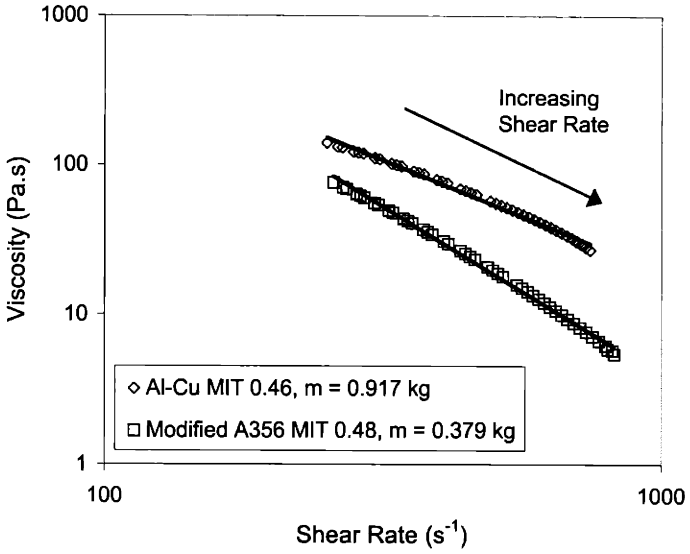

Figure 4-15: Comparison of the calculated viscosity versus increasing shear rate for Al-4.5wt%Cu and modified A356 rheocast with the MIT process at similar fraction solid (experiments 12 and 19).

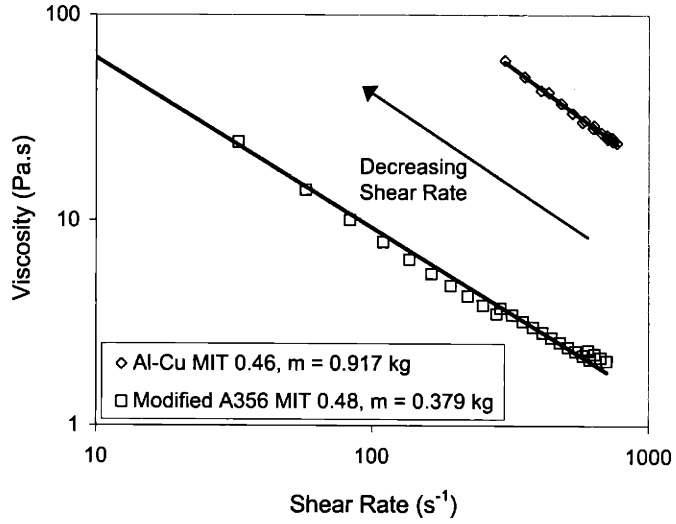

Figure 4-16: Comparison of calculated viscosity versus decreasing shear rate for Al-4.5wt%Cu and modified A356 rheocast with the MIT process at similar fraction solid. The higher viscosity of the Al-4.5wt%Cu corresponds with the higher viscosity observed in Figure 4-15 during the increase in shear rate (experiments 12 and 19).

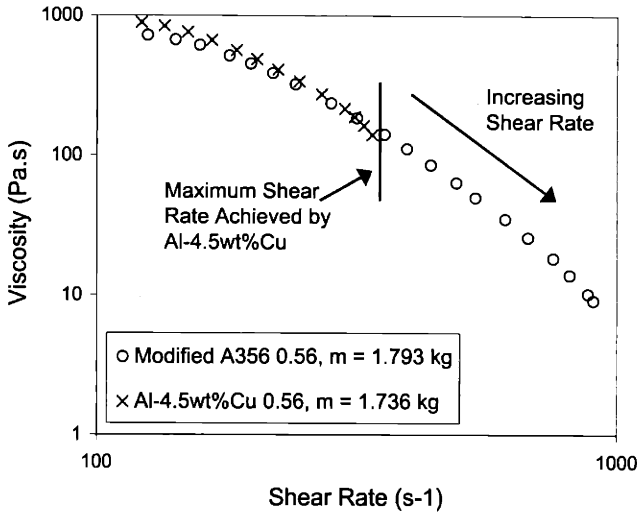

Figure 4-17: Calculated viscosity as a function of increasing shear rate for Al-4.5wt%Cu and modified A356 rheocast with the MIT process (experiments 15 and 24).

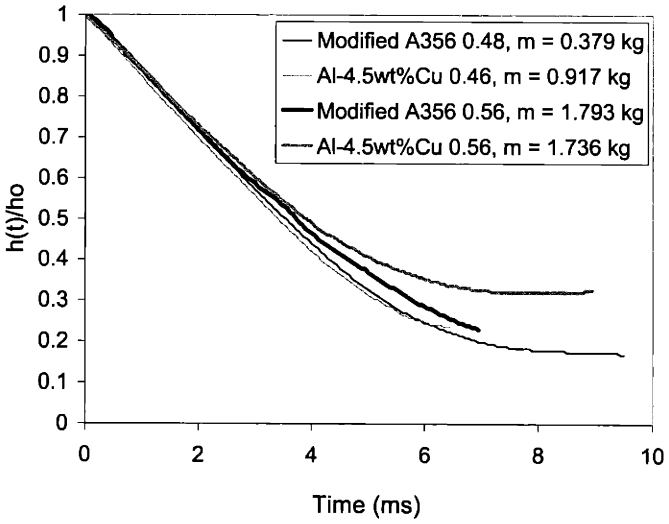

Figure 4-18: Comparison of the dimensionless height for rheocast Al-4.5wt%Cu and modified A356 at varying fractions solid and platen masses (experiments 12, 15, 19, and 24).

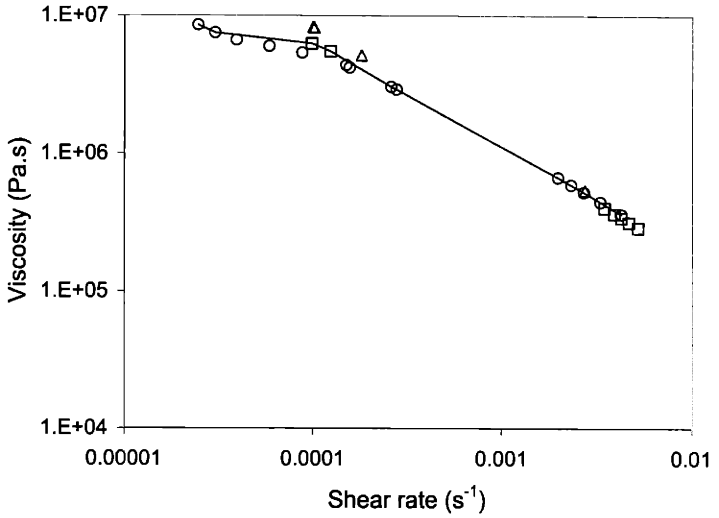

Figure 4-19: Calculated viscosity as a function of decreasing shear rate for A357 SIMA at low compression velocity. Data are from three experiments carried out at a volume fraction solid of 0.48 (experiments 4-6).

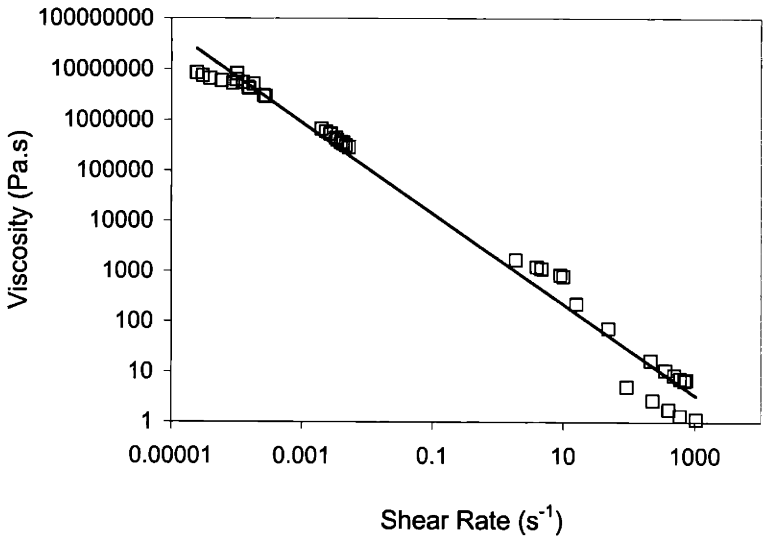

Figure 4-20: Calculated viscosity as a function of decreasing shear rate for A357 SIMA at a fraction solid of 0.48. Data are from several experiments at low, intermediate, and high compression rates (experiments 1-6).

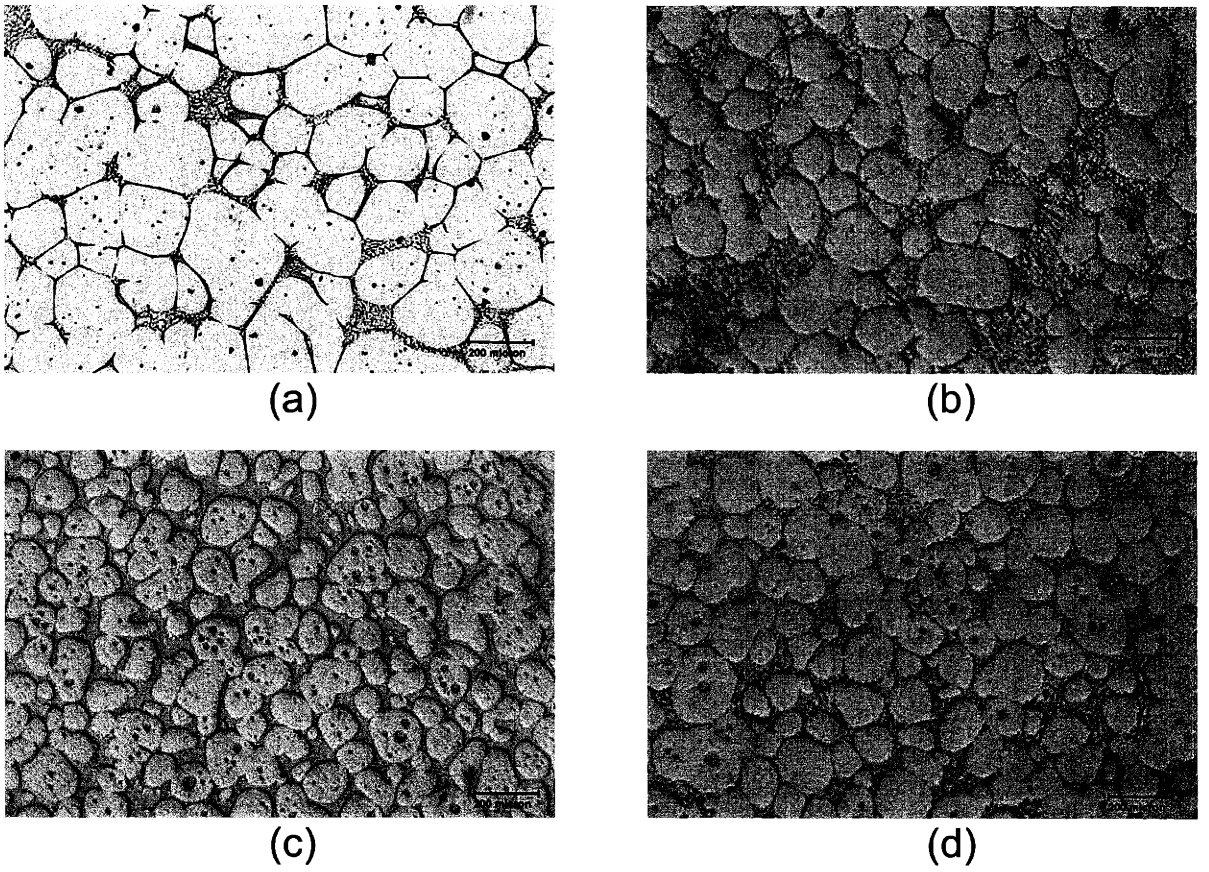

Figure 4-21: Micrographs of as-cast and water quenched material prior to compression: (a) Al-4.5wt%Cu MIT process, (b) modified A356 MIT process, (c) A357 MHD, and (d) A357 SIMA.

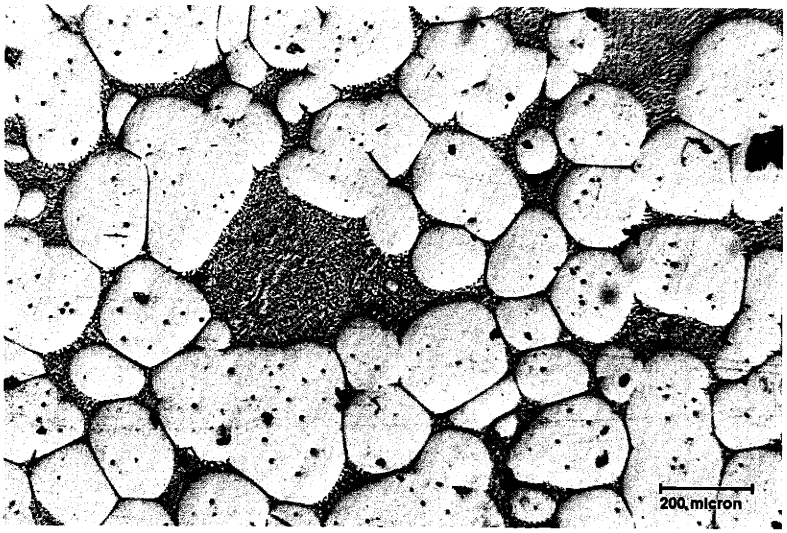

Figure 4-22: Micrograph of Al-4.5wt%Cu quenched prior to compression. Pocket of eutectic liquid is observed in the center of the micrograph.

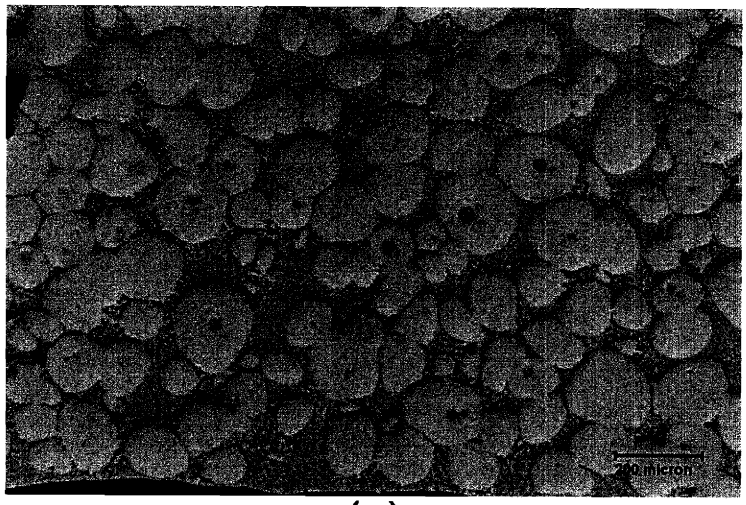

Figure 4-23: Micrographs of a compressed sample (experiment 2) after fast compression from (a) near the radial edge and (b) in the center of the specimen.

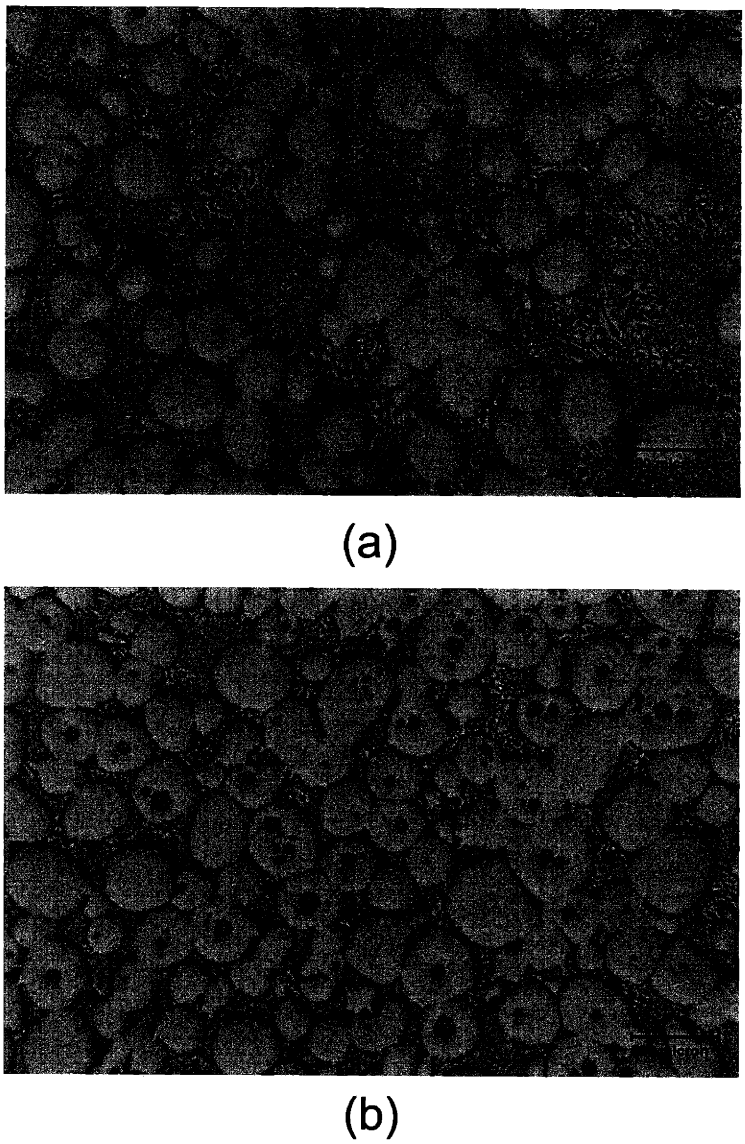

Figure 4-24: Micrographs of a compressed specimen (experiment 5) after slow compression for 16 minutes at (a) the radial edge and (b) the center of the sample.

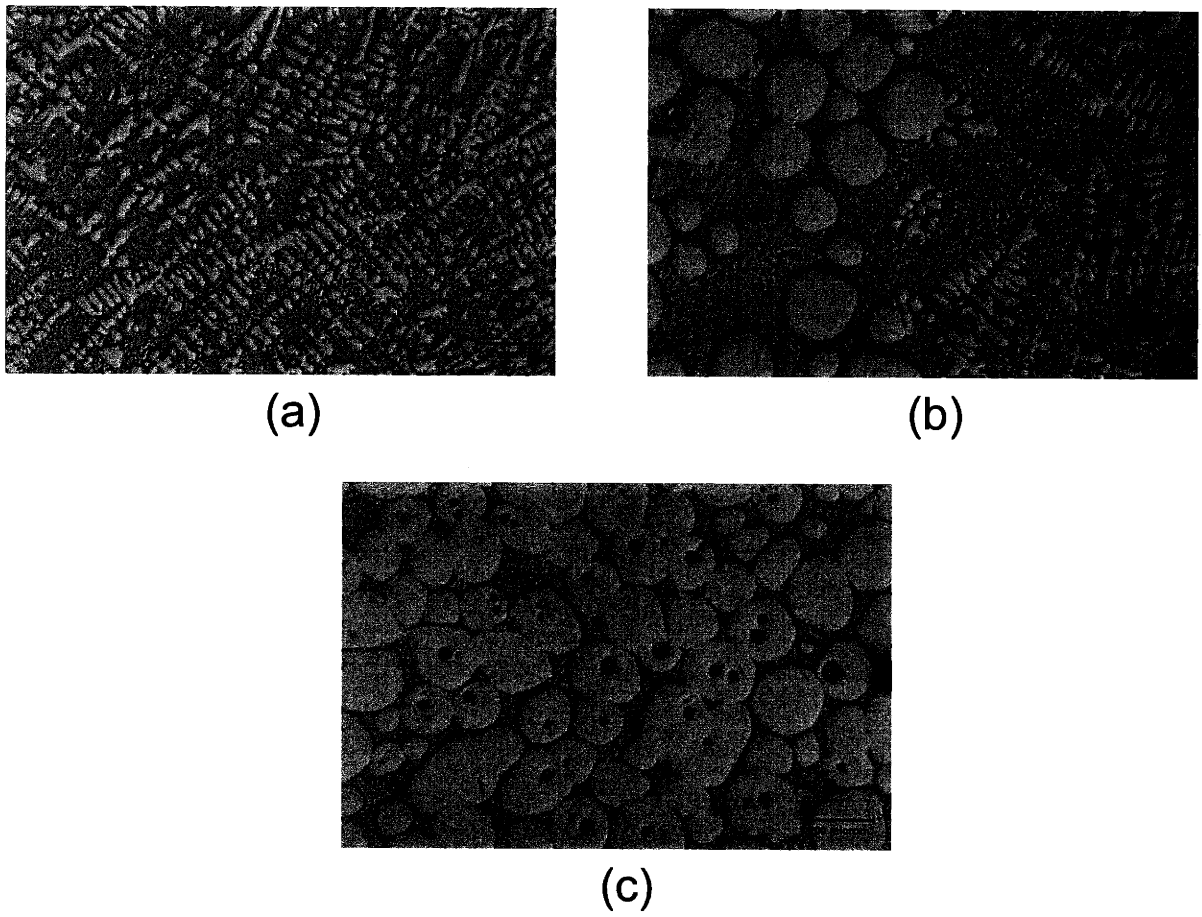

Figure 4-25: Micrographs of a sample (Experiment 6) that was compressed at low shear rates for 4 hours. The radial edge (a) is of eutectic composition indicating segregation of the liquid and solid during compression. The middle of the sample (c) consists of mostly primary grains. A boundary can be seen in (b) separating the two regions.

Chapter 5

Discussion

5.1 High Shear Rate Results

Viscosity results for different aluminum alloys at varying fraction solid were shown in the last chapter. There were several interesting results from the experiments, and these will be discussed in further detail in this section.

5.1.1 Increasing versus Decreasing Shear Rate

As seen in Figure 4-1, the shear rate is generally seen to increase during the first part of a test, and then to decrease. Depending on the fraction solid of the semi-solid sample and the platen height and mass, only one of the flow regimes may be present. In general, as fraction solid decreases and kinetic energy of the platen increases, there is larger probability that only the increasing shear rate regime will be discernible from the data.

The slope of the viscosity curve is significantly different depending on whether the shear rate is increasing or decreasing, as seen in Figure 4-2. In the log-log plot of viscosity as a function of shear rate, the slope of the curve, m, is related to the power-law exponent, n, where $n = m + 1$. The power-law exponent represents the shear stress dependence on shear rate (Equation 2.6).

In the increasing shear rate portion of the experiments, the average calculated value of n was -0.80 ± 0.40. The n-value was calculated from data taken from each alloy, processing route, and fraction solid. Because the power-law index is negative, the shear stress decreases with

increasing shear rate. The significance of a negative n-value was detailed in a recent paper by McLelland *et al.*, stating that it occurs during thixotropic, structural breakdown [63]. There does not appear to be a correlation between n-value and fraction solid or alloy composition in this study.

The n-value in the decreasing shear rate regime was 0.07 ± 0.21, and this value is considerably higher than the increasing shear rate n-value. During the increasing shear rate part of the test, it seems logical that the n-value would be smaller because the fluid is undergoing thixotropic breakdown. By the time the decreasing shear rate part of the test begins, the fluid has undergone significant compression and thus has a power-law index of approximately zero, which is similar to non-thixotropic, shear-thinning fluids. The n-value reported in this work, 0.07, is similar to n-values observed by other researchers under *steady-state* conditions, as seen in Table 5-1. This is a surprising result because the experiments in this work are performed during rapid transients.

Differences in the n-value between the increasing and decreasing shear rate flow regimes could indicate potential error in analyzing data from the early portion of the test. In Chapter 3, the effect of inertia and the non-radial pressure gradient on the Stefan solution were discussed. The inertial effect increases the applied force exerted on the falling platen; therefore, inertia would increase the experimentally determined force and subsequently, the calculated viscosity through the Stefan solution. The inertial effect is more pronounced as $h(t)/h_o \longrightarrow 1$; fortunately, viscosity values are not determined when the dimensionless height is greater than 0.75. The effect of inertia could still exaggerate the force when the dimensionless height is less than 0.75, but it was determined that at a dimensionless height of 0.50, the difference in force calculated with FLOW3D® (with inertia) and the Stefan solution was less than a factor of 1.5, as seen in Figure 3-11. On a log-log plot of viscosity, a factor of 1.5 difference in force would decrease viscosity during the early part of an experiment and increase the n-value (less negative), but not by enough to account for the large differences in n-values calculated for the two flow regimes.

The time required to begin the decreasing shear rate flow regime (region b in Figure 4-2), where the calculated n-value was similar to other researchers' steady-state values, was 4 ms (experiment 2). This transient time to achieve steady-state flow is considerably more rapid

than values previously reported from concentric cylinder experiments, which are on the order of seconds [26], [28], [59].

A comparison of this work with a recent study by de Figueredo *et al.* dramatically shows the decreased transient time [76]. In de Figueredo's experiment, shear rate was increased to a high value, and then the power of their instrument was turned off, to drop the shear rate to zero. The duration of their entire test was 2 seconds, from the start of the increase in shear rate until the shear rate reached zero. Figure 5-1 is a plot of the viscosity versus shear rate from experiment 1 and their work. In both flow curves it can be seen that viscosity remains at a small value after having reached a high shear rate, and the time necessary for the viscosity from this work to decrease to a value comparable to theirs is only 4 ms. It is also remarkable that the viscosity values during the decreasing shear rate period appear independent of time, at least relative to the duration of the two experiments, 6 ms and 2 seconds, respectively.

5.1.2 Viscosity Comparison of Various Alloys and Processing Routes

The calculated viscosity of the various rheocast alloys was compared in several figures in the last chapter (Figures 4-3, 4-4, 4-5, 4-6, 4-7, 4-12, 4-15, 4-16, and 4-17). Some of the major observations from these figures will be discussed in this section.

A357 SIMA

In Figures 4-3, 4-4, and 4-5, viscosity from two A357 SIMA experiments were compared (experiments 1 and 2). During the increase in shear rate (Figure 4-3), both alloys behave similarly, but the lower fraction solid sample achieved a much higher shear rate. The fraction solid difference is insignificant, so the difference in maximum attained shear rate is probably caused by experimental deviation (*i.e.* changes in sample composition or temperature).

The viscosity behavior during the decrease in shear rate (Figure 4-4) is quite different for the two experiments. The fluid that achieved the higher shear rate has a much smaller viscosity during the decreasing portion of the test. Figure 4-5 shows dramatically the effect of attaining a high shear rate. The sample that achieved a 75% larger shear rate had viscosity that was about an order of magnitude smaller than the other for a given shear rate. This observation has significant impact on commercial semi-solid processing. For example, semi-solid metal in a

die-casting process would undergo a large drop in shear rate as the metal entered the die cavity from the gate. Attaining a high shear rate is critical for maintaining a small viscosity during the duration of the forming process. Die design should account for this observation.

Comparison of A357 SIMA, A357 MHD, and A356 MIT

The instantaneous, dimensionless height and apparent viscosity of A356 and A357 rheocast with the MHD, SIMA, and MIT processes can be seen in Figures 4-6 and 4-7 (experiments 1, 2, 7, and 9). The dimensionless height plot shows that the SIMA and MIT material behave quite similarly, but the MHD undergoes less strain (Figure 4-6). Although the MHD sample does not achieve as large of a shear rate, the viscosity of each alloy appears similar (Figure 4-7). An interesting observation of the MHD viscosity is that it agrees with the other materials even though its larger, final dimensionless height clearly indicates it has a higher resistance to flow.

The MHD material used in this study was not the best quality, which can be seen in the as-cast, quenched micrographs in Figure 4-21(c). The shape factor for this alloy (which measures its sphericity) was smaller than the other materials (Table 4-2). Furthermore, MHD material had the largest amount of entrapped eutectic liquid, which increases the material's effective solid fraction because this liquid does not contribute to flow. The only conclusion on the difference between MHD and the other materials in this work is that the resistance to flow was larger for the MHD in this particular set of experiments because of the smaller shape factor and the amount of entrapped eutectic liquid.

The examination of the MIT prepared alloy was the first rheological study performed on this rheocast material. The results are very encouraging because of the similarity in behavior when compared to the SIMA produced material.

Modified A356 MIT

A356 was diluted with pure Al to produce an alloy that contained approximately 30% eutectic. A356 is a difficult alloy to examine at fractions solid above 0.55 because of the narrow temperature range over which the eutectic freezes. The diluted alloy remedies this problem and is referred to as modified A356 in this work (experiments 11-18).

Comparisons of the instantaneous, dimensionless height of modified A356 at varying fraction

solid and platen mass are in Figures 4-8 and 4-9. The results are not surprising in that the final height of the compressed samples decreases with decreasing fraction solid and increasing platen mass. This trend is apparent in a macroscopic photograph of compressed samples (Figure 4-10). Surface cracking of the samples is observed at high fraction solid, greater than 0.60. The highest fraction solid successfully compressed was 0.67, and development of this alloy leads to the belief that alloys with less eutectic than A356 and A357 should be used commercially in the future. A sample with higher fraction solid, between 0.68 and 0.70 was examined in the Drop Forge Viscometer, but the platen did not compress the sample. It is unclear whether a maximum forming limit was attained, possibly corresponding to the theoretical maximum packing fraction, but it is also possible because of the composition that the eutectic phase begins to freeze at this fraction solid.

An interesting observation is the comparison of modified A356 and A357 SIMA at a similar fraction solid (Figure 4-12). The major difference in the two alloys is the amount of eutectic. In A357 at a fraction solid of 0.48, the majority of the liquid is near eutectic composition, while the modified A356 has liquid with less silicon content. It is unclear from literature if solid/liquid surface energy or any other material parameter is affected by this change in the liquid composition. From the plot of viscosity, it appears that both alloys behave in a similar manner regardless of liquid composition for a given volume fraction solid.

Comparison of Al-4.5wt%Cu MIT and Modified A356 MIT

Al-4.5wt%Cu was rheocast with the MIT process and examined at high fractions solid, similar to the modified A356 (experiments 19-24). A plot of instantaneous, dimensionless height for varying fraction solid and platen mass can be seen in Figure 4-13. The plot follows the same trends as the Al-Si alloys, decreasing final height with decreasing solid fraction and increasing platen mass. Viscosity is shear thinning and increases with solid fraction (Figure 4-14).

A surprising result was the large difference in viscosity values of Al-Cu and Al-Si alloys at similar fractions solid (experiments 12, 15, 19, and 24). The instantaneous, dimensionless height of the two alloys at two similar fractions solid can be seen in Figure 4-18. The Al-Cu alloy had a larger, final compressed height for both fractions solid. The Al-Cu alloy was compressed with a mass of 0.917 kg at a fraction solid of 0.46, yet its final height was greater

than the Al-Si sample at a fraction solid of 0.48 compressed with a mass of 0.379 kg. The viscosity curves for these two experiments are in Figures 4-15 and 4-16. There is a dramatic difference in viscosity in these two plots. At the higher fraction solid, the viscosity is plotted as a function of increasing shear rate (Figure 4-17, and although there is no difference in viscosity, there is a large difference in the maximum attained shear rate. Clearly there is a higher resistance to flow in the Al-Cu alloys.

It is unclear why there is a difference in viscosity between the two alloys, but there are several possibilities. From an experimental standpoint, it has already been mentioned that Al-Cu has a higher fraction solid temperature dependence than Al-Si (df_s/dT), but it would be natural to assume that if this were the case, then Al-Cu would have an equally probable chance of having a lower fraction solid than Al-Si for a given experiment. Al-Cu never had a lower viscosity than Al-Si for a comparable experiment.

From a microstructural perspective, the Al-Cu and Al-Si have a similar shape factor (Table 4-2), but upon examination of Figure 4-21, the Al-Cu grains appear larger. It should be noted, however, that the microstructure seen after quenching does not necessarily correspond to what existed during compression. The grain boundaries of the Al-Cu appear to have on average longer contact length, but as mentioned in Chapter 2, two-dimensional micrographs do not give a good picture of the three-dimensional network. From Figure 4-22, it's observed that the Al-Cu does not have as finely dispersed, liquid phase. There is pooling of liquid in certain regions of the sample, which could contribute to an increased viscosity.

Considering the grain boundary contact length of the two alloys, it was thought that a difference in solid/liquid and solid/solid surface energy among the two alloys may account for some difference in the wetting behavior of high-angle grain boundaries. There is little experimental data on the surface energies of these two alloys, but a study was conducted by Gündüz and Hunt on the two alloy systems in question [79]. Using their data for surface energies along with Equation 2.47, it was found that the wetting angles for Al-Si and Al-Cu are 5.2° and 6.5°. The solid/liquid surface energies are for liquid of eutectic composition, and the reported error in their values was 14%. This error does not give great faith in the calculated wetting angles, or that Al-Si necessarily has better wetting characteristics compared with Al-Cu, but it does allow for an interesting discussion.

It was mentioned previously that a partially wet grain boundary will limit the size of a neck that forms between two particles (Equation 2.48). The sinter bond strength is proportional to the fourth power of the neck size, so for a given grain size, the sinter bond strength of Al-Cu is twice as great as Al-Si. This was determined by finding the average contact area between particles based on the limiting neck size and the aforementioned wetting angles. The larger grain size of Al-Cu would also increase the neck size according to Equation 2.48, further increasing the inter-particle strength. The larger particle size would decrease the number of grains per volume and consequently, the number of bonds per volume.

Tzimas and Zavaliangos report that binary Al-Cu has a higher resistance to flow than commercial A2014 Al-Cu alloy [85]. They speculated that the A2014 Al-Cu alloy has third phase precipitates (Fe-Mn) at its grain boundaries that decreased cohesion among grains. The Al-Si alloys in this study do not have any third phases present above the eutectic melt temperature, so that is not a probable explanation. But the fact that Tzimas and Zavaliangos reported that binary Al-Cu has higher flow resistance than a commercial alloy of similar composition means that in the future a better comparison of flow behavior could be made between either binary or commercial alloys.

5.1.3 Effect of Yield Stress on Apparent Viscosity Calculation

Some researchers have claimed that semi-solid slurries possess a yield stress and categorize semi-solid metal as Herschel-Bulkley fluids. The Stefan solution, Equation 2.27, does not account for yield stress when determining apparent viscosity, only viscous stress. If there is a yield stress, and it is of the same order of magnitude as the viscous shear stress, then a different solution would be appropriate for calculating apparent viscosity.

Covey and Stanmore introduced the dimensionless number, S, the plasticity number, to relatively compare viscous and yield stresses (Equation 2.38) [38].

$$S = \frac{R\,(-dh/dt)\,\mu}{h^2 \tau_o}$$

They stated that when $S > 10$, Equation 2.39 is the correct solution for calculation of viscosity.

$$F = \frac{3V^2\mu}{2\pi h^5}\left(\frac{dh}{dt}\right) + \frac{\tau_o V^{3/2}}{\pi^{1/2}h^{5/2}}$$

The equation is similar to the Stefan solution, Equation 2.27, but includes a second term on the right-hand side that accounts for the yield stress effect.

Experimental data from A357 SIMA at a g_s of 0.48 was analyzed to determine whether yield stress would affect the calculation of viscosity (experiment 2). Data analysis for this particular sample occurred after the sample had compressed to sixty-six percent of its original height. The plasticity number, S, was plotted as a function of time, assuming a yield stress of 1000 Pa and a viscosity of 3 Pa·s (Figure 5-4). The value of 1000 Pa for yield stress is within the order of magnitude of reported values for semi-solid alloys at this fraction solid. The viscosity of 3 Pa·s was taken as an average value from the study of de Figueredo *et al.* on their work of A356 at a similar fraction solid and constant shear rate [76]. The viscosity values from de Figueredo are reported as a function of shear rate, but for simplicity in the calculation of S, the value is assumed constant at 3 Pa·s.

The calculated value of S was greater than 1 for a majority of the duration of the experiment, as seen in Figure 5-4. Covey and Stanmore stated that $S > 10$ is a prerequisite for using equation 2.39, but from examining their work it appears that $S > 1$ is also a reasonable condition. Apparent viscosity was recalculated with a yield stress of 1000 Pa using Equation 2.39. Apparent viscosity changed less than *one percent* from the value predicted by the Stefan solution for this experiment, indicating that the yield stress has a minor relative effect compared with the viscous stress. If the yield stress term is significant but known *a priori*, the Drop Forge Viscometer is still an effective tool for extracting rheological data with the modified Stefan solution, Equation 2.39.

5.2 Low Shear Rate Results

5.2.1 Viscosity of A357 SIMA

Besides the high shear rate tests, a number of low shear rate experiments were conducted on reheated A357 SIMA. The results of these tests can be found in Figure 4-19 (experiments 4-6). Instead of being dropped, the platen in the Drop Forge Viscometer was rested on the semi-solid cylindrical sample, and images were acquired periodically for calculation of displacement. Experiments were carried out for different lengths of time, ranging from approximately fifteen minutes to 24 hours. The shear rate was continuously decreasing for all experiments.

The viscosity behavior of the alloys was shear thinning, and it compared well with results from the high shear rate experiments (viscosity as a function of decreasing shear rate), as seen in Figure 4-20. The calculated viscosity agrees over six orders of magnitude of shear rate. The n-value in the linear part of the low shear rate portion of the curve was 0.22, similar to the value of 0.07 for the high shear rate flow regime.

The calculated viscosity agrees from the two types of experiments when the high shear rate results are from the decreasing shear rate portion of an experiment (*e.g.* region (b) in Figure 4-2). This seems logical because the flow has developed into a pseudo-steady-state at this later stage of an experiment. The low shear rate tests are always in a steady-state condition because of the low compression velocities; therefore the data agrees over several orders of magnitude.

5.2.2 Microstructure from High and Low Shear Rate Experiments

Although the viscosity behavior of A357 is similar between the two types of experiments, the microstructure of the compressed samples is very different. It has been reported in previous studies that separation of the liquid and solid phases will occur at low shear rates, and the amount of segregation will decrease with increasing shear rate and fraction solid [84]. At high shear rates there is no apparent phase separation [49].

Micrographs were taken of a sample that was compressed at high compression velocity, as well as two samples that were compressed at low velocities for durations of 16 minutes and 4 hours (Figures 4-23, 4-24, and 4-25). For each sample, micrographs were taken near the outer radial edge and also the center of the sample. Quantitative metallography and EDS

was performed on each sample, and the results are in Tables 4-3 and 4-4. The area fraction calculation is much larger than the other predictions, but this method is known to overestimate calculation of fraction solid, and the results are larger than predictions from Thermo-Calc® or EDS data [90]. The results are still useful because it aides in the relative comparison between regions in the cross section of the compressed sample.

As predicted by previous studies, the fast compression experiment had no discernible segregation (experiment 2). The fraction solid at the radial edge was less than the center, but the difference was minimal (Table 4-4). The difference in calculated fraction solid from the two techniques was 0.05 and 0.08, similar in magnitude to the experimental error in calculating fraction solid. The shape factor of the two regions was 0.80 and 0.83, unchanged from the uncompressed shape factor of 0.81 (Table 4-2). The similarity of the shape factor before and after compression indicates that the particles do not exhibit evidence of large amounts of plastic deformation.

The slow compression experiments that lasted 16 minutes and 4 hours, on the other hand, have evidence of segregation, as predicted by previous studies. The shorter and longer experiments had differences in calculated fraction solid of 0.25 and 0.19, and 0.53 and 0.67, respectively, as determined by the area fraction and lever rule methods. Clearly, there is significant segregation in these two alloys, with the degree of segregation increasing with time (or strain). At the outer edge of the longer duration experiment, the composition is almost entirely eutectic, as seen in Figure 4-25(a), and when this region solidified, dendrites formed. The shape factor from the micrographs (besides Figure 4-25(a)) is the same as the uncompressed material, approximately 0.80-0.83.

The slow compression experiment that was conducted for a short amount of time did exhibit segregation, but not to the extent of the long duration test. One possible explanation for this behavior arises from the coherency theory of dendrites and maximum packing fraction discussed in Chapter 2. Below a certain temperature, the coherency fraction solid (f_s^{ch}), grains are unable to move great distances in the melt because particles are contacting each other, but they can rearrange over short distances by either stress induced grain boundary motion [88] or lubricated sliding [91]. There is a maximum solid fraction, the packing solid fraction (f_s^{pk}), where grains can no longer move by these mechanisms, and fluid flow stops because the solid network supports

the stress of the upper platen. The exact fraction solid that corresponds to the coherency and packing limit are functions of the grain shape and size, and also alloy composition [87].

In the case of the two slow compression experiments, the shorter test did not exhibit complete segregation of the two phases, but the difference in fraction solid from the center to the edge shows that segregation was occurring. Liquid flows interdendritically, because the pressure gradient in the radial direction is minimum at the outer edge of the sample. The fraction solid increased to 0.53 in the center of the sample, but this fraction solid is less than the maximum packing fraction of hard spheres, thus the temperature is in the range $f_s^{ch} < f_s < f_s^{pk}$. This indicates that sliding and re-orientation of grains can occur in the semi-solid sample, but probably not rapidly enough to keep up with radial liquid flow, hence segregation occurs.

In the case of the long-duration experiment, the calculated fraction solid was 0.69, and there were no particles at the outer edge of the compressed sample. A follow up experiment was conducted with a sample being compressed for 24 hours, and its dimensionless height was only one percent less than the four-hour experiment. It appears that a packing limit has been attained that exhibits a yield stress, because no further decrease in height of the sample was measured between 4 and 24 hours. At some point between 15 minutes and 4 hours, it seems that a maximum packing solid fraction was reached in the center of the sample, and liquid was squeezed or ran out under the influence of gravity. Once the solid skeleton compressed to its minimum height (for a given platen mass), fluid flow appears to have ceased because the solid skeleton supports the stress of the platen. It is unclear if the liquid flowed out of the sample before of after the central region reached the maximum packing fraction limit.

5.3 Comparison of the DFV with other Viscometers

One of the main purposes of developing the Drop Forge Viscometer was to create a new instrument that could extract rheological data from reheated semi-solid alloys that agreed with other researchers' results. Viscosity from the last chapter will be compared with data from other studies in this sections.

There have been few studies of semi-solid aluminum alloys at high shear rates and fractions solid above 0.40 because of experimental limitations of specific rheometers and high temper-

atures. Loué used the back-extrusion technique on aluminum at high shear rates, and complemented his high shear rate data with the parallel-plate compression method for low shear rates [49]. de Figueredo *et al.* used a parallel-plate rotational viscometer on MHD A357 at a fraction solid of 0.48 up to steady-state shear rates of 900 s^{-1} [76]. Figures 5-2 and 5-3 are plots of the results from these studies compared with the work from this thesis. It is noted that the viscosity values from de Figueredo in Figure ?? are from steady-state experiments, not transient results cited from their work in an earlier section of this chapter.

The Drop Forge Viscometer produced results that agree well with other researchers. In Figure 5-2, it can be seen that the results from this thesis are similar to the Al-Si alloy studied by Loué at a fraction solid of 0.45. Considering the difficulty in calculating fraction solid and shear rate in a non-homogeneous flow field, it is remarkable that the apparent viscosity results are similar over six orders of magnitude of shear rate. Loué used two different instruments to examine the wide range in shear rate, while this experiment only needed one. The viscosity values of de Figueredo are also similar.

5.4 Engineering Applications of the Drop Forge Viscometer

The Drop Forge Viscometer can serve as a useful process-control and characterization tool for semi-solid alloys. The common commercial techniques for creating semi-solid metal, SIMA and MHD, were conducted at the primary aluminum producer, but lately, rheocasting processes that produce the semi-solid structure at the end user's facility have gained momentum. Quality control must be performed at the end user site where the desired microstructure is created. The drop forge viscometer is a potential tool for determining whether semi-solid slurry is adequate for processing. Periodically drawn, compressed samples could be compared to indexes of either (a) previously compressed specimens or (b) force versus time curves of ideal semi-solid samples. A photograph of a dendritic and non-dendritic sample shows the stark contrast in behavior during compression, as seen in Figure 5-5.

Atkinson *et al.* has proposed that the force curve from compression may be used to determine an appropriate rheological model for describing the flow-behavior of semi-solid alloys [92]. Using the computational fluid dynamics software program FLOW3D®, a mesh is generated

that has the same geometry as the Drop Forge Viscometer (Appendix B). In the modeling code, Newtonian and non-Newtonian rheological models based on the Carreau model (Equation 2.12) are inserted. The model appears as follows, where μ is the fluid viscosity, μ_o is the viscosity at zero shear rate, μ_∞ is the viscosity at infinite shear rate, n is the power-law exponent, II_{2D} is the second invariant of the rate of deformation tensor, and λ_0 and λ_1 are curve fitting constants.

$$\mu = \mu_\infty + \frac{\mu_o - \mu_\infty}{\left(\lambda_0 + \lambda_1^2 II_{2D}\right)^{\frac{1-n}{2}}}$$

The Carreau-Yasuda model is very powerful because many non-Newtonian fluids can be curve fit with this equation. Besides inserting the viscosity model, the experimental plate velocity is used as the boundary condition of the upper platen as a function of time. FLOW3D® calculates the force the fluid exerts on the platen during compression, and comparing this with the experimentally calculated force, the validity of the rheological model can be established. If the viscosity model is not known *a priori*, an iterative process can be undertaken, changing fluid model parameters until the predicted force agrees with the experimentally determined force.

The software was used to verify that the viscosity reported in Figure 4-20 could predict a force that was similar to the experimentally calculated value. The data in Figure 4-20 were curve fit using the Carreau-Yasuda model with the following inserted parameters.

$$\mu = 0.1 + \frac{8e7 - 0.1}{\left(1 + 100000^2 II_{2D}\right)^{\frac{1-0.1}{2}}}$$

In Figure 5-6, force is compared from modeling predictions and experimental data. The upper platen velocity as a function of time (experiment 2) was inserted into the modeling software, along with a Newtonian viscosity, and the predicted results were similar to the force value calculated using the Stefan Equation with the same viscosity and platen speed (Equation 2.27). This agreement verifies that the modeling program can accurately predict force that agrees with the classic solution. A non-Newtonian model, curve fit from Figure 4-20, was implemented, and the predicted force values were within a factor of 3 from the experimental data, as seen in Figure 5-6. The much better agreement of the predicted force results using the shear thinning, non-Newtonian model with the experimentally determined force indicates that a model of this type is much better at predicting flow behavior than a Newtonian viscosity.

Researcher	n-value	f_s	Shear Rate Range (s^{-1})	alloy
McLelland [63]	-0.3	0.50	2-50	Sn-Pb
Quaak [64]	-0.3	0.40	0.4-200	Al-Si
Moon [93]	0.13	0.40	160-900	Al-Si
Loué [49]	0.05	0.55	$10^{-3} - 10^{3}$	Al-Si
Loué [49]	-0.06	0.45	$10^{-3} - 10^{3}$	Al-Si
de Figueredo [76]	-0.57	0.48	400-900	Al-Si
Martin [61]	> 1	0.50	0-800	Al-Si
Kattamis [58]	0.10	0.40	70-570	Al-Cu
Gebelin [70]	0.13	0.58	$10^{-3} - 10^{3}$	AZ91 Mg
THIS WORK	0.1	0.48	$10^{-5} - 10^{3}$	Al-Si

Table 5.1: Comparison of n-values from previous studies and this work.

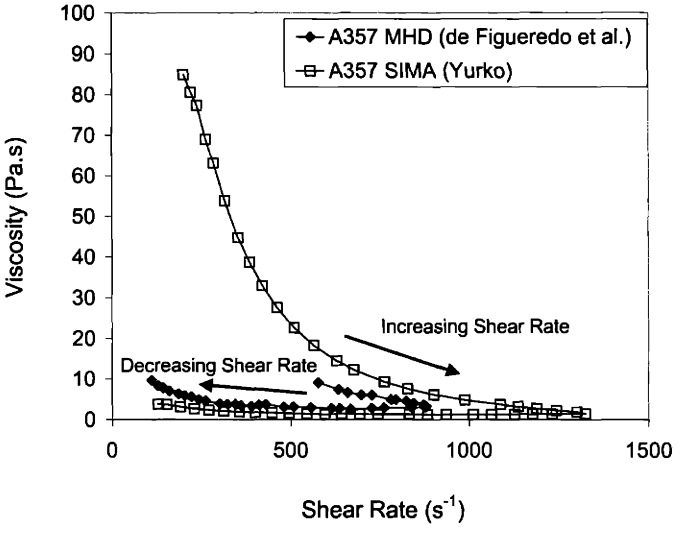

Figure 5-1: Comparison of viscosity versus shear rate for A357 at $g_s = 0.48$ from this work and de Figueredo *et al.* under a transient shear rate flow condition. The duration of the experiment from this work and also de Figueredo were 6 milliseconds and 2 seconds, respectively. After 4 ms, the calculated viscosity from this work was comparable to de Figueredo [76], indicating that the transient time for thixotropic breakdown is on the order of milliseconds.

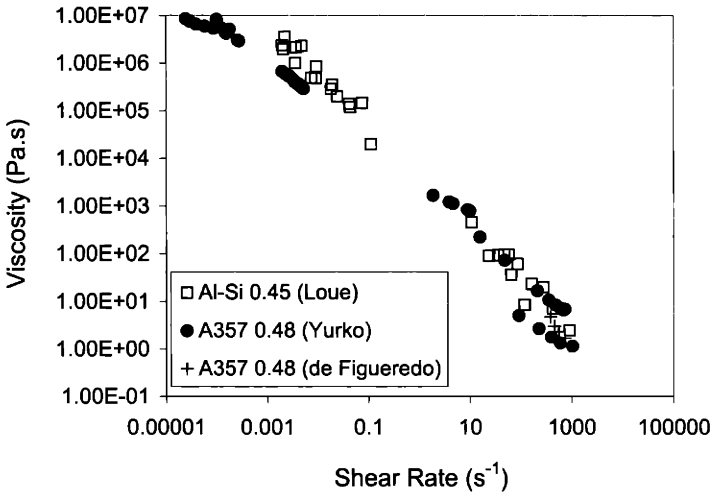

Figure 5-2: Comparison of A357 SIMA at a fraction solid of 0.48 (experiments 1-6) compressed with the Drop Forge Viscometer and similar alloys examined by other researchers [49],[76].

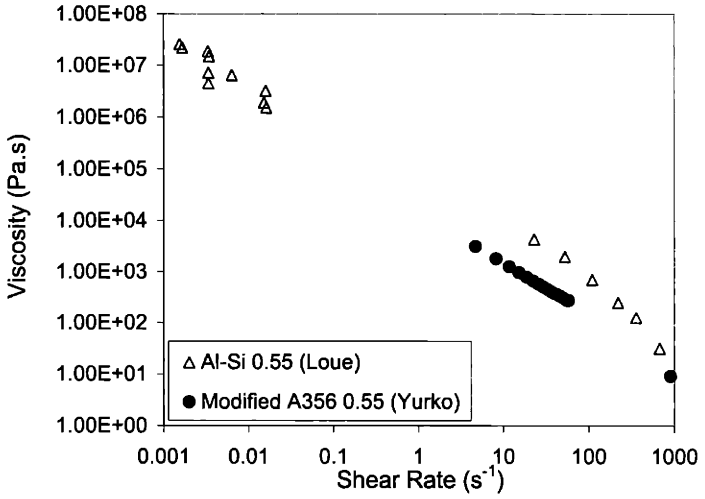

Figure 5-3: Comparison of modified A356 at a fraction solid of 0.55 (experiment 15) compressed in the Drop Forge Viscometer and an Al-Si alloy examined by Loué with the back-extrusion technique [49].

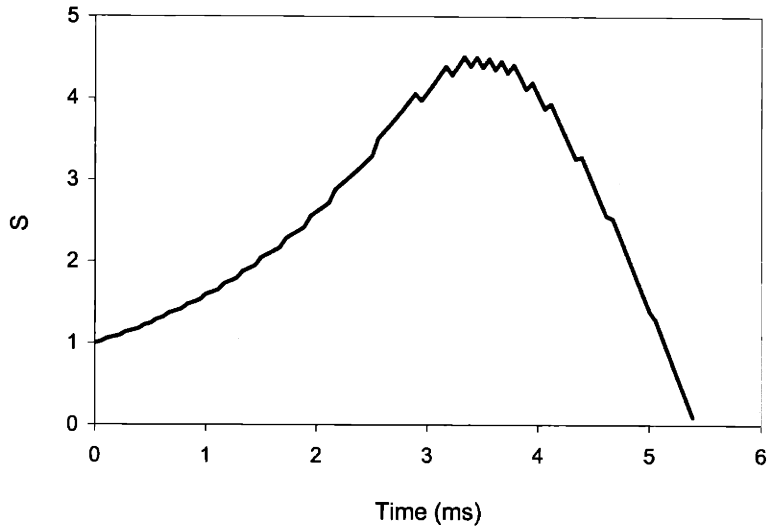

Figure 5-4: Plot of the dimensionless plasticity number, S, as a function of time for experiment 2 with an assumed yield stress of 1000 Pa and a viscosity of 3 Pa·s.

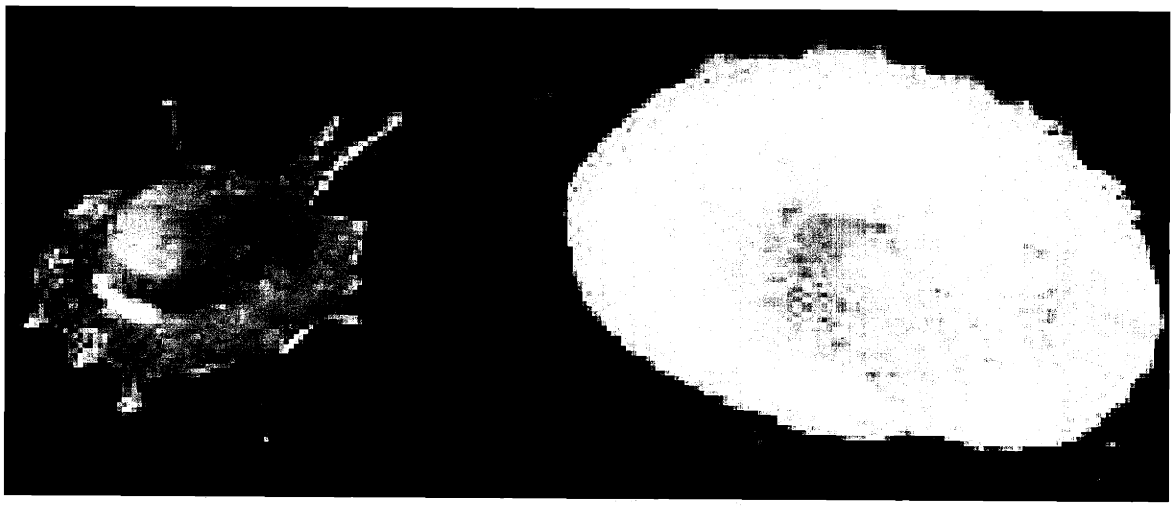

Figure 5-5: Comparison of dendritic and non-dendritic semi-solid samples compressed in the Drop Forge Viscometer. The effect of microstructure on the final shape of the sample is evident.

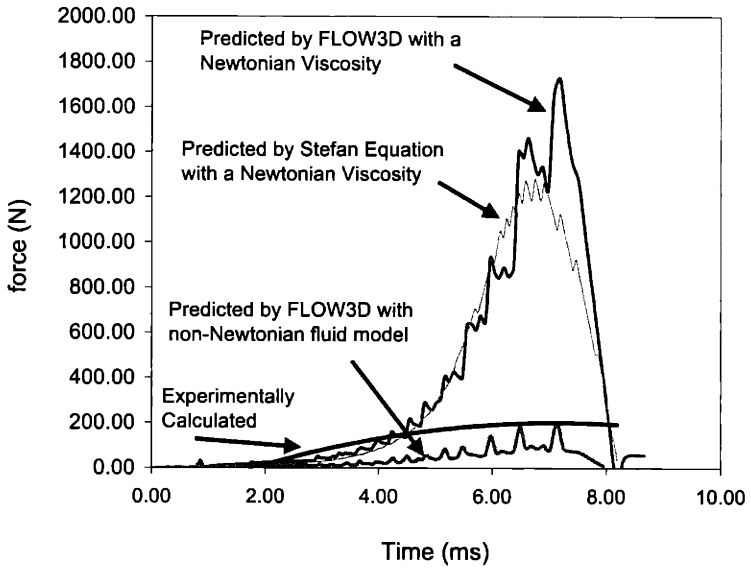

Figure 5-6: Comparison of force determined from an experiment and predicted by modeling. The upper platen velocity from an experiment was input in FLOW3D®, and force was predicted with both a Newtonian and non-Newtonian fluid model. Force was also determined with the Stefan equation, using the experimental platen velocity and Newtonian viscosity. The non-Newtonian model was based on a curve fit of data from Figure 4-20.

Chapter 6

Conclusions

1. A novel apparatus, the Drop Forge Viscometer (DFV) was designed and constructed based on the parallel-plate compression viscometer. The viscometer permits calculating force from the second derivative of the displacement data allowing calculations of viscosities at shear rates in excess of 10^3 s^{-1}. Total duration of a test can be less than 10 ms. Alternatively, the DFV can be operated as a conventional parallel-plate viscometer, attaining shear rates as low as 10^{-5} s^{-1}.

2. A unique feature of the DFV is that a typical experiment yields instantaneous, volume-averaged viscosity first under rapidly increasing shear rate and then under rapidly decreasing shear rate.

3. The apparatus was used to determine the viscosity as a function of shear rate and fraction solid for alloys of non-dendritic structure produced by three means, known as the SIMA, MHD, and MIT processes. The viscosity of the MIT material was similar to alloys produced by the commercial SIMA and MHD processes.

4. Most compression tests in this work (all of the rapid compression tests) were completed within about 6 ms. During the increased shear rate portion of a typical test (lasting about 4 ms), the viscosity dropped by 1-2 orders of magnitude. Viscosity during the decreasing shear rate period decreased with increasing maximum increasing shear rate. For example, in two

SIMA alloys of about 0.48 volume fraction solid (g_s), the viscosity calculated at 100 s^{-1} was an order of magnitude greater than a sample that achieved a 75% higher shear rate.

5. Viscosity versus increasing shear rate of the Al-Si alloys at 0.48 g_s produced by the three different process routes all showed roughly the same viscosity as a function of shear rate, ranging from 300 Pa·s at 120 s^{-1} to 2.2 Pa·s at 1500 s^{-1}.

6. Viscosity as a function of increasing shear rate of the Al-4.5wt%Cu alloy was larger than an Al-Si alloy for a fraction solid of about 0.48, but the viscosity was about the same as an Al-Si alloy at 0.56 g_s. The final compressed height of the Al-Cu was always greater than an Al-Si alloy for similar experimental conditions.

7. Visual examination of cross sections did not show separation of liquid and solid phases in any of the rapidly compressed samples in the shear rate range of 10 to 1500 s^{-1}. Segregation was not detected by either quantitative metallography or chemical composition variation in an A357 SIMA sample that had been compressed at a fraction solid of 0.48 and at shear rates ranging between 15 and 750 s^{-1}. However, when the DFV was used as a conventional parallel-plate viscometer to achieve very low shear rates, there was a fraction solid variation from center to edge of 0.20 (calculated from variation in chemical composition) after compression for 15 minutes in the shear rate range of 10^{-2} to 10^{-4} s^{-1}. A sample that was compressed for four hours at shear rates of 10^{-2} to 10^{-5} s^{-1} had a fraction solid of approximately zero at the edge and 0.70 in the center. Segregation appears to increase with increasing strain in the low shear rate experiments.

8. The maximum fraction solid that was compressed with the DFV at high and low compression velocity was 0.67 and 0.70, respectively.

9. The DFV is a useful process-control tool for comparing the relative compression behavior of semi-solid alloys in the two-phase temperature region. Differences between samples are reflected in the final shape and thickness of the compressed samples, and also in the displacement data.

10. The DFV provides unique transient rheological data of particular relevance to the

modeling of semi-solid processing. Validation of rheological models was achieved by comparing experimental results with model predictions.

Future Work

1. The Drop Forge Viscometer is a simple, robust technique for characterizing the flow behavior of semi-solid alloys at transient, high shear rates; therefore, it could be used to examine other non-Newtonian fluids such as polymers, glass, food products, *etc.* Besides examining reheated, rheocast alloys, it would be interesting to adapt the DFV for examining rheocast alloys cooled directly from the liquid state. Rheocasting has advantages over thixocasting, and understanding how the flow behavior changes with cooling time and structure evolution during the short time between processing and forming is important.

2. The most interesting conclusion from this thesis is that instantaneous viscosity has strong functional dependence on shear rate, and not time. Viscosity approaches steady state values after only milliseconds of shear, and it remains there for a duration much longer than the time required for a typical forming operation. This knowledge should be utilized during the design of dies and even new processes.

3. The semi-solid microstructure is very complex, with fast kinetic processes occurring at the interface of the solid and liquid phases (solidification, coarsening, coalescence). Differences in flow behavior caused by a semi-solid alloy's composition and rheocast processing route will be easier to explain with a more fundamental understanding of the interface kinetic processes, leading to new constitutive relationships.

Appendix A

Calculation of Fraction Solid

When determining the fraction solid of an alloy at any temperature, there are two limiting cases: complete diffusion in the solid and liquid phases (equilibrium solidification) or no back diffusion in the solid (non-equilibrium solidification) [94]. The predicted fraction solid from the two methods is similar and only begins to deviate at fractions solid near the eutectic temperature in alloys that have very small amounts of eutectic (Figure A-1). Because experiments in this thesis were near a fraction solid of 0.5, the non-equilibrium method was used to predict fraction solid.

The Scheil Equation or *non-equilibrium lever rule* is used to determine fraction solid in the case of no back diffusion of the solid, where C_L^* and C_S^* are the liquid and solid equilibrium compositions, respectively, and $C_L = C_L^*$ because of diffusion in the liquid.

$$(C_L - C_S^*)df_s = (1 - f_s)dC_L \tag{A.1}$$

Substituting the partition ratio, k, (k is the ratio of the equilibrium solidus and liquidus compositions, C_S^*/C_L^*) into Equation A.1 and integrating from $C_S^* = kC_o$ (C_o is the alloy composition) at $f_s = 0$ results in

$$C_S^* = kC_o(1 - f_s)^{(k-1)} \tag{A.2}$$

Equation A.2 can be rearranged so that fraction solid is a function of solid composition, the partition ratio, and the alloy composition.

$$f_s = 1 - \left(\frac{C_S^*}{kC_o}\right)^{\frac{1}{k-1}} \tag{A.3}$$

Following example 30 of the Thermo-Calc® Examples Manual [95], the fraction solid was calculated for A357, modified A356, and the Al-4.5wt%Cu. Figures 3-3, 3-4, and 3-5 are plots of the weight percent fraction solid versus temperature as predicted by Thermo-Calc®. The program uses an iterative process to evaluate the liquid composition after rejection of solute by the solid phase and maintains a mass balance. The major benefit to using Thermo-Calc® is that it evaluates the partition ratio as a function of temperature, instead of assuming that it is linear throughout the two phase region.

Similar to rheology studies on suspensions, experiments conducted on semi-solid alloys requires knowledge of volume fraction solid. The volume fraction solid, g_s, can be calculated from the weight percent fraction solid using the following equation.

$$gs = \frac{fs}{fs + (1 - fs) \cdot \frac{\rho_S}{\rho_L}} \tag{A.4}$$

where ρ_L and ρ_S are the densities of the liquid and solid phases, respectively. Densities for the liquid and solid phases as a function of composition for the Al-Cu system have been reported in the literature [96], but there has not been a corresponding study for Al-Si. Estimated values were taken from Viswanathan, and the deviation between weight fraction solid and volume fraction solid was minimal [97]. The densities of the liquid and solid phases in the Al-Cu alloy over the fraction solid studied were the same, therefore g_s and f_s are equal. In A357, the densities of the liquid and solid were estimated at 2.45 g/cm^3 and 2.54 g/cm^3, respectively. The volume fraction solid value is one percent fraction solid less than the weight percent value. For example, if $f_s = 0.48$, then $g_s = 0.47$. It was assumed that the diluted A356 would have the same deviation as the A357.

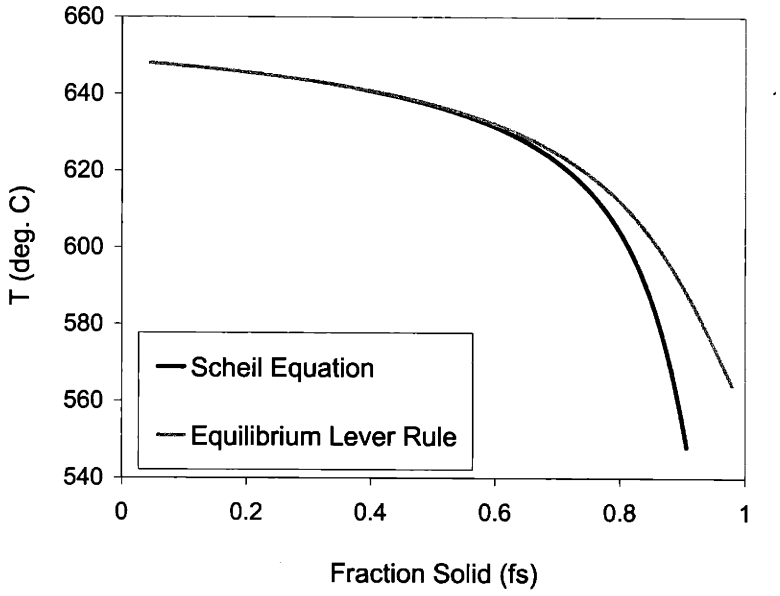

Figure A-1: Comparison of fraction solid prediction using the equilibrium lever rule and the Scheil Equation for Al-4.5wt%Cu. A deviation in fraction solid is only apparent at high fraction solid.

Appendix B

FLOW3D® Modeling Code

The following text is the code of the mesh for an SSM cylinder compressed by a falling platen from experiment 2. This file is modified from the original work of Barkhudarov at Flow Science. A similar version of this geometry and mesh was originally used by Kapranos *et al.* at the University of Sheffield [50]. The flow model was a non-Newtonian, Carreau model fit to Figure 4-20 in this work. The viscosity model and compression velocity are changed to produce the various plots seen in this thesis. Units are in MKS.

```
$xput
remark='overall control parameters',
twfin=0.0085, remark='set finish time, initial dt',
remark='turn on wall shear',
itb=1, remark='free surface tracking',
gz=-9.8, remark='turn on gravity',
impvis=1, remark='turn on implicit viscous option',
ipdis=1,autot=2., imobs=1, ifpk=0,
epsadj=0.1,hpltdt=0.0,
dum3=1.0, dum4=2.0,
ifvis=0,
$end
$limits
```

```
remark='iteration and print limits',
itvsmx=25, remark='limit implicit viscous iterations',
$end
$props
rhof=2.5e+03, remark='set fluid viscosity, density',
mu1=80000000.,
muc00=0., muc0=1., muc1=100000., muc2=0.1,
muc3=0.1,
$end
$bcdata
remark='boundary types',
wl=1, wr=3, remark='left=symmetry,bottom=continuative',
$end
$mesh remark='lower platen is at z=0.005 m',
icyl=1,                remark='upper platen at t=0, z=0.025m',
nxcelt=60,
px(2)=4.5e-02,
nzcelt=45,
pz(1)=0.0e-02,
pz(2)=0.50e-02, sizez(2)=0.05e-02,
pz(3)=2.5e-02,
nycelt=1,
$end
$obs
avrck=-2.1, remark='turn on obstacle smoothing',
nobs=2,
    remark='the following array defines the velocity of the platen',
    remark='at a given time during the experiment. Only the beginning',
    remark='and final 5 velocities during the test are shown',
    remark='TOBS defines the time in seconds and WTOBS the velocity in m/s.',
```

```
zh(1)=0.50e-02, ifrco(1)=1,
zl(2)=2.2e-02, imo(2)=1,
TOBS(1)=0.000000000,        WTOBS(1,2)=-2.350,
TOBS(2)=0.000851100,        WTOBS(2,2)=-2.341,
TOBS(3)=0.000906656,        WTOBS(3,2)=-2.353,
TOBS(4)=0.000962211,        WTOBS(4,2)=-2.363,
TOBS(5)=0.001017767,        WTOBS(5,2)=-2.372,
TOBS(130)=0.007962211,      WTOBS(130,2)=-0.128,
TOBS(131)=0.008017767,      WTOBS(131,2)=-0.099,
TOBS(132)=0.008073322,      WTOBS(132,2)=-0.070,
TOBS(133)=0.008128878,      WTOBS(133,2)=-0.042,
TOBS(134)=0.008184433,      WTOBS(134,2)=-0.014,
ioh(1)=1, ioh(2)=1,
$end
$fl
nfls=1,
frah(1)=1.25e-02, fzh(1)=2.0e-02, wi=0.0e-02,
$end
$bf,$end
$temp,$end
$motn,$end
$grafic
remark='specify desired output plots',
isymx=1, remark='reflect symmetry accross x=0.0',
nvplts=4, contpv(1)='stnr', ivtyp(2)=1,
contpv(3)='p',
contpv(4)='mu',
$end
$parts
$end
```

Bibliography

[1] C.W. Macosko, Rheology: Principles, Measurements, and Applications, Wiley-VCH, New York, (1994).

[2] D.J. Jeffrey and A. Acrivos, "The Rheological Properties of Suspensions of Rigid Particles.", *AIChE,* **22** (2) (1976), 417-432.

[3] A. Einstein, Investigations on the Theory of the Brownian Movement, Dover, New York, (1956).

[4] R. Rutgers, "Relative Viscosity of Suspensions of Rigid Spheres in Newtonian Liquids", *Rheol. Acta,* **2** (1962), 202-210.

[5] D.G. Thomas, "Transport Characteristics of Suspensions: VIII. A Note on the Viscosity of Newtonian Suspensions of Uniform Spherical Particles", *Journal of Colloid Science,* **20** (1965), 267-277.

[6] I.M. Krieger and T.J. Dougherty, "A Mechanism for Non-Newtonian Flow in Suspensions of Rigid Spheres", *Trans. Soc. Rheol.,* **3** (1959), 111-136.

[7] N.A. Frankel and A. Acrivos, "On the Viscosity of a Concentrated Suspension of Solid Spheres", *Chemical Engineering Science,* **22** (1967), 847-853.

[8] G.K. Batchelor, "The Stress System in a Supension of Force-Free Particles", *J. Fluid Mech.,* **41** (1970), 545-570.

[9] W.B. Russel and A.P. Gast, "Nonequilibrium Statistical Mechanics of Concentrated Colloidal Dispersions: Hard Spheres in Weak Flows", *J. Chem. Phys.,* **84** (3) (1986), 1815-1826.

[10] N. Phan-Thien, "Constitutive Equation for Concentrated Suspensions in Newtonian Liquids", *J. Rheol.*, **39** (4) (1995), 679-695.

[11] N. Phan-Thien, X.J. Fan, and B.C. Khoo, "A New Constitutive Model for Monodispersed Suspensions of Spheres at High Concentrations", *Rheol. Acta*, **38** (1999), 297-304.

[12] D.R. Poirier and G.H. Geiger, Transport Phenomena in Materials Processing, TMS, Warrendale, PA, (1994).

[13] D.M. Husband, N. Aksel, and W. Gleissle, "The Existence of Static Yield Stresses in Suspensions Containing Noncolloidal Particles", *J. Rheol.*, **37** (2) (1993), 215-235.

[14] I.M. Krieger, "Rheology of Monodisperse Latices", *Advan. Colloid Interface Sci.*, **3** (1972), 111-136.

[15] H.M. Laun, "Rheology and Particle Structures of Concentrated Polymer Dispersions", Xth International Congress on Rheology, Sydney (1988).

[16] J.D. Lee, J.H. So, and S.M. Yang, "Rheological Behavior and Stability of Concentrated Silica Suspensions", *J. Rheol.,* **43** (5) (1999), 1117-1140.

[17] A.B. Metzner and M. Whitlock, "Flow Behaviour of Concentrated (Dilatant) Suspensions", *Trans. Soc. Rheol.*, **2** (1958), 239-254.

[18] R.L. Hoffman, "Discontinuous and Dilatant Viscosity Behaviour in Concentrated Suspensions. I. Observation of a Flow Instability", *Trans. Soc. Rheol.*, **16** (1972), 155-173.

[19] H.A. Barnes, "Shear Thickening ("Dilatancy") in Suspensions of Nonaggregating Solid Particles Dispersed in Newtonian Liquids", *J. Rheol.*, **33** (1989), 329-366.

[20] H. Watanabe, *et al.*, "Nonlinear Rheological Behavior of a Concentrated Spherical Silica Suspension", *Rheol. Acta*, **35** (1996), 433-445.

[21] Q.D. Nguyen and D.V. Boger, "Yield Stress Measurement for Concentrated Suspensions", *J. Rheol.*, **27** (4) (1983), 321-349.

[22] W.H. Bauer and E. A. Collins, "Thixotropy and Dilatancy" in Rheology: Theory and Applications, F. R. Eirich, Academic Press, New York, (1967), 423-459.

[23] J. Mewis, "Thixotropy - A General Review." *J. Non-Newt. Fluid Mech.*, **6** (1979), 1-20.

[24] A. Slibar and P.R. Paslay in M. Reiner and D. Abir (Eds.), *Proc. Int. Symp. on Second-Order Effects in Elasticity Plasticity and Fluid Dynamics*, Pergamon Press, Oxford, (1964).

[25] D. C.-H. Cheng and F. Evans, "Phenomenological Characterization of the Rheological Behaviour of Inelastic Reversible Thixotropic and Antithixotropic Fluids." *Brit. J. Appl. Phys.*, **16** (1965), 1599-1617.

[26] M. Mada and F. Ajersch, "Rheological Model of Semi-Solid A356-SiC Composite Alloys. Part I. Dissociation of Agglomerate Structures During Shear", *Mat. Sci. Eng.*, **A212** (1996), 157-170.

[27] M. Mooney, *J. Colloid Sci.*, **1** (1946).

[28] P. Kumar, C.L. Martin, and S. Brown, "Shear Rate Thickening Flow Behavior of Semisolid Slurries", *Met. Trans.*, **24A** (1993), 1107-1116.

[29] M. Perez, *et al.*, "Computer Simulation of the Microstructure and Rheology of Semi-Solid Alloys Under Shear", *Acta Mater.*, **48** (2000), 3773-3782.

[30] F. Gadala-Maria and A. Acrivos, "Shear-Induced Structure in a Concentrated Suspension of Solid Spheres", *J. Rheol.*, **24** (6) (1980), 799-814.

[31] D.M. Husband, *et al.*, "Direct Measurements of Shear-Induced Particle Migration in Suspensions of Bimodal Spheres", *Rheol. Acta*, **33** (1994), 185-192.

[32] I. Williams, "The Plasticity of Rubber and its Measurements", *Ind. Eng. Chem.*, **16** (1924), 362.

[33] M.J. Stefan, "Versuche Über Die Scheinbare Adhäsion", *Akad. Wiss. Wien. Math.-Natur. Klasse. Abt. 2*, **69** (1874), 713-735.

[34] R.W. Griffiths, "The Plasticity of Unvulcanized Rubber", *IRI Transactions*, **1** (1926), 308-341.

[35] G.J. Dienes and H.F. Klemm, "Theory and Application of the Parallel-Plate Plastometer", *J. Appl. Phys.*, **17** (1946), 458-471.

[36] V. Laxmanan and M.C. Flemings, "Deformation of Semi-Solid Sn-15 Pct Pb Alloy", *Met. Trans.*, **11A** (1980), 1927-1937.

[37] J.R. Scott, "Theory and Application of the Parallel-Plate Plastimeter", *IRI Transactions*, **7** (1931), 169-185.

[38] G.H. Covey and B.R. Stanmore, "Use of the Parallel-Plate Plastometer for the Characterisation of Viscous Fluids with a Yield Stress", *J. Non-Newt. Fluid Mech.*, **8** (1981), 249-260.

[39] P.J. Leider and R.B. Bird, "Squeezing Flow between Parallel Disks. I. Theoretical Analysis", *Ind. Eng. Chem. Fundam.*, **13** (4) (1974), 336-341.

[40] H.M. Laun, "Rheometry Towards Complex Flows: Squeeze Flow Technique", *Makromol. Chem., Macromol. Symp.*, **56** (1992), 55-66.

[41] W. Zhang, N. Silvi, and J. Vlachopoulos, "Modelling and Experiments of Squeezing Flow of Polymer Melts", *Int. Polym. Proc.*, **X** (1995), 155-164.

[42] T. Kitano and T. Kataoka, "The Effect of the Mixing Methods on Viscous Properties of Polyethylene Melts Filled with Fibers", *Rheol. Acta,* **19** (1980), 753-763.

[43] A. Lawal and D.M. Kalyon, "Compressive Squeeze Flow of Generalized Newtonian Fluids with Apparent Wall Slip", *Int. Polym. Proc.*, **XV** (2000), 63-71.

[44] W.M. Gearhart and W.D. Kennedy, "Cellulose Acetate Butyrate Plastics: High Temperature Evaluation of Plasticizers by the Parallel Plate Plastometer", *Ind. Eng. Chem.*, **41** (4) (1949), 695-701.

[45] G. Winther, K. Almdal, and O. Kramer, "Determination of Polymer Melt Viscosity by Squeezing Flow With Constant Plate Velocity", *J. Non-Newt. Fluid Mech.,* **39** (1991), 119-136.

[46] A.V. Tungare, G.C. Martin, and J.T. Gotro, "Chemorheological Characterization of Thermoset Cure", *Poly. Eng. Sci.*, **28** (16) (1988), 1071-1075.

[47] S.J. Wilson and D. Poole, "Glass Viscosity Measurement By Parallel-Plate Rheometry", *Mat. Res. Bull.*, **25** (1990), 113-118.

[48] M. Mada and F. Ajersch, "Viscosity Measurements of A356-15% Si Semi-Solid Alloys Using a Squeezing Flow Viscometer", *Proc. of the Sec. Int. Conf. on the Processing of Semi-Solid Alloys and Composites*, Cambridge, MA (1992), 276-289.

[49] W.R. Loué, M. Suéry, and J.L. Querbes, "Microstructure and Rheology of Partially Remelted AlSi-Alloys", *Proc. of the Sec. Int. Conf. on the Processing of Semi-Solid Alloys and Composites*, Cambridge, MA (1992), 266-275.

[50] P. Kaprano, D.H. Kirkwood, and M.R. Barkhudarov, "Modeling of Structural Breakdown During Rapid Compression of Semi-Solid Alloy Slugs", *Proc. of the Fifth Int. Conf. on the Processing of Semi-Solid Alloys and Composites*, Golden, CO (1998), 11-19.

[51] J.A. Goshawk, *et al.*, "Rheological Phenomena Occurring During the Shearing Flow of Mayonnaise", *J. Rheol.*, **42** (6) (1998), 1537-1553.

[52] B. Hoffner, C. Gerhards, and M. Peleg, "Imperfect Lubricated Squeezing Flow Viscometry for Foods", *Rheol. Acta*, **36** (1997), 686-693.

[53] H.M. Laun, M. Rady, and O. Hassager, "Analytical Solutions for Squeeze Flow with Partial Wall Slip", *J. Non-Newt. Fluid Mech.*, **81** (1999), 1-15.

[54] D.B. Spencer, "Rheology of Liquid-Solid Mixtures of Lead-Tin", *Sc.D. Thesis*, MIT, (1971).

[55] M.C. Flemings, "Behavior of Metal Alloys in the Semisolid State", *Met. Trans.*, **22B** (1991), 269-293.

[56] R.A. Martinez-Ayers, "A New Technique for the Formation of Semisolid Structures", *S.M. Thesis*, MIT, (2001).

[57] X. Pan, *et al.*, "Trend and Development of Semi-Solid Metal Processing", *J. Mater. Sci. Technol.*, **16** (5) (2000).

[58] T.Z. Kattamis and T.J. Piccone, "Rheology of Semisolid Al-4.5wt%Cu-1.5wt%Mg Alloy", *Mat. Sci. Eng.*, **A131** (1991), 265-272.

[59] L.S. Turng and K.K. Wang, "Rheological Behaviour and Modelling of Semi-Solid Sn-15% Pb Alloy", *J. Mat. Sci.*, **26** (1991), 2173-2183.

[60] P. Kumar, C.L. Martin, and S. Brown, "Constitutive Modeling and Characterization of the Flow Behavior of Semi-Solid Metal Alloy Slurries - I. The Flow Response", *Acta Metall. Mater.*, **42** (11) (1994), 3595-3602.

[61] C.L. Martin, P. Kumar, and S. Brown, "Constitutive Modeling and Characterization of the Flow Behavior of Semi-Solid Metal Alloy Slurries - II. Structural Evolution Under Shear Deformation", *Acta Metall. Mater.*, **42** (11) (1994), 3603-3614.

[62] M. Mada and F. Ajersch, "Rheological Model of Semi-Solid A356-SiC Composite Alloys Part II: Reconstitution of Agglomerate Structures at Rest", *Mat. Sci. Eng.*, **A212** (1996), 171-177.

[63] A.R.A. McLelland, *et al.*, "Anomalous Rheological Behaviour of Semi-Solid Alloy Slurries at Low Shear Rates", *Mat. Sci. Eng.*, **A232** (1997), 110-118.

[64] C.J. Quaak, M.G. Horsten, and W.H. Kool, "Rheological Behaviour of Partially Solidified Aluminium Matrix Composites", *Mat. Sci. Eng.*, **A183** (1994), 247-256.

[65] W.R. Loué, S. Landkroon, and W.H. Kool, "Rheology of Partially Solidified AlSi7Mg0.3 and the Influence of SiC Additions", *Mat. Sci. Eng.*, **A151** (1992), 255-262.

[66] H. Peng and K.K. Wang, "Steady-State and Transient Rheological Behavior of a Semi-Solid Tin-Lead Alloy in Simple Shear Flow", *Proc. of the Fourth Int. Conf. on the Processing of Semi-Solid Alloys and Composites*, Sheffield, UK (1996), 2-9.

[67] M. Modigell, J. Koke, and J. Petera, "Two-Phase Model for Metal Alloys in the Semi-Solid State", *Proc. of the Fifth Int. Conf. on the Processing of Semi-Solid Alloys and Composites*, Golden, CO (1998), 317-326.

[68] Q.Y. Pan and D. Apelian, "Yield Stress of Al Alloys in the Semi-Solid State", *Proc. of the Sixth Int. Conf. on the Processing of Semi-Solid Alloys and Composites*, Turin, Italy (2000), 399-404.

[69] S. Sannes, H. Gjestland, and L. Arnberg, "Thixotropic Magnesium Alloys", *Proc. of the Sec. Int. Conf. on the Processing of Semi-Solid Alloys and Composites*, Cambridge, MA (1992), 76-85.

[70] J.C. Gebelin, M. Suéry, and D. Favier, "Characterisation of the Rheological Behaviour in the Semi-Solid State of Grain-Refined AZ91 Magnesium Alloys", *Mat. Sci. Eng.*, **A272** (1999), 134-144.

[71] T. Basner, R. Pehlke, and A. Sachdev, "Thin-Wall Back Extrusion of Partially Remelted Semi-Solid Sn-Pb", *Met. and Mat. Trans.*, **31A** (2000), 57-62.

[72] F.C. Yee, *Ph.D. Thesis*, Nanyang Technical University, Singapore (1999).

[73] M. Modigell, *et al.*, "Comparison of Rheological Measurement Methods for Semi-Solid Alloys", *Proc. of the Sixth Int. Conf. on the Processing of Semi-Solid Alloys and Composites*, Turin, Italy (2000), 605-609.

[74] P. Vicente-Hernandez, A.M. Chaze, and C. Levaillant, "Rheological Behaviour of Zn-Sn Alloy in the Solidification Range", *Proc. of the Sec. Int. Conf. on the Processing of Semi-Solid Alloys and Composites*, Cambridge, MA (1992), 316-327.

[75] C. Rouff, *et al.*, "Mechanical Behavior of Semi-Solid Materials", *Proc. of the Sixth Int. Conf. on the Processing of Semi-Solid Alloys and Composites*, Turin, Italy (2000), 405-410.

[76] A.M. de Figueredo, A. Kato, and M.C. Flemings, "Viscosity of Semi-solid A357 alloy in the Transient, High Shear Rate Regime", *Met. Sci. Tech.*, **18** (2) (2000), 32-36.

[77] R.M. German, Liquid Phase Sintering, Plenum Press, New York, (1985).

[78] R.M. German, "Theory of *In Situ* Strength Evolution During Sintering", *Sintering 2000*, 17-31.

[79] M. Gündüz and J.D. Hunt, "The Measurement of Solid/Liquid Surface Energies in the Al-Cu, Al-Si and Pb-Sn Systems", *Acta Metall.*, **33** (9) (1985), 1651-1672.

[80] Y. Ito, M.C. Flemings, J.A. Cornie, "Rheological Behavior and Microstructure of Al-6.5wt%Si Alloy", *Nature and Properties of Semi-Solid Materials*, (1991), 3-17.

[81] T.L. Wolfsdorf, W.H. Bender, and P.W. Voorhees, "The Morphology of High Volume Fraction Solid-Liquid Mixtures: An Application of Microstructural Tomography", *Acta Mater.*, **45** (6) (1997), 2279-2295.

[82] L. Arnberg, A. Bardal, and H. Sund, "Agglomeration in Two Semisolid Type 6082 Aluminium Alloys", *Mat. Sci. Eng.*, **A262** (1999), 300-303.

[83] S. Verrier, *et al.*, "Experimental Investigation by EBSD and X-Ray Tomography of the Agglomeration of the Solid Phase After Deformation in the Semi-Solid State of a A357 Aluminium Alloy", *Proc. of the Sixth Int. Conf. on the Processing of Semi-Solid Alloys and Composites*, Turin, Italy (2000), 423-428.

[84] C.P. Chen and C.-Y.A. Tsao, "Semi-Solid Deformation of Non-Dendritic Structures - I. Phenomenological Behavior", *Acta Mater.*, **45** (5) (1997), 1955-1968.

[85] E. Tzimas and A. Zavaliangos, "Mechanical Behavior of Alloys with Equiaxed Microstructure in the Semisolid State at High Solid Content", *Acta Mater.*, **47** (2) (1999), 517-528.

[86] A.P. Shapiro and R.F. Probstein, "Random Packings of Spheres and Fluidity Limits of Monodisperse and Bidisperse Suspensions", *Phy. Rev. Letters*, **68** (9) (1992).

[87] A.K. Dahle and D.H. StJohn, "Rheological Behaviour of the Mushy Zone and Its Effect on the Formation of Casting Defects During Solidification", *Acta Mater.*, **47** (1) (1999), 31-41.

[88] M Winning, G. Gottstein, and L.S. Shvindlerman, "Stress Induced Grain Boundary Motion", *Acta Mater.*, **49** (2001), 211-219.

[89] B. Sundman, B. Jansson, and J.-O. Anderson, "The Thermo-Calc Database System", *Calphad,* **9** (1985), 153-190.

[90] A.M. de Figueredo, Y. Sumartha, M.C. Flemings, "Measurement and Calculation of Solid Fraction in Quenched Semi-Solid Melts of Rheocast Aluminum Alloy A357", *Light Metals 1998*, TMS, Warrendale, PA, (1998), 1103-1106.

[91] H. Iwasaki, *et al.*, "Shear Deformation Behavior of Al-5% Mg in a Semi-Solid State", *Acta Mater.*, **46** (18) (1998), 6351-6360.

[92] H.V. Atkinson, P. Kapranos, and D.H. Kirkwood, "Alloy Development for Thixoforming", *Proc. of the Sixth Int. Conf. on the Processing of Semi-Solid Alloys and Composites*, Turin, Italy (2000), 443-450.

[93] H.K. Moon, "Rheological Behavior and Microstructure of Ceramic Particulate/Aluminum Alloy Composites", *Ph.D. Thesis*, MIT, (1990).

[94] M.C. Flemings, Solidification Processing, McGraw-Hill, New York, (1974).

[95] B. Sundman, Thermo-Calc Examples, Division of Computational Thermodynamics, Stockholm, (1993).

[96] S. Ganesan and D.R. Poirier, "Densities of Aluminum-Rich Aluminum-Copper Alloys During Solidification", *Met. Trans*, **18A** (1987), 721-723.

[97] S. Viswanathan, *et al.*, "Thermophysical Properties of SSM Ingots and Castings", presented at the Semisolid Metal Processing Consortium Spring Meeting, Worcestor Polytechnic Institute, (1999).